Copyright © 1996 by Hope M. Concannon All rights reserved

#### **Report Documentation Page**

Form Approved OMB No. 0704-018

Public reporting burden for the collection of information is estimated to average 1 hour per response, including the time for reviewing instructions, searching existing data sources, gathering and maintaining the data needed, and completing and reviewing the collection of information. Send comments regarding this burden estimate or any other aspect of this collection of information, including suggestions for reducing this burden, to Washington Headquarters Services, Directorate for Information Operations and Reports, 1215 Jefferson Davis Highway, Suite 1204, Arlington VA 22202-4302. Respondents should be aware that notwithstanding any other provision of law, no person shall be subject to a penalty for failing to comply with a collection of information if it does not display a currently valid OMB control number.

1. REPORT DATE <b>01 FEB 1996</b>	2. REPORT TYPE	3. DATES COVERED <b>00-00-1996 to 00-00-1996</b>
4. TITLE AND SUBTITLE		5a. CONTRACT NUMBER
Two-Photon Raman Gain in a La	aser Driven Potassium Vapor	5b. GRANT NUMBER
		5c. PROGRAM ELEMENT NUMBER
6. AUTHOR(S)		5d. PROJECT NUMBER
	5e. TASK NUMBER	
		5f. WORK UNIT NUMBER
7. PERFORMING ORGANIZATION NAME(S) A <b>Duke University ,Department of</b>	` /	8. PERFORMING ORGANIZATION REPORT NUMBER
9. SPONSORING/MONITORING AGENCY NA	ME(S) AND ADDRESS(ES)	10. SPONSOR/MONITOR'S ACRONYM(S)
		11. SPONSOR/MONITOR'S REPORT NUMBER(S)

12. DISTRIBUTION/AVAILABILITY STATEMENT

Approved for public release; distribution unlimited

13. SUPPLEMENTARY NOTES

14. ABSTRACT

Atomic systems that display a linear or weakly nonlinear interaction with light, such as that occurring in typical optical ampliPers and lasers, are well known and well understood. However, when the interaction between light and matter becomes highly nonlinear and the light and matter strongly couple, the systems become much more difficult to understand both theoretically and experimentally. One example of a strongly coupled, highly nonlinear system is the two-photon laser that is based on the two-photon stimulated emission process. This laser has intrigued theorists and experimentalists alike over the past three decades because of the challenges in explaining the interactions taking place in the device as well as the possibilities for novel and potentially useful behavior. Research concerning two-photon lasers has been hindered, however, by the difficulties in constructing such a laser. Most two-photon gain media prove unsuitable due to small gain and the occurrence of destructive competing nonlinear effects. I have developed a new two-photon gain medium that overcomes these difficulties; it displays large, spectrally-resolved two-photon gain with few competing effects. It consists of a laser-driven potassium vapor in which the origin of the gain is due to the two-photon Raman scattering process. The two-photon gain feature is identified by performing spectroscopy of the laser-driven potassium vapor. I observe 30% two-photon optical ampliPcation, which is two orders of magnitude larger than previously observed gain. To complement the experimental observations, I have developed a theoretical model of the two-photon Raman gain medium using the semi-classical density-matrix formalism. The predictions of the model are in qualitative agreement with the experimentally observed frequency- and intensity-dependence of the two-photon gain. I also describe a simpliPed rate-equation model of two-photon lasers through which I explore their steady-state and transient behavior. The model highlights the novel threshold behavior of two-photon lasers and the need to inject an external field to initiate lasing. This work, both theoretical and experimental, provides the Prst step toward a robust experimental realization of a two-photon laser.

15. SUBJECT TERMS

16. SECURITY CLASSIFIC	CATION OF:		17. LIMITATION OF 18. NUMBER 19a. NA ABSTRACT OF PAGES RESPO		
a. REPORT unclassified	b. ABSTRACT <b>unclassified</b>	c. THIS PAGE unclassified	Same as Report (SAR)  ABSTRACT OF PAGES RESPONSIBLE  REPORT (SAR)		1.00.01.00.01.00.1

Standard Form 298 (Rev. 8-98) Prescribed by ANSI Std Z39-18

# TWO-PHOTON RAMAN GAIN IN A LASER DRIVEN POTASSIUM VAPOR

by

Hope M. Concannon

Department of Physics Duke University

Date:
Approved:
FL
Daniel J. Gauthier, Supervisor
, 1
Dr. John E. Thomas
Dr. Joshua E. S. Socolar
Dr. David D. Skatrud
Dr. Robert G. Brown

Dissertation submitted in partial fulfillment of the requirements for the degree of Doctor of Philosophy in the Department of Physics in the Graduate School of Duke University

 $1 \ {\rm February} \ 1996$ 

#### **ABSTRACT**

(Physics)

# TWO-PHOTON RAMAN GAIN IN A LASER DRIVEN POTASSIUM VAPOR

by

Hope M. Concannon

Department of Physics
Duke University

Date:
Approved:
Daniel J. Gauthier, Supervisor
, •
Dr. John E. Thomas
Dr. Joshua E. S. Socolar
D D :1D Cl + 1
Dr. David D. Skatrud
D D-1 - / C D -
Dr. Robert G. Brown

An abstract of a dissertation submitted in partial fulfillment of the requirements for the degree of Doctor of Philosophy in the Department of Physics in the Graduate School of Duke University

1 February 1996

#### Abstract

Atomic systems that display a linear or weakly nonlinear interaction with light, such as that occurring in typical optical amplifiers and lasers, are well known and well understood. However, when the interaction between light and matter becomes highly nonlinear and the light and matter strongly couple, the systems become much more difficult to understand both theoretically and experimentally.

One example of a strongly coupled, highly nonlinear system is the two-photon laser that is based on the two-photon stimulated emission process. This laser has intrigued theorists and experimentalists alike over the past three decades because of the challenges in explaining the interactions taking place in the device as well as the possibilities for novel and potentially useful behavior. Research concerning two-photon lasers has been hindered, however, by the difficulties in constructing such a laser. Most two-photon gain media prove unsuitable due to small gain and the occurrence of destructive competing nonlinear effects.

I have developed a new two-photon gain medium that overcomes these difficulties; it displays large, spectrally-resolved two-photon gain with few competing effects. It consists of a laser-driven potassium vapor in which the origin of the gain is due to the two-photon Raman scattering process. The two-photon gain feature is identified by performing spectroscopy of the laser-driven potassium vapor. I observe 30% two-photon optical amplification, which is two orders of magnitude larger than previously observed gain.

To complement the experimental observations, I have developed a theoretical model of the two-photon Raman gain medium using the semi-classical density-matrix formalism. The predictions of the model are in qualitative agreement with the experimentally observed frequency- and intensity-dependence of the two-photon gain.

I also describe a simplified rate-equation model of two-photon lasers through which I explore their steady-state and transient behavior. The model highlights the novel threshold behavior of two-photon lasers and the need to inject an external field to initiate lasing.

This work, both theoretical and experimental, provides the first step toward a robust experimental realization of a two-photon laser.

### Acknowledgements

This dissertation and the work described in it would not have been possible without the help and support, both intellectual and emotional, of a number of people.

I would first like to thank my advisor Daniel Gauthier for his guidance and encouragement over the past few years. Even in the darkest experimental stages he never let me give up, always had suggestions for what to try next, and displayed boundless enthusiasm when I saw tangible progress. I also owe him a great debt for forcing me to carefully evaluate my goals and motivations concerning graduate school and beyond. He has never been anything but supportive of my decision to finish my thesis and then to distance myself from the research aspects of physics in order to concentrate instead on physics education, and for that I am very grateful.

The theoretical calculations and numerical simulations described in this thesis relied heavily on the help of William J. Brown. As I was struggling to make deadlines, his efficient programming skills and insights into interpreting the results proved invaluable. In addition, many of the thesis revisions stemmed out of suggestions and comments made by Jeff Gardner. His careful reading and endless questioning helped immeasurably in producing a final draft of my

dissertation.

I've been blessed with the opportunity to be a member of a wonderful research group, with incomparable colleagues. As well as providing an intellectually stimulating environment in which we continually question ourselves and others, the members of my group have worked diligently to expose me to "classic" music and fill in gaps in other parts of my cultural heritage. I'd like to acknowledge the other members of my group: my inestimable colleague David "pluperfect" Sukow, whose jokes only get funnier the more often they are repeated; Martin "wild dogs howling in the night" Hall; and Mark "I can't think of a word you need to put in your thesis" Steen.

As one might expect, my family has greatly influenced the person I am today, from instilling in me early on the love of learning to continually supporting me in my endeavors, whether they be related to further schooling or my extreme hobbies. Though Mom, Dad, Claire, Leah, and Ellen have been many miles away during my time here at Duke, their visits, letters, and phone calls have always kept them close. I'd like to thank them for all that they have done.

And finally, my graduate school years have seen me pass through emotional highs and lows, and often seemed filled with more frustrating times than good times. The friendship and support of colleagues, classmates, and friends has both kept me motivated and kept me sane. Outside of the physics world, my paddling family has provided hours of fun, kept me firmly rooted in the real world, and shown me through words and example that there is more to life than physics. In this group a special thanks must be given to Chris, who has been unflagging in his enthusiasm and support. His love and companionship

have been priceless over the past few years.

This work was supported by the Army Research Office under grants DAAL03-92-G-0286 and DAAH04-94-G-0174; and by the National Science Foundation under grant PHY-9357234-001.

# Contents

A	bstra	${f ct}$	i
$\mathbf{A}$	ckno	vledgements	iii
Li	st of	Figures	x
Li	st of	Tables x	iii
1	Intr	oduction	1
	1.1	Two-photon amplification	3
	1.2	Motivation for the Current Work	5
		1.2.1 Intensity dependent gain	6
		1.2.2 Nonclassical photon statistics	7
		1.2.3 Squeezed light	8
		1.2.4 Novel threshold behavior	9
		1.2.5 Bistable Output	10
	1.3	Problems and Progress	11
	1.4	A new twist on Raman gain	13
	1.5	Experimental Overview	16
	1.6	Thesis Organization	19
2	Fun	damental aspects of two-photon interactions	22
	2.1	The atom-field interaction	23
		2.1.1 Density matrix formalism	23
		2.1.2 Dynamics of the three-level system	25
	2.2	The two-photon Bloch equations	28
	2.3	Intensity dependent gain	30

	2.4		lerations in two-photon laser	
				34
		2.4.1		35
		2.4.2		36
		2.4.3	1 0	37
		2.4.4	Intermediate state detuning	39
		2.4.5	Frequency selection	10
3	Exp	erimer	ntal Apparatus 4	4
	3.1	The P	ump Lasers	15
		3.1.1	The Ti:Sapphire Laser	15
		3.1.2	The Argon Ion Laser	16
	3.2	The D	iode Laser	17
		3.2.1	Laser System Components	18
		3.2.2	Drive Electronics	54
		3.2.3	Locking and Tuning the Grating	59
	3.3	Wavele	ength Selection	67
		3.3.1	The wavemeter	57
		3.3.2	Stabilized Helium-Neon Laser	8
	3.4	The Po	otassium Cell and Heat Pipe	70
	3.5	The O	ptical Layout	76
	3.6	Data A	Acquisition	79
4	Exp	erimer	ntal Procedures and Results 8	<b>1</b>
	4.1	Review	v of Raman Scattering	32
	4.2			35
		4.2.1	Tuning the diode laser to resonance	35
		4.2.2	Scanning the atomic resonance	88
	4.3	Two-b		90
		4.3.1		)1
		4.3.2	Optical pumping	92
		4.3.3	Stimulating field	)4
		4.3.4	Probe-pump alignment	95
		4.3.5		97
		4.3.6		98
	4.4	Genera	al spectral features	
	4 5		Analysis 10	

	4.6	Specti	ra versus probe power	. 108
		4.6.1	Demonstration of two-photon gain	. 110
	4.7	Four-v	wave mixing	. 116
	4.8	Exper	imental parameters	. 123
		4.8.1	The pump detuning	. 124
		4.8.2	Temperature	. 125
		4.8.3	Crossing Angle	. 125
		4.8.4	Beam Intensities	. 125
5	Sen	niclassi	ical Theory of a Driven Three-Level Atom	127
	5.1	Introd	luction	. 127
		5.1.1	Comparison of our model with previous theories	. 129
		5.1.2	Usefulness of the theory	. 132
	5.2	Applie	cation of the density matrix to spectroscopy experiments	. 133
	5.3	Three	-level atom equations of motions	. 135
		5.3.1	Optical Stark Effect	. 137
	5.4	Modif	fications for a second field	. 145
		5.4.1	Computational issues	. 148
		5.4.2	General spectral features	. 151
		5.4.3	Doppler Averaging	. 153
	5.5	Theor	retical parameter values	. 157
		5.5.1	Calculation of the electric dipole matrix elements	. 157
		5.5.2	The Rabi frequency	. 162
		5.5.3	Spontaneous emission rates	. 163
		5.5.4	Ground state decay	. 164
		5.5.5	What are the working intensities?	. 165
	5.6	Comp	parison between theory and experiment	. 167
6	Pre	vious	Work on Two-Photon Lasers	172
	6.1	Theor	etical Work	. 172
		6.1.1	Early Papers	. 174
		6.1.2	Semiclassical Approach	. 176
		6.1.3	Simple Quantum Theory	. 177
		6.1.4	Non-classical light: Squeezing and Photon Statistics	. 184
		6.1.5	Bistabilities and Instabilities	. 192
		6.1.6	Recommended reading	. 197
	6.2	Exper	rimental Progress	

		6.2.1	Early Experimental Work	. 200
		6.2.2	Two-Photon Micromaser	. 202
		6.2.3	Dressed-State Lasers	. 204
		6.2.4	Raman Lasers	208
7	Rat	e-equa	ation model of two-photon lasers	211
	7.1	One-p	hoton rate equations	. 212
		7.1.1	Amplifier model	. 213
		7.1.2	One-photon laser	. 215
	7.2	Two-p	photon rate-equations	219
		7.2.1	Two-photon amplifier model	. 220
		7.2.2	Two-photon laser model	
	7.3	Deriva	ation of the steady-state behavior	. 222
		7.3.1	Steady-state equations for $q_{inj} = 0$	. 223
		7.3.2	Dimensionless equations	
		7.3.3	Steady-state equations for $\tilde{q}_{inj} \neq 0$	
	7.4	Linear	r stability analysis	. 230
		7.4.1	Linearization procedure	. 230
		7.4.2	Linear stability analysis for $q_{inj} = 0 \dots \dots \dots$	
		7.4.3	Linear stability analysis with $q_{inj} \neq 0 \ldots \ldots$	
	7.5	Inject	ion Threshold	
		7.5.1	Transient behavior of the laser	. 243
		7.5.2	Limitations of our model	. 247
8	Cor	ıclusio	ns and Future Directions	249
$\mathbf{B}^{i}$	ibliog	graphy		253
Bi	iogra	phy		270

# List of Figures

1.1	Symbolic illustration of a two-photon laser. Elimination of the mirrors leaves a two-photon amplifier
1.2	(a) The one-photon stimulated emission process. (b) The two-
	photon stimulated emission process
1.3	Schematic representation of the input-output characteristics of
	a system that displays optical bistability
1.4	Level structure for one- and two-photon Raman gain 14
1.5	The experimental geometry
1.6	Two-photon Raman scattering in potassium as a mechanism for two-photon gain
1.7	Gain experienced by a strong probe beam. The two-photon gain is about 30%
2.1	Two-photon gain in a three-level atomic system. The intermediate state $ i\rangle$ enhances the two-photon transition rate 26
2.2	Effect of the two-photon Rabi frequency and the AC Stark shift on the atomic energy levels
2.3	Comparison of the gain bandwidth for a one-photon and two-
	photon laser system
3.1	Top-view of diode laser apparatus
3.2	Grating feedback in the Littrow configuration
3.3	Diode laser current control circuit
3.4	Protection diode wiring to laser
3.5	Geometry of light diffraction from a grating 60
3.6	Monitor photodiode output
3.7	The wavemeter
3.8	The polarization stabilization scheme 69

3.9	Stabilization electronics
3.10	Hyperfine structure of the $4^2S_{1/2}$ , $4^2P_{1/2}$ , and $4^2P_{3/2}$ states of the two abundant isotopes of K
3.11	Cross-sectional view of the heat pipe and potassium cell 75
	Experimental optical layout
4.1	One-photon and two-photon Raman Stokes scattering in $^{39}{\rm K}$ 83
4.2	Single-beam absorption dip
4.3	Diode laser frequency scan showing modehops 89
4.4	The effect of optical pumping on the potassium ground-state
	populations
4.5	Raman scattering resulting from pump-probe interactions 94
4.6	One-photon Raman gain as a function of cell temperature $$ 100
4.7	Typical probe transmission spectrum
4.8	The creation of Rabi resonances in a two-level atom $103$
4.9	Anti-Stokes Raman scattering
4.10	Illustration of the data used for gain/loss calculations 107
4.11	Wide-view showing dependence of the probe transmission spec-
	trum on probe beam power
4.12	Detail showing the dependence of the probe transmission spec-
	trum on probe beam power
4.13	Demonstration of 30% two-photon Raman gain
4.14	Anti-Stokes Raman scattering
4.15	The mechanics of four-wave mixing
4.16	Phase matching requirement for anti-Stokes Raman scattering $$ . 120
4.17	Probe transmission spectrum showing some effects of four-wave
	mixing
5.1	Representation of a three-level atom interacting with two inci-
۲.0	dent fields
5.2	Use of a probe field to study level-shifting effects due to a strong driving field (frequency $\omega_d$ )
5.3	Splitting and shifting of atomic energy levels due to interaction with a strong electromagnetic field
5.4	Change in the splitting between levels $c$ and $a$ as a function of
	pump Rabi frequency
5.5	Level populations as a function of pump Rabi frequency 145
5.6	Typical output spectrum of our theoretical calculations 152

5.7	Comparison of a Doppler averaged spectrum with one that has not been Doppler averaged. Parameter values are the same as	
	those used in Fig. 5.6	155
5.8	Level scheme used in the calculation of dipole matrix elements $$ .	158
5.9	Level diagram for potassium	159
5.10	Theoretical dependence of the probe beam transmission spectrum on probe beam intensity	169
5.11	Comparison between the shape of the calculated theoretical out-	
	put spectum versus actual experimental data	170
6.1	Representation of amplitude and phase squeezing	185
6.2	Steady-state behavior in the two-photon laser	194
6.3	Standard dressed-states for a two-level atom driven at the fre-	
	quency $\omega$	
6.4	Schematic representation of the two-photon dressed-state laser .	207
6.5	Raman scattering as a mechansim for gain	209
7.1	Energy balance between atomic inversion and field photons	213
7.2	Generalized amplifier model showing relevant population-changing processes	215
7.3	Approximate steady-state behavior of the photon number and the inversion above and below the one-photon laser threshold	219
7.4	Steady-state behavior of the cavity photon number and atomic inversion with no injected field	<b>9</b> 93
7.5	Steady-state behavior of the laser showing hysteresis	
7.6	Steady-state behavior of the cavity photon number with a non-	221
1.0	zero injected field	229
7.7	Stability boundary with no injected field	
7.8	Turn-on and turn-off thresholds as a function of injection	
7.9	Comparison between exact and approximate expressions for the laser turn-on threshold	
7.10	Variation of the injection threshold with pump rate	
	Injection threshold for a constant pump rate	
	Transient evolution of the photon number for pumping 20%	_ 12
,.14	above threshold in the good cavity limit	244
7.13	Transient evolution of the photon number in the bad-cavity limit	

# List of Tables

2.1	Parameters used to calculate the two-photon rate coefficient 36
5.1	Values of the reduced matrix element $\langle F' \parallel \mu(1) \parallel F \rangle$ . Each element in the table should be multiplied by the factor $\mu_o$ 160
5.2	Relative values of the z component of the electric dipole matrix elements for the potassium $4^2P_{1/2} \rightarrow 4^2S_{1/2}$ resonance. Each
	element in the table should be multiplied by the factor $\mu_o$ 161

### Chapter 1

#### Introduction

The field of nonlinear optics encompasses the study of the optical properties of materials in the presence of intense electromagnetic radiation. Interest in this field has grown considerably since its birth in the early sixties as advances have been made toward an understanding of basic nonlinear optical effects. The field now includes fundamental studies of the interaction of light with matter as well as diverse applications such as laser development, frequency conversion, phase conjugation, electro-optic modulation, and optical fiber technology.

One interesting nonlinear optical device is the two-photon laser. Like all lasers, a two-photon laser consists of an externally pumped gain medium and a resonant cavity surrounding the gain medium, as shown schematically in Fig. 1.1. The gain is based on the two-photon stimulated emission process, which is a generalization of the one-photon stimulated emission used in typical one-photon lasers. However, nonlinearities inherent in two-photon stimulated emission cause the two-photon laser to have a number of different, and perhaps useful, properties in comparison to other light sources, as described in the following sections. Despite great interest in two-photon lasers due to their

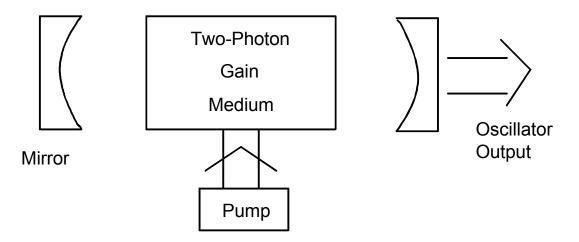


Figure 1.1: Symbolic illustration of a two-photon laser. Elimination of the mirrors leaves a two-photon amplifier.

expected novel properties, there has been limited success in the realization of practical two-photon lasers in the years since they were first proposed [1, 2]. This is in large part due to the small two-photon gain exhibited by most physical systems.

This thesis describes experimental and theoretical investigations of a new two-photon gain medium where the origin of the gain is a process I call two-photon stimulated emission. I observe approximately 30% two-photon optical amplification of a probe laser field propagating through a vapor of laser-pumped potassium atoms, which is 300 times larger than that of previously reported continuous-wave two-photon amplification. This result represents a breakthrough which should make it easier to conduct precise studies of the photon statistics of this highly nonlinear quantum amplifier and to develop and characterize two-photon lasers based on this new gain medium.

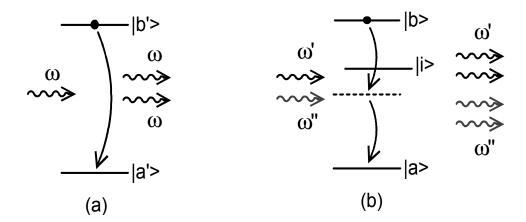


Figure 1.2: (a) The one-photon stimulated emission process. (b) The two-photon stimulated emission process.

#### 1.1 Two-photon amplification

In order to develop a laser based upon two-photon gain, one first needs to develop and optimize a two-photon gain medium. On a microscopic level, the amplification of light results from a complicated interplay of light-matter interactions, one of which is the stimulated emission process. In order to better explain two-photon gain, which is based on a two-photon stimulated emission process, I compare and contrast one- and two-photon stimulated emission effects.

In one-photon amplifiers and lasers, light is amplified upon passing through the gain medium by the one-photon stimulated emission process shown schematically in Fig. 1.2a. Here I consider the interaction of radiation with an atomic medium, where each atom has a pair of bound-state energy levels |b'| > at energy  $E_{b'}$  and |a'| > at energy  $E_{a'}$ , with  $\hbar \omega_{b'a'} = E_{b'} - E_{a'}$ . If the atom is initially in the state |b'| > (due to a pumping process), a radiation field at frequency  $\omega \simeq \omega_{b'a'}$  induces the atom to make a transition from the upper state |b'| to the lower state |a'|. Most importantly for our purposes, the photons scattered by the atom in this process will have the same frequency and direction as the incident photon. This process gives laser light coherence properties much different than random light [3].

The one-photon stimulated emission rate for first-order optical transitions between discrete atomic states  $\mid b' >$  and  $\mid a' >$  is given by

$$R_{1-\gamma} = \left(\frac{8\pi}{\hbar^2}\right) \left| \boldsymbol{\mu}_{b'a'} \right|^2 \left| \mathcal{E}(\mathbf{r}, t) \right|^2 \delta(\omega_{b'a'} - \omega) , \qquad (1.1)$$

where the electric dipole matrix element is denoted by  $\boldsymbol{\mu}_{ij} = \langle i \mid \boldsymbol{\mu} \mid j \rangle$  and I use an electric field of the form  $\mathbf{E}(\mathbf{r},t) = \mathcal{E}(\mathbf{r},t) \exp[-i\omega t] + c.c$ . The stimulated emission rate is proportional to the incident intensity (and hence the photon flux) through  $I = (c/2\pi) |\mathcal{E}(\mathbf{r},t)|^2$  and proceeds most efficiently when: (1) the frequency of the incident photon  $\omega$  is equal to the transition frequency  $\omega_{b'a'}$ ; and (2) when the states have opposite parity and are hence connected by an allowed electric dipole transition matrix element.

In contrast, the gain in two-photon amplifiers and lasers is due to the two-photon stimulated emission process shown schematically in Fig. 1.2b. In this process, two incident photons stimulate an atom from the upper state  $|b\rangle$  to the lower state  $|a\rangle$  and four photons are scattered by the atom. Note that the frequencies  $\omega'$  and  $\omega''$  of the incident photons can take on any value so long as  $\omega' + \omega'' \simeq \omega_{ba}$ , where  $\omega_{ba}$  is the two-photon transition frequency. Throughout the rest of the thesis, however, I assume for simplicity that there is only a single frequency of light stimulating the transition, and hence that  $\omega' = \omega'' \equiv \omega \simeq \omega_{ba}/2$ .

In order to have a basis for comparison with one-photon transitions, consider degenerate two-photon transitions which take an atom from state  $|b\rangle$  to  $|a\rangle$  via a two-photon process through some real intermediate state  $|i\rangle$ . The transition rate in second order for this process (assuming dipole interactions) is

$$R_{2-\gamma} = \left(\frac{32\pi}{\hbar^2}\right) \frac{\left|\boldsymbol{\mu}_{bi}\right|^2 \left|\boldsymbol{\mu}_{ig}\right|^2 \left|\mathcal{E}(\mathbf{r},t)\right|^4}{E_i - E_a - \hbar\omega} \delta(\omega_{ba} - 2\omega) . \tag{1.2}$$

Note that in this case, the two-photon stimulated emission rate is proportional to the square of the incident intensity. The emission process proceeds most efficiently when the states have the same parity (not connected by an allowed electric dipole transition matrix element) and when the real intermediate level is close to the virtual level of the two-photon transition ( $E_i - E_a - \hbar\omega$  small). Additionally, the four scattered photons have the same frequency and direction as the two incident photons. The two-photon stimulated emission process leads to coherence properties different than those of normal one-photon amplifiers and lasers, a fact which will be discussed more as I progress.

The two-photon stimulated emission on which the amplifier or laser is based serves as the most fundamental difference between two-photon amplifiers and lasers and standard one-photon amplifiers and lasers. The nonlinearities inherent in this stimulated emission process also give two-photon lasers and amplifiers a host of interesting properties and novel behaviors which provide a strong motivation for studying them in some detail.

#### 1.2 Motivation for the Current Work

In the most fundamental sense, development of two-photon devices excites researchers because, in the same way that the pioneers of old set off to explore the unknown, it investigates the scientific frontier. Yet climbing a mountain simply "because it is there" is not an entirely satisfying justification; similarly, building a two-photon amplifier "because we can" leaves something to be desired. In fact, the two-photon amplifier and laser offer rich and varied systems that challenge our understanding of the interaction of light with matter. The two-photon laser in particular is a highly nonlinear, far from equilibrium system that cannot be analyzed using standard perturbation techniques. Both the two-photon laser and amplifier represent an entirely new class of quantum optical device that promise to display a wealth of new and exciting nonlinear behavior. The following sections summarize a few of these behaviors, some of which exhibit potential to be harnessed in a variety of scientific and technological fields.

#### 1.2.1 Intensity dependent gain

One immediate consequence of the scaling of the two-photon stimulated emission rate with the incident photon flux (see section 1.1) is that the gain resulting from a two-photon process is intensity dependent. Consider a beam of light (intensity  $I_{in}$ ) incident on a collection of atoms that possesses a two-photon inversion. It will be amplified by an amount that is approximately given by

$$I_{out} \sim I_{in} \exp\left[G^{(2)}I_{in}L\right]$$
 (1.3)

when the frequency of the incident beam is equal to one-half the two-photon transition frequency, where L is the length of the medium and  $G^{(2)}$  is the two-photon gain coefficient. Equation 1.3 is valid when the transition is not saturated and that the gain is very small<sup>1</sup>. Note that the input intensity ap-

<sup>&</sup>lt;sup>1</sup>See Sec. 2.3 for a more complete explanation of the derivation of Eq. 1.3.

pears in the exponential, and hence the gain vanishes when the input intensity is small. This is in contrast to a one-photon gain medium where the gain is independent of the intensity (until saturation sets in).

The intensity dependent gain seen in two-photon gain media made two-photon lasers initially appear to be an experimentalists dream – not only could they produce two tunable frequencies, but they would operate at high power and store large energies. This contrasted with the fixed-frequency, modest power lasers which existed in the early sixties, and provided great motivation to study these novel devices.

#### 1.2.2 Nonclassical photon statistics

Measuring and understanding the statistics of photons allows direct study of the particle character of the electromagnetic field, and hence offers a window into the fundamentals of quantum mechanics. The potential of a two-photon amplifier or a two-photon laser to display nonclassical behavior and statistics has long been discussed. In 1967 Lambropoulos remarked, "At the present time, there are two kinds of light sources, as far as photon statistics is concerned: thermal sources and lasers. The results of this paper [titled Quantum Statistics of a Two-Photon Quantum Amplifier] indicate that by passing laser light through a two-photon amplifier, one will be able to create a light source having a new kind of statistics even if the amplifier operates well below threshold [4]." It was realized that the two-photon amplifier and laser represent potential sources of nonclassical light which may display non-Poissonian photon number statistics and photon bunching or anti-bunching<sup>2</sup>. From that time

<sup>&</sup>lt;sup>2</sup>See Sec. 6.1.4 for a further description of squeezing and nonclassical photon statistics.

on, there has been continuing theoretical interest in the intrinsic nonlinear and nonclassical nature of the two-photon interaction. Although idealized theories exist, the statistical and coherence properties of a real two-photon amplifier and laser are still very much unknown and in need of careful study.

#### 1.2.3 Squeezed light

The nonclassical nature of light generated from a two-photon interaction may have potential applications in optical communications as well. A necessity in any type of communication, optical or otherwise, is that information be transferred with as little distortion or noise as possible. In the electronic regime there is a fundamental lower limit to this noise, yet in the optical regime a few tricks can be played to get around an apparently similar lower limit. It has recently become possible to "squeeze" [5] noise from the amplitude of light to its phase, or vice versa. Information can then be efficiently and effectively transferred on the low-noise light quadrature with little distortion even over very long distances.

The light output from ideal two-photon lasers has been predicted to automatically emerge in one of these squeezed states. This is true of very few, if any, other quantum devices. Harnessing the laser's squeezed noise characteristics could prove quite useful in optical technology and communications systems currently under development. However, predictions concerning the output noise behavior of the two-photon laser are contradictory, some claiming squeezing and others finding an absence of squeezing in any 'real' (versus ideal) system. Similarly, there are many contradictory predictions concerning the squeezed state characteristics of light exiting a two-photon amplifier, yet again no care-

ful tests have been performed. A definitive measurement of the output light characteristics of a two-photon device certainly seems a topic worth pursuing.

#### 1.2.4 Novel threshold behavior

Intensity dependent gain, non-classical photon statistics, and squeezing are behaviors predicted of devices based on a two-photon gain process that are not seen in similar devices based on a one-photon gain process. Further interesting characteristics are predicted of the two-photon laser in particular. Some of the earliest musings about two-photon lasers, for example, recognized that they would display novel threshold behavior. The threshold condition for all lasers requires that the light circulating in the cavity be self-sustaining, and hence the round-trip gain must equal the round-trip loss. For one-photon lasers this criterion yields the well known result that lasing will commence when a uniquely defined minimum inversion, proportional to the gain, is attained via sufficient pumping. The situation is more complicated for the two-photon laser because the gain increases with increasing inversion density  $\Delta N$  and with increasing cavity photon number q (until the atoms are saturated), so the threshold condition must be specified by two parameters. I define a threshold inversion density  $\Delta N_{th}$  as the inversion density needed to satisfy the threshold condition with a cavity photon number  $q_{sat}$  just sufficient to saturate the twophoton gain. When  $\Delta N > \Delta N_{th}$ , there is a corresponding cavity photon number (which is less than, but comparable to,  $q_{sat}$ ) that must be present in the cavity before the laser will turn on. Hence, if the laser is initially off it cannot turn on unless some perturbation, such as an externally injected field, brings it above the necessary value [6, 7, 8, 9]. The two-parameter threshold

condition and need for an external trigger are essentially new laser behaviors.

Tests confirming these behaviors are needed to verify theoretical approaches researchers take toward two-photon lasers.

#### 1.2.5 Bistable Output

The dual threshold condition resulting from the nonlinearities of the system serves to give the laser an interesting, and potentially useful, bistable character. A typical laser, once above threshold, turns on smoothly and reaches a single stable output intensity. A two-photon laser, on the other hand, undergoes a discontinuous transition at the lasing threshold between a low intensity state and the high-output lasing state. Both the low and the high outputs are accessible states of the system for the same given input parameters. The ability to discontinuously jump between these two possible outputs is an example of optical bistability, and allows us to consider the two-photon laser as an optical switch. This behavior is illustrated in Fig. 1.3, and can be described as follows [10]:

If the input intensity is held fixed at the value  $I_{bias}$  (the bias intensity), the two stable output points indicated by the filled dots are possible. The state of the system can be used to store binary information. The system can be forced to make a transition to the upper state by injecting a pulse of light so that the total input intensity exceeds  $I_{high}$ ; the system can be forced to make a transition to the lower state by momentarily blocking the input, taking the intensity below  $I_{low}$ .

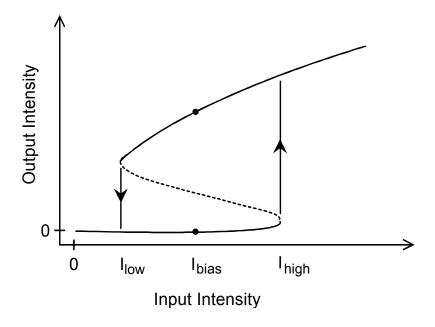


Figure 1.3: Schematic representation of the input-output characteristics of a system that displays optical bistability.

Optical switches are a critical component in any type of all-optical device or optical computer because of their ability to perform logic and memory functions. The potential of optical devices to work faster and at higher bandwidth than many electronic devices has spurred research into their design and construction, and new optically bistable devices like the two-photon laser are constantly in demand.

#### 1.3 Problems and Progress

The previous section presented a wide range of motivations, both fundamental and applied, for studying the two-photon amplifier and two-photon laser and should make clear that a robust experimental realization of both devices is quite desirable. Unfortunately, experimental tests of the numerous, often

conflicting, predictions regarding two-photon amplifier and laser behavior have been hindered by the limited success in the realization of such devices. The smallness of the two-photon gain coefficient  $G^{(2)}$  presents the main stumbling block in both cases. No atomic or molecular gain medium has been found that possesses a large enough two-photon gain coefficient on which to base an effective two-photon amplifier, let alone a two-photon laser. Seemingly, a natural solution would involve using high intensities as can be seen from Eq. 1.3. Unfortunately, several other competing nonlinear optical processes [11], such as four-wave mixing [12], anti-Stokes Raman scattering [13], self-focusing [14], and photo-ionization [15] occur simultaneously in the gain medium and become more prevalent at higher intensities. In addition, normal one-photon lasing or super-fluorescence [16] from the upper state to some other lower-energy intermediate state may deplete the inversion and hence reduce two-photon gain. Typically, the competing processes dominate the two-photon stimulated emission process and prevent the occurrence of two-photon lasing.

Progress toward the realization of a two-photon laser was virtually at a standstill due to the lack of a suitable two-photon gain medium until the recent development of the dressed atom two-photon gain medium [17]. This composite gain medium, made up of laser-pumped two-level atoms, couples the atom to the field in such a way that the energy-level and resonances structure of the atom is modified due to the laser-field induced Stark shifts. Dressed-state atoms provide a near ideal two-photon gain medium which proved remarkably successful and culminated in the first observation of continuous-wave two-photon optical lasing [18].

The dressed-state two-photon laser remains the only two-photon laser ever

successfully realized. Its usefulness is, however, limited by the relatively small  $(\sim 0.1\%)$  two-photon gain it displays. The difficulty in constructing and maintaining a dressed-state two-photon laser based upon gain of only 0.1% is such that it proves impractical to do extended studies on the laser's properties and behavior. This drawback motivated us to search for a new two-photon gain medium. A medium displaying large two-photon amplification would allow detailed studies into the two-photon amplification process and the photon statistics of this unusual quantum amplifier. In addition, a laser based upon a new two-photon gain medium offers the opportunity to distinguish between properties inherent to a general two-photon laser and properties specific to a particular gain medium. Finally, a better two-photon amplifier will make it easier to achieve two-photon lasers, addressing some open questions about the laser's coherence properties, instabilities in output power, photon fluctuation noise, photon correlations, and threshold behavior, for example.

#### 1.4 A new twist on Raman gain

I have discovered and characterized a new type of two-photon gain medium that is capable of amplifying a beam of light by 30% using the two-photon stimulated emission process, about 300 times larger than the best previously reported dressed-atom two-photon gain. The gain mechanism is based on a process I call two-photon stimulated Raman scattering, in which laser photons scatter from a three-level atom as shown in Fig. 1.4b. In this experiment the Raman transition occurred between the hyperfine-split ground-state levels of a laser-driven potassium vapor.

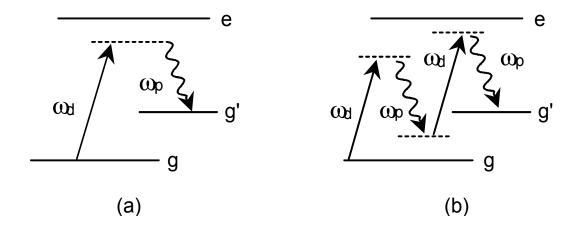


Figure 1.4: Level structure for one- and two-photon Raman gain

In its most basic form, the geometry of Raman scattering is straightforward. A strong driving field (the "pump" beam) passes through a Raman active medium and interacts with the medium in such a way that part of its energy is transferred to waves at frequencies different from that of the source. The component shifted to lower frequency wave is known as the Stokes wave and will be produced when the final atomic state has a higher energy than the initial state. The higher frequency component, resulting from the final atomic state being less excited than the initial state, is known as the anti-Stokes wave. The pump, Stokes, and anti-Stokes wave are all observed at the output of the Raman medium. Most relevant for our purposes, under appropriate conditions stimulated Raman scattering can occur [19], resulting in an exponential growth of the Stokes wave.

In the atomic gain medium, application of a strong driving signal at  $\omega_d$  generates new scattered frequencies at  $\omega_p = \omega_d \pm \Delta_{hfs}$ , when  $\Delta_{hfs}$  is the ground state hyperfine splitting of potassium. Familiar one-photon Raman

Stokes scattering (Fig. 1.4a) involves a single pump photon (at frequency  $\omega_d$ ) and a single scattered Raman photon (at frequency  $\omega_p$ ) in making a transition from the initial state  $|g\rangle$  to the final state  $|g'\rangle$  via a virtual state associated with the excited state  $|e\rangle$ . This occurs at a frequency  $\omega_p = \omega_d - \Delta_{hfs}$ . The intensity of the scattered light for the Raman Stokes process shown in Fig. 1.4a is proportional to the pump intensity (until saturation occurs), the Raman cross section (a medium dependent factor), and the population in the initial state. Because the virtual level is close to the real excited state, the Raman cross section will be greatly enhanced. This Raman process will amplify the Stokes radiation if the populations of the levels are such that an atom is transferred from a more to a less populated state. This amplification is, of course, at the expense of the pumping laser – one laser photon is lost for each Stokes photon that is created. Absorption is expected at frequency  $\omega_p = \omega_d + \Delta_{hfs}$  due to the corresponding anti-Stokes process involving a transition from  $\mid g' > \text{to} \mid g >$ . In our experiment the inversion is such that this process will, of itself, not be amplified.

So far I have only considered conversion to the first Stokes wave. With powerful laser beams, Raman scattering involving multiple pump and probe photons can appear, producing light at the subharmonics of the first Stokes wave. Although these effects have been noticed in spectroscopy and wave-mixing experiments for a number of years, their potential for multiphoton gain has, to my knowledge, never before been carefully studied. I intend to use a two-photon Raman process, shown in Fig. 1.4b, to provide the gain for a two-photon amplifier and a two-photon laser. A two-photon Raman process involves the absorption of two pump photons and emission of two Raman photons in

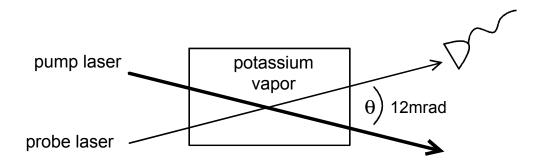


Figure 1.5: The experimental geometry

making the transition between states  $|g\rangle$  and  $|g'\rangle$ , and occurs at frequency  $\omega_p = \omega_d - \Delta_{hfs}/2$ . The intermediate level  $|e\rangle$  that is nearly equidistant from each ground state serves to significantly enhance the transition. Even so, the two-photon Raman transition is a second order effect, and thus the two-photon cross section is much smaller than the one-photon cross section. Two-photon gain thus tends to be relatively small, which might explain why it has been ignored up until now. The two-photon gain coefficient is, however, intensity dependent, differing from the usual Raman gain coefficient, and in agreement with the earlier discussion. This can be intuitively understood since the multiphoton nature of the transition requires the two pump and probe photons to arrive at the atom simultaneously, occurring more often at higher intensities.

#### 1.5 Experimental Overview

The experiment presented in this thesis reports on the observation of 30% continuous-wave two-photon optical amplification in a laser-driven potassium vapor. The experimental geometry is shown in Fig. 1.5 and involves a strong

pump laser and relatively weaker probe laser interacting in a potassium vapor cell. The modifications to the probe beam transmission spectrum due to the presence of the pump beam are detected and analyzed. The pump laser used in this pump-probe spectroscopy is tuned to the red of the 770-nm  $4S_{1/2}$  (F = 1)  $\rightarrow 4P_{1/2}$  (F = 1) transition in potassium and serves two purposes. First, it creates an inversion between the ground-state hyperfine levels (necessary for gain) by optically pumping atoms from the F = 2 to F = 1 levels as they move into the pump beam. Second, it acts as the pump field for the two-photon Raman process. Typical pump intensities are 1 kW/cm<sup>2</sup>. The probe laser, used to stimulate Raman scattering, spatially overlaps the pump beam inside much of the cell and crosses it at a about a 12 mrad angle. Typical probe beam intensities range up to about 50 W/cm<sup>2</sup>.

Using this experimental configuration, I observe large amplification of the probe laser due to one-photon Raman scattering when  $\omega_p \simeq \omega_d - \Delta_{hfs}$  and probe laser power is low. For higher powers, the one-photon Raman gain decreases dramatically and a new gain feature appears at  $\omega_p \simeq \omega_d - \Delta_{hfs}/2$ . I attribute this probe-dependent feature to the two-photon Raman scattering process because it occurs at the expected frequency and it is not present for low probe-beam intensities, as expected for the two-photon stimulated emission process. Figure 1.6 illustrates the two-photon scattering process and relevant energy levels in potassium. Figure 1.7 shows the experimentally measured gain experienced by a strong probe beam as a function of the probe-pump detuning frequency. As seen in Fig. 1.7, I observed single-pass two-photon amplification of about 30%. This gain is sufficiently large as to allow detailed studies concerning the properties of the two-photon amplification process and

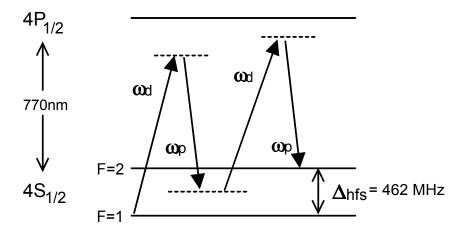


Figure 1.6: Two-photon Raman scattering in potassium as a mechanism for two-photon gain.

make tractable the construction of a two-photon laser.

The two-photon Raman-scattering system provides two significant (and related) advantages over the dressed-state two-photon laser. First, it is relatively insensitive to broadening mechanisms. This stems from two factors: the initial and final states of the Raman transition are long-lived ground states (though they do have a finite effective lifetime due to optical pumping), freeing the system from radiative broadening; in addition, the net Doppler effect for Raman transitions with nearly copropagating beams is nearly zero. Insensitivity to broadening mechanisms leads naturally to the second advantage – it results in extremely good spectral resolution, so the gain feature remains resolved even in a high number-density atomic vapor. Working at high number densities serves as a major source of our gain enhancement over the dressed-atom case. Using a vapor cell rather than an atomic beam as the source of atoms also substantially simplifies the experimental apparatus.

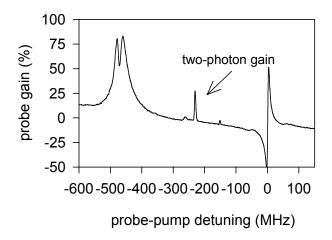


Figure 1.7: Gain experienced by a strong probe beam. The two-photon gain is about 30%.

## 1.6 Thesis Organization

The body of this thesis is divided into six chapters. Chapter 2 develops a semiclassical theory of two-photon transitions in a three-level atom. The results are used to give a basic understanding of a few of the considerations that must go into the design of a two-photon laser, and help to convey why building such a laser is a difficult task.

Chapter 3 describes the experimental apparatus used to perform pumpprobe spectroscopy. A fairly comprehensive overview is presented of the diode laser system. Sections also detail the pump laser, the potassium cell, the optical layout, and the data collection and analysis implementation.

Chapter 4 reports on the experimental results in the development of a new

two-photon gain medium. It describes pump-probe spectroscopy in a potassium vapor cell, carefully explaining experimental techniques and the resulting probe-beam output spectrum. In particular, it notes the appearance of light due to two-photon Raman scattering.

Chapter 5 presents the theory used to describe the interactions of the pump and probe fields with the potassium vapor. I use a density-matrix approach to the problem in which potassium is treated as a three-level atom and both the pump and the probe fields are allowed to interact with all relevant transitions. I also Doppler average over the atomic velocities in order to more accurately represent the physical system. Using reasonable estimates of system and experimental parameters, the theory reproduces all major features in the experimental spectra. Our group intends to use the theory in future work to help predict and optimize system parameters in potassium, as well as to test other alkali atoms for their two-photon gain characteristics.

Chapter 6 carefully reviews the past and current literature on two-photon lasers. It begins with some early theory on two-photon lasers and amplifiers, and progresses through semiclassical and quantum theories of the two-photon laser. The quantum theory naturally leads to interesting predictions concerning the nonclassical nature of the light output from the laser. The stability properties of the two-photon laser are also explored. The chapter ends with a quick synopsis of the important experimental progress towards the realization of a two-photon laser.

Chapter 7 presents a simple rate-equation model for two-photon lasers that, despite its simplicity, captures the essential physics of their behavior and affords an intuitive understanding of their novel threshold and stability behavior. I use the model to investigate the steady-state behavior of the laser, explore the stability of the steady-state solutions, and predict the injected pulse strength necessary to initiate lasing.

## Chapter 2

# Fundamental aspects of two-photon interactions

I begin the discussion of the fundamental aspects of two-photon interactions by investigating the microscopic interaction of a field with a three-level atomic system using a semi-classical density matrix formalism. Although this chapter provides a simplistic picture of these interactions (much simpler than the experiment), it captures many of the essential features expected from a two-photon amplifier or laser, and in doing so elucidates how the scaling of certain experimental parameters affect the two-photon gain. I first derive the two-photon Bloch equations for degenerate two-photon transitions in a three-level atom that describe the time-evolution of the population inversion and two-photon coherence in the atomic system. Using this result, I derive an expression for the intensity of a field as it propagates through a two-photon gain medium, and show that the gain scales with the incident intensity as described by Eq. 1.3. Based on these findings, I discuss the relationships between the two-photon gain, competing one-photon gain, and considerations in building a two-photon oscillator. It is shown that balancing two-photon gain against com-

peting nonlinear effects is a difficult task and a major factor in efforts toward the experimental realization of a two-photon laser.

## 2.1 The atom-field interaction

#### 2.1.1 Density matrix formalism

For completeness, I briefly describe the origin of the density matrix equations; the interested reader should consult one of the many excellent texts on quantum mechanics [20] for a detailed discussion.

For a system in a pure state with wavefunction  $\Psi(t)$ , the wavefunction can be expanded in a linear superposition of the energy eigenstates  $\{|n\rangle\}$ , where these eigenstates are solutions to the time-independent Schrödinger equation  $\hat{H}_0 |n\rangle = E_n |n\rangle$  and  $\hat{H}_0$  is the Hamiltonian of the unperturbed atom. The time evolution of the system is then given by the time-dependent Schrödinger equation

$$i\hbar \frac{\partial}{\partial t} |\Psi(t)\rangle = \hat{H}(t) |\Psi(t)\rangle ,$$
 (2.1)

where  $\hat{H}(t)$  is the full Hamiltonian of the system. Since the interaction between an atom and a field is typically weak, the Hamiltonian can be broken down into the sum of the Hamiltonian of the unperturbed atom  $\hat{H}_0$  and a perturbation term  $\hat{V}$  representing the interaction of the optical field with the atom. In the electric dipole approximation, the interaction operator is given by

$$\hat{V} = -\hat{\boldsymbol{\mu}} \cdot \mathbf{E}(\mathbf{r}, t) , \qquad (2.2)$$

where  $\hat{\boldsymbol{\mu}}$  represents the dipole matrix operator and  $\mathbf{E}(\mathbf{r},t)$  denotes the electric field.

The density operator  $\hat{\rho}(t)$  is defined as the projection operator of the state vector

$$\hat{\rho}(t) = |\Psi(t)\rangle \langle \Psi(t)|. \tag{2.3}$$

This operator can be expressed in matrix form

$$\hat{\rho} = \begin{bmatrix} \rho_{aa} & \rho_{ab} & \rho_{ac} \\ \rho_{ba} & \rho_{bb} & \rho_{bc} \\ \rho_{ca} & \rho_{cb} & \rho_{cc} \end{bmatrix} , \qquad (2.4)$$

where the density matrix elements are given by

$$\rho_{mn} = \langle m \mid \hat{\rho} \mid n \rangle = \langle m \mid \Psi \rangle \langle \Psi \mid n \rangle . \tag{2.5}$$

The time evolution of the density matrix elements is then described by

$$i\hbar \frac{\partial \rho_{mn}}{\partial t} = \left[\hat{H}, \hat{\rho}\right]_{mn} , \qquad (2.6)$$

where Eq. 2.6 is exactly equivalent to the Schrödinger equation given by Eq. 2.1.

For the driven three-level atomic system, I assume that an incoherent pump source modifies the atomic populations and creates a population inversion. The diagonal density matrix elements  $\rho_{mm}$  are probabilities of the atom being in state m and hence describe the time dependence of the 'population' for level m. Because populations are real,  $\rho_{mm} = \rho_{mm}^*$ . Decay of population from the excited state to the ground state is accounted for phenomenologically and is taken to be the sum of the spontaneous emission and collisional transfer rate constants from level l to m,  $\gamma_{lm}$ . The off-diagonal elements are proportional to the atomic dipole moment, and explicitly represent coherences between the atomic levels. Off-diagonal elements satisfy the relationship  $\rho_{lm} = \rho_{ml}^*$  and relax at a rate  $\Gamma_{lm}$ .

The explicit form of the density matrix equations of motion for an atom driven by one or more fields and damped by broadening and decay mechanisms can be found from Eqs. 2.2 and 2.6 and are given by [21]

$$\frac{\partial \rho_{ll}}{\partial t} = -\sum_{\substack{i \\ E_i \le E_l}} \gamma_{li} \rho_{ll} + \sum_{\substack{i \\ E_i \ge E_l}} \gamma_{il} \rho_{ii} + \frac{i}{\hbar} \sum_{i} \left( \boldsymbol{\mu}_{li} \rho_{il} - \boldsymbol{\mu}_{il} \rho_{li} \right) \cdot \mathbf{E}(\mathbf{r}, t)$$
(2.7)

and

$$\frac{\partial \rho_{lm}}{\partial t} = -\left(i\omega_{lm} + \Gamma_{lm}\right)\rho_{lm} + \frac{i}{\hbar}\sum_{i}\left(\boldsymbol{\mu}_{li}\rho_{im} - \boldsymbol{\mu}_{im}\rho_{li}\right) \cdot \mathbf{E}(\mathbf{r}, t) , \qquad (2.8)$$

where  $\omega_{lm} = E_l - E_m/\hbar$ . The dipole matrix elements are denoted by  $\boldsymbol{\mu}_{li}$ , where electric dipole transitions only occur between states of different parity. Thus  $\boldsymbol{\mu}_{ca} = \boldsymbol{\mu}_{ac} = 0$ .

#### 2.1.2 Dynamics of the three-level system

I consider the interaction of a laser field  $\mathbf{E}(\mathbf{r},t) = \mathcal{E}(\mathbf{r},t)e^{-i\omega t} + c.c.$  and the three-level system shown schematically in Fig. 2.1. The states  $|e\rangle$  and  $|g\rangle$  have the same parity (thus  $\mu_{eg} = 0$ ) and state  $|i\rangle$  has the opposite parity. A pump mechanism transfers population from  $|g\rangle$  to  $|e\rangle$  at a rate R to create a population inversion between the two states  $(\rho_{ee} > \rho_{gg})$ . Population in  $|e\rangle$  decays via one-photon spontaneous emission to state  $|i\rangle$  at rate  $\gamma_{ei}$ , which subsequently decays to  $|g\rangle$  at rate  $\gamma_{ig}$ . For simplicity, I assume that  $\gamma_{ig} \gg \gamma_{ei}$  so that essentially no population builds up in the intermediate level.

The field induces two-photon transitions  $|e\rangle \rightarrow |g\rangle$  that proceed through a virtual intermediate level depicted as a dashed line in Fig. 2.1. The real intermediate level  $|i\rangle$  is located near the virtual level (detuning  $\Delta_{ig} = \omega - \omega_{ig}$ ) to resonantly enhance the two-photon transition rate, as shown below.

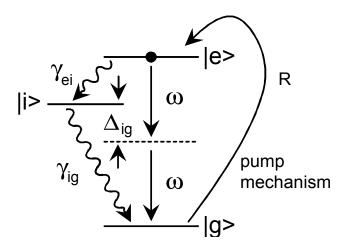


Figure 2.1: Two-photon gain in a three-level atomic system. The intermediate state  $|i\rangle$  enhances the two-photon transition rate.

The density matrix equations for the simplified model of the three-level atom with degenerate two-photon transitions are given by

$$\frac{d\rho_{ig}}{dt} = -(i\omega_{ig} + \Gamma_{ig})\rho_{ig} + \frac{i}{\hbar}(\boldsymbol{\mu}_{ig}\rho_{gg} + \boldsymbol{\mu}_{ie}\rho_{eg} - \boldsymbol{\mu}_{ig}\rho_{ii}) \cdot \mathbf{E}(\mathbf{r}, t), \quad (2.9)$$

$$\frac{d\rho_{ei}}{dt} = -(i\omega_{ei} + \Gamma_{ei})\rho_{ei} + \frac{i}{\hbar}(\boldsymbol{\mu}_{gi}\rho_{eg} - \boldsymbol{\mu}_{ei}\rho_{ee} + \boldsymbol{\mu}_{ei}\rho_{ii}) \cdot \mathbf{E}(\mathbf{r}, t), \quad (2.10)$$

$$\frac{d\rho_{eg}}{dt} = -(i\omega_{eg} + \Gamma_{eg})\rho_{eg} + \frac{i}{\hbar}(\boldsymbol{\mu}_{ei}\rho_{ig} - \boldsymbol{\mu}_{ig}\rho_{ei}) \cdot \mathbf{E}(\mathbf{r}, t), \quad (2.11)$$

$$\frac{d\rho_{gg}}{dt} = \gamma_{ig}\rho_{ii} - R\rho_{gg} + \frac{i}{\hbar}(\boldsymbol{\mu}_{gi}\rho_{ig} - \boldsymbol{\mu}_{ig}\rho_{gi}) \cdot \mathbf{E}(\mathbf{r}, t), \quad (2.12)$$

$$\frac{d\rho_{ee}}{dt} = \gamma_{ei}\rho_{ee} + R\rho_{gg} + \frac{i}{\hbar}(\boldsymbol{\mu}_{ei}\rho_{ie} - \boldsymbol{\mu}_{ie}\rho_{ei}) \cdot \mathbf{E}(\mathbf{r}, t), \quad (2.13)$$

$$\frac{d\rho_{ii}}{dt} = \gamma_{ei}\rho_{ee} - \gamma_{ig}\rho_{ii} + \frac{i}{\hbar}(\boldsymbol{\mu}_{ig}\rho_{gi} + \boldsymbol{\mu}_{ie}\rho_{ei} - \boldsymbol{\mu}_{gi}\rho_{ig} - \boldsymbol{\mu}_{ei}\rho_{ie}) \cdot \mathbf{E}(\mathbf{r}, t), \quad (2.14)$$

Since the coherences  $\rho_{ij}$  contain both a fast time scale (set by the optical frequency  $\omega$ ) and a slow time scale (set by the interaction energy), I introduce

slowly varying coherences  $\sigma_{ij}$  through the relations

$$\rho_{ei} = \sigma_{ei} e^{-i\omega t} , \qquad (2.15)$$

$$\rho_{ig} = \sigma_{ig} e^{-i\omega t} , \qquad (2.16)$$

$$\rho_{eg} = \sigma_{eg} e^{-i2\omega t} , \qquad (2.17)$$

and

$$\rho_{kk} = \sigma_{kk} \ . \tag{2.18}$$

In order to eliminate fast time variations in the density matrix equations I keep only resonant terms, effectively factoring out terms which oscillate at optical frequencies and thus have negligible average response. This is called the rotating wave approximation, and serves to significantly simplify the problem. As a final notational simplification, I write the Rabi frequencies for the dipole-allowed transitions as

$$\Omega_{ig} = \frac{2\boldsymbol{\mu}_{ig} \cdot \mathcal{E}(\mathbf{r}, t)}{\hbar} , \qquad (2.19)$$

and

$$\Omega_{ei} = \frac{2\boldsymbol{\mu}_{ig} \cdot \mathcal{E}(t)}{\hbar} \ . \tag{2.20}$$

The Rabi frequencies provide a natural measure of the strength of the applied signal field and the effectiveness of the laser in stimulating transitions in the atom.

Inserting Eqs. 2.15 - 2.20 into Eqs. 2.9 - 2.14 and making the rotating wave approximation, I find that

$$\frac{d\sigma_{ig}}{dt} = i(\Delta_1 + i\Gamma_{ig})\sigma_{ig} + \frac{i}{2}(\Omega_{ig}\sigma_{gg} + \Omega_{ei}^*\sigma_{eg}), \qquad (2.21)$$

$$\frac{d\sigma_{ei}}{dt} = -i(\Delta_1 - i\Gamma_{ei})\sigma_{ei} - \frac{i}{2}(\Omega_{ig}^*\sigma_{eg} + \Omega_{ei}\sigma_{ee}), \qquad (2.22)$$

$$\frac{d\sigma_{eg}}{dt} = i(\Delta_2 + i\Gamma_{eg})\sigma_{eg} + \frac{i}{2}(\Omega_{ei}\sigma_{ig} - \Omega_{ig}\sigma_{ei}) , \qquad (2.23)$$

$$\frac{d\sigma_{gg}}{dt} = \gamma_{ei}\sigma_{ee} - R\sigma_{gg} + \frac{i}{2}(\Omega_{ig}^*\sigma_{ig} - \Omega_{ig}\sigma_{gi}), \qquad (2.24)$$

and

$$\frac{d\sigma_{ee}}{dt} = -\gamma_{ei}\sigma_{ee} + R\sigma_{gg} + \frac{i}{2}(\Omega_{ei}\sigma_{ie} - \Omega_{ei}^*\sigma_{ei}). \qquad (2.25)$$

## 2.2 The two-photon Bloch equations

This set of equations can be further simplified through adiabatic elimination of the one-photon coherences (performed formally by setting  $d\rho_{ig}/dt = d\rho_{ei}/dt =$  0) which is valid so long as  $\Delta_1 \gg \Gamma_{ei}$ ,  $\Gamma_{ig}$  [21]. Under these circumstances the dipole moment of the atoms follows the applied field. Adiabatic elimination immediately allows us solve for the one-photon coherences, giving

$$\sigma_{ig} = -\frac{1}{2\Delta_1} (\Omega_{ig} \sigma_{gg} + \Omega^*_{ei} \sigma_{eg})$$
 (2.26)

and

$$\sigma_{ei} = -\frac{1}{2\Delta_1} (\Omega_{ei} \sigma_{ee} + \Omega^*_{ig} \sigma_{eg}) . \qquad (2.27)$$

Inserting Eqs. 2.26 and 2.27 into Eqs. 2.23 – 2.25 and introducing the twophoton population inversion  $w = \sigma_{ee} - \sigma_{gg}$  (where the total population in the levels is normalized to unity,  $\sigma_{ee} + \sigma_{gg} = 1$ ), I find that the equations-of-motion for the population inversion and the slowly varying two-photon coherence are given by

$$\frac{dw}{dt} = -(\gamma_{eg} + R)(w - w_{eq}) - i[\Omega^* \sigma_{eg} - \Omega \sigma_{ge}], \qquad (2.28)$$

and

$$\frac{d\sigma_{eg}}{dt} = i[\Delta_2 - \delta_s + i\Gamma_{eg}]\sigma_{eg} + \frac{i}{2}\Omega w . \qquad (2.29)$$

Equations 2.28 and 2.29 are known as the two-photon Bloch equations, where

$$\Omega = \frac{\Omega_{ig}\Omega_{ei}}{2\Delta_1} \tag{2.30}$$

is the two-photon Rabi frequency,

$$\delta_s = \frac{|\Omega_{ei}|^2 - |\Omega_{ig}|^2}{4\Delta_1} \tag{2.31}$$

is the frequency shift due to the AC Stark effect, and

$$w_{eq} = \frac{R - \gamma_{eg}}{R + \gamma_{eg}} \tag{2.32}$$

is the population inversion in the absence of an applied field.

Two important parameters describing a two-photon system have become self-evident in the two-photon Bloch equations. The first is the two-photon Rabi frequency, which gives an indication of the strength of the two-photon interaction in the same way that the more familiar one-photon Rabi frequency gives information about the strength of one-photon interactions. The AC-Stark shift of the two-photon transition is a shift in the atomic energy levels resulting from interaction with oscillating electric fields<sup>1</sup>. A simplified diagram illustrating the effect of the two-photon Rabi frequency and the AC Stark shift on the atomic energy levels is shown in Fig. 2.2. The initial and final states of the two-photon transition are shifted apart by the AC Stark shift, while the levels are split by the two-photon Rabi frequency.

<sup>&</sup>lt;sup>1</sup>Interaction of atoms with a static electric field has long been known to produce shifts of atomic energy levels, traditionally termed DC Stark shifts. In both the AC and DC Stark effect, an applied electric field induces a large dipole moment in an atom. This dipole moment then interacts with the field via the electric dipole interaction to produces the shift in atomic energy levels.

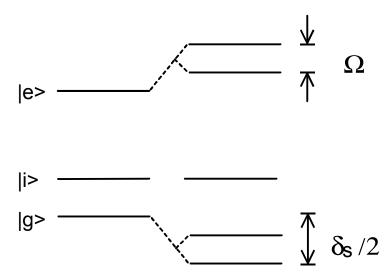


Figure 2.2: Effect of the two-photon Rabi frequency and the AC Stark shift on the atomic energy levels.

## 2.3 Intensity dependent gain

The two-photon Bloch equations allow us to explore how an applied optical field evolves as it propagates through a two-photon gain medium. Since the intensity dependence of a two-photon gain process provides the basis for many of the novel characteristics expected of two-photon lasers and amplifiers, it is worthwhile to derive a first-order approximation to the two-photon gain coefficient. In addition, the form of the result, which reproduces Eq. 1.3, proves particularly intuitive.

The evolution of an optical field within the amplifier is described by Maxwell's Equations. For a non-conducting, non-magnetic gain medium without any free charges or currents, Maxwell's Equations can be manipulated to arrive at the

optical wave equation [22, 23]

$$\nabla^{2}\mathbf{E}(\mathbf{r},t) - \frac{1}{c^{2}}\frac{\partial^{2}\mathbf{E}(\mathbf{r},t)}{\partial t^{2}} = \frac{4\pi}{c}\frac{\partial^{2}\mathbf{P}(\mathbf{r},t)}{\partial t^{2}},$$
 (2.33)

where  $\mathbf{P}(\mathbf{r},t)$  is the polarization (i.e., the dipole moment per unit volume) of the medium. The polarization is given in terms of the density matrix through the relation  $\mathbf{P}(\mathbf{r},t) = N\langle \hat{\boldsymbol{\mu}} \rangle = NTr(\hat{\rho}\hat{\boldsymbol{\mu}})$  where N is the number density of atoms. For a monochromatic plane-wave electric field propagating in the +zdirection,

$$\mathcal{E}(\mathbf{r},t) = \hat{\epsilon}A(z)\exp(ikz) \tag{2.34}$$

where  $\hat{\epsilon}$  is the polarization unit vector. Similarly, the polarization can be expressed as

$$\mathbf{P}(\mathbf{r},t) = \mathcal{P}(z) \exp[-i(\omega t - kz)] + c.c.$$
 (2.35)

Inserting Eqs. 2.34 and 2.35 into the wave equation and making the slowly varying amplitude approximation  $(\partial^2 A/\partial z^2 \ll k\partial A/\partial z)$ , the spatial evolution of the field is given by

$$\frac{\partial A(z)}{\partial z} = i2\pi k \hat{\epsilon} \cdot \mathcal{P}(z) . \qquad (2.36)$$

The intensity of the field is given by

$$I(z) = \frac{c}{2\pi} \left| \mathcal{E}(\mathbf{r}, t) \right|^2 , \qquad (2.37)$$

and hence

$$\frac{\partial I(z)}{\partial z} = \frac{c}{2\pi} \left( A(z) \frac{\partial A^*(z)}{\partial z} + c.c. \right) = -2\omega \operatorname{Im} \left[ A^*(z) \hat{\boldsymbol{\epsilon}} \cdot \mathcal{P}(z) \right] . \tag{2.38}$$

Because Eq. 2.38 involves only the imaginary part of the quantity  $A^*(z)\hat{\epsilon}\cdot\mathcal{P}(z)$ , I explicitly evaluate  $\text{Im}\left[A^*(z)\hat{\epsilon}\cdot\mathcal{P}(z)\right]$  and ignore any pure-real terms in the

bracket. For the three-level system,

$$\mathcal{P}(z) = N(\boldsymbol{\mu}_{ie}\sigma_{ei} + \boldsymbol{\mu}_{gi}\sigma_{ig})$$

$$= -\frac{N}{2\Delta_{1}} \left[ \boldsymbol{\mu}_{ie}(\Omega_{ei}\sigma_{ee} + \Omega_{ig}^{*}\sigma_{eg}) + \boldsymbol{\mu}_{gi}(\Omega_{ig}\sigma_{gg} + \Omega_{ei}^{*}\sigma_{eg}) \right] , \quad (2.39)$$

where in the second equation I have used Eqs. 2.26 and 2.27 for the coherences  $\sigma_{ei}$  and  $\sigma_{ig}$ . Expressions for  $\sigma_{ee}$ ,  $\sigma_{gg}$ , and  $\sigma_{eg}$  are found by solving the two-photon Bloch equations in steady-state,

$$w = \sigma_{ee} - \sigma_{gg} = w_{eq} \left[ 1 + \frac{|\Omega|^2 \Gamma_{eg}}{(\gamma_{eg} + R)[(\Delta_2 - \delta_s)^2 + \Gamma_{eg}^2]} \right]^{-1}$$
(2.40)

and

$$\sigma_{eg} = \frac{-\Omega w_{eq}}{2(\Delta_2 - \delta_s + i\Gamma_{eg})} \left[ 1 + \frac{|\Omega|^2 \Gamma_{eg}}{(\gamma_{eg} + R)[(\Delta_2 - \delta_s)^2 + \Gamma_{eg}^2]} \right]^{-1} . \tag{2.41}$$

I find

$$\operatorname{Im} \left[ A^{*}(z) \hat{\boldsymbol{\epsilon}} \cdot \mathcal{P}(z) \right] = - \left[ \frac{N \left| A(z) \right|^{4} \left| \hat{\boldsymbol{\epsilon}} \cdot \boldsymbol{\mu}_{ig} \right|^{2} \left| \hat{\boldsymbol{\epsilon}} \cdot \boldsymbol{\mu}_{ei} \right|^{2} w_{eg} \Gamma_{eg}}{\Delta_{1}^{2} \hbar^{3} \left[ (\Delta_{2} - \delta_{s})^{2} + \Gamma_{eg}^{2} \right]} \right] \times \left[ 1 + \frac{4 \left| A(z) \right|^{4} \left| \hat{\boldsymbol{\epsilon}} \cdot \boldsymbol{\mu}_{ig} \right|^{2} \left| \hat{\boldsymbol{\epsilon}} \cdot \boldsymbol{\mu}_{ei} \right|^{2} \Gamma_{eg}}{\Delta_{1}^{2} \hbar^{4} (\gamma_{eg} + R) \left[ (\Delta_{2} - \delta_{s})^{2} + \Gamma_{eg}^{2} \right]} \right]^{-1} . (2.42)$$

Although the above expression can be used to evaluate the field intensity as a function of z, in general its complicated intensity dependence (both  $|A(z)|^2$  and the Stark shift  $\delta_s$  are intensity dependent) make this a nontrivial computation.

If, however, I consider the case when the Stark shift  $\delta_s$  is zero (i.e.,  $|\hat{\epsilon} \cdot \boldsymbol{\mu}_{ig}|^2 = |\hat{\epsilon} \cdot \boldsymbol{\mu}_{ig}|^2$ ), I can derive a relatively simple expression for  $\partial I(z)/\partial z$ . Introducing the two-photon saturation intensity  $I_{sat}$  defined by

$$\frac{1}{I_{sat}^{2}} = \frac{4\pi^{2}}{c^{2}} \frac{4\left|\hat{\boldsymbol{\epsilon}} \cdot \boldsymbol{\mu}_{ig}\right|^{2} \left|\hat{\boldsymbol{\epsilon}} \cdot \boldsymbol{\mu}_{ei}\right|^{2} \Gamma_{eg}}{\Delta_{1}^{2}\hbar^{4}(\gamma_{eg} + R)[\Delta_{2}^{2} + \Gamma_{eg}^{2}]}$$
(2.43)

I find that

$$\operatorname{Im}\left[A^*(z)\hat{\boldsymbol{\epsilon}}\cdot\mathcal{P}(z)\right] = -\frac{\hbar N(R - \gamma_{eg})}{4} \frac{I^2}{I_{sat}^2 + I^2} \ . \tag{2.44}$$

Thus

$$\frac{\partial I(z)}{\partial z} = \frac{\hbar \omega N(R - \gamma_{eg})}{2} \left[ \frac{(I/I_{sat})^2}{1 + (I/I_{sat})^2} \right] \equiv G^{(2)} \left[ \frac{I^2}{1 + (I_{in}/I_{sat})^2} \right] , \quad (2.45)$$

where  $G^{(2)}$  is the two-photon gain coefficient.

Rather than attempting to directly solve this differential equation for the intensity, I consider propagation of the field through a thin slice of the gain medium in which the change in the intensity can be described reasonably by

$$\frac{\partial I(z)}{\partial z} = \frac{I(z+L) - I(z)}{L} \ . \tag{2.46}$$

For a thin medium where the intensity is approximately constant throughout, I find

$$I_{out} = I_{in} + \frac{I_{in}^2}{1 + (I_{in}/I_{sat})^2} G^{(2)}L$$
, (2.47)

where  $I_{in} = I(z)$  and  $I_{out} = I(z + L)$ . For low intensities  $(I_{in} / I_{sat} \ll 1)$  and a thin medium  $(I_{in}G^{(2)}L \ll 1)$ ,

$$I_{out} \simeq I_{in} + G^{(2)}L I_{in}^2 + \text{higher order terms}$$
  
 $\simeq I_{in} \exp[I_{in}G^{(2)}L]$  (2.48)

Equation 2.48 reproduces Eq. 1.3.

I write the intensity in this form in order to emphasize the similarity of the beam intensity behavior to that for ordinary linear gain media in which  $I_{out} = I_{in} \exp[G^{(1)}L]$ . The expressions are identical with the exception that the two-photon gain in the exponential has a linear intensity dependence. Yet this intensity dependence leads to entirely new behaviors – not only does the gain increase with intensity, but because the input intensity appears in the exponential, the gain vanishes when the input intensity is small.

## 2.4 Considerations in two-photon laser construction

The two-photon Bloch equations derived earlier contain information that helps to explain why building a two-photon laser is difficult. In order to explore this problem it becomes useful to draw upon results from my rate-equation model of two-photon lasers that will not be discussed in detail until Chapter 7. The rate-equations are written in terms of the two-photon rate coefficient  $B^{(2)}$ , and the model then derives results for the two-photon saturation number  $q_{sat}$  and saturation intensity  $I_{sat}$  in a two-photon laser cavity, as well as the required threshold inversion density  $\Delta N_o^{th}$  to initiate two-photon lasing. Referencing ahead to Sections 7.2 and 7.3, I have

$$q_{sat} = \sqrt{\gamma/2B^{(2)}} ,$$
 (2.49)

$$I_{sat} = c\hbar\omega q_{sat} / V_c , \qquad (2.50)$$

and

$$\Delta N_o^{th} = n \, w_{eq} = 4q_{sat} \, \gamma_c / \gamma V_a \,, \qquad (2.51)$$

where  $\gamma$  ( $\gamma_c$ ) is the population (cavity) decay rate,  $V_c$  is the volume of the cavity, and n is the number density of the gain medium.

The two-photon Bloch equations obtained from the density matrix formalism are connected to the rate equations under conditions when there is large dephasing of the two-photon coherence ( $\Gamma_{eg} \gg \Delta_2, \Delta_s, \gamma, \gamma_c$ ). In this case, the two-photon coherence can be adiabatically eliminated from Eq. 2.28 using Eq. 2.29 with  $\partial \sigma_{eg}/\partial t = 0$ . It is then found through comparison with the rate equations (Eq. 7.17) that the two-photon rate coefficient is given by

$$B^{(2)} = \frac{32\pi^2 \left| \boldsymbol{\mu}_{ei} \cdot \hat{\boldsymbol{\epsilon}} \right|^2 \left| \boldsymbol{\mu}_{ig} \cdot \hat{\boldsymbol{\epsilon}} \right|^2 \omega^2}{V_c^2 \hbar^2 \Delta_{ig}^2 \Gamma_{eq}} , \qquad (2.52)$$

where  $\hat{\epsilon}$  is the polarization unit-vector of the field. Note that the rate coefficient can be enhanced significantly when the real intermediate level  $|i\rangle$  is close to the virtual level of the two-photon process, that is, when  $\Delta_{ig}$  is small. It was an understanding of this scaling that led to the development of the first microwave two-photon oscillator [24, 25], and the first two-photon optical laser [18].

In what follows, I point out some of the considerations that go into building a two-photon laser that immediately follow from the two-photon Bloch equations, the intensity-dependent gain seen in two-photon amplifiers, or the rate-equation model of two-photon lasers.

#### 2.4.1 Stark-shifted levels

The AC Stark shift which appears in the two-photon Bloch equations can play an important role in the dynamics of two-photon amplifiers and lasers. As a simple example, note that the two-photon transition frequency is intensity dependent due to the intensity dependence of the Stark shift. Now assume, for example, that a laser cavity is exactly tuned to the two-photon transition frequency. A field initially resonant with both the cavity and the atoms will experience gain, and the field intensity will increase as described by Eq. 2.45. Yet the increasing field intensity serves to Stark shift the levels progressively farther

```
dipole moment, |\boldsymbol{\mu}_{ei} \cdot \hat{\epsilon}|
                                                        ea_o = 2.4 \times 10^{-18} \text{cm}^{5/2}
                                                                           10^8 s^{-1}
      population decay rate, \gamma
                                                                        1 \times 10^9 \text{s}^{-1}
 coherence dephasing rate, \Gamma_{eq}
                                                                        1 \times 10^{13} \text{s}^{-1}
intermediate level detuning, \Delta_{iq}
                                                                       3 \times 10^{15} \text{s}^{-1}
            laser frequency, \omega
             cavity length, L
                                                                             5~\mathrm{cm}
                                                                      6\times10^{-4}~\rm{cm^3}
            cavity volume, V_c
                                                                        6\times10^7\mathrm{s}^{-1}
         cavity decay rate, \gamma_c
      (corresponds to 1\% loss)
```

Table 2.1: Parameters used to calculate the two-photon rate coefficient.

apart, detuning the cavity from resonance by a greater and greater amount. This level shifting will eventually lead to two-photon loss rather than gain, and hence the intensity dependence of the two-photon transition frequency complicates the design of potential two-photon laser cavities.

## 2.4.2 Saturation intensity

An important conclusion drawn from the rate-equation model of a two-photon laser is that the intensity circulating in a two-photon laser resonator is always greater than or equal to the two-photon saturation intensity. Because of this, the gain medium must have a *low* two-photon saturation intensity both to avoid the high intensities that tend to magnify competing nonlinear optical processes and to keep the cavity intensities within physically realizable bounds.

Let's now see what the equations describing the two-photon rate coefficient and saturation intensity can tell us. Using values that are typical for a three-level two-photon optical gain medium and a resonator with a loss-per-pass of 1% (see Table 2.1), Eqs. 2.50, 2.51, and 2.52 give  $B^{(2)} = 2.6 \times 10^{-12} \text{s}^{-1}$ ,  $I_{sat} = 6.6 \times 10^4 \text{W} \cdot \text{cm}^{-2}$ , and  $\Delta N_o^{th} = 1.8 \times 10^{13}$  atoms-cm<sup>-3</sup>. The intensity circulating in the resonator is modest in comparison to some present-day lasers,

giving hope that competing nonlinear optical effects, such as self-focusing and photoionization, can be avoided. In addition, the threshold inversion density is quite low (and easily realizable in an atomic vapor, for example).

It also proves enlightening at this point to calculate the saturation intensity for other gain media with detunings quite different from that given in Table 2.1. Early explorations into two-photon gain media often looked at metastable atomic levels for which no intermediate state existed. In such a two-level model, the detuning parameter is equal to the laser frequency and is orders of magnitude larger than when an intermediate state does exist. With all other parameters remaining the same, this situation would increase the saturation intensity to  $2.2 \times 10^7 \; \mathrm{W} \cdot \mathrm{cm}^{-2}$ . An intracavity intensity of 20 MW-cm<sup>-2</sup> approaches the limits of easily available present-day continuous-wave lasers, and probably presented a formidable barrier to experimentalists of the 1960's. In the other extreme, the Raman system discussed in this thesis can easily have intermediate state detunings smaller than 2 GHz, corresponding to saturation intensities only on the order of 20 W-cm<sup>-2</sup>. This would seem to be an ideal situation – the intensity is low and easily realizable, while the two-photon rate coefficient and corresponding gain, which scale inversely with detuning, have increased by orders of magnitude. Based on these numbers, we have not yet come upon any fundamental limitations hindering two-photon laser construction, and it would seem straightforward to achieve two-photon lasing.

## 2.4.3 Competing effects

Unfortunately, nothing turns out to be quite this simple! Although the saturation intensities may be reasonable to achieve, we have not yet carefully considered the potential for competing processes to interfere with two-photon lasing and complicate two-photon laser design. For example, we must consider the possibility that normal one-photon lasing on the  $|e\rangle \rightarrow |i\rangle$  transition can occur at a frequency spectrally distinct from the desired two-photon lasing frequency. This would prevent any two-photon lasing from occurring. For sufficiently low one-photon gains, one-photon lasing can be avoided using a high-finesse cavity that selectively enhances the two-photon laser frequency and not the one-photon laser frequency. Yet in systems with high one-photon gain (a fairly typical situation in systems that also have relatively large two-photon gain), cavity selectivity proves less effective because amplified spontaneous emission or superfluorescence may occur and destructively interfere with potential two-photon lasing.

In amplified spontaneous emission, spontaneous emission from a single atom is amplified as it propagates through an inverted medium. Superfluorescence involves cooperative spontaneous emission among many atoms. In both effects, quantum fluctuations at the normal one-photon lasing frequency lead to amplification at this frequency, and an incoherent excitation of atoms may produce a macroscopic output signal. When this occurs, spontaneous emission may, after amplification, become large enough to deplete the laser inversion before the desired two-photon optical signal can be efficiently propagated. The strength of each of these emission processes is determined by the gain of the system. As found by Malcuit [26], when the gain increases above unity the radiative decay of the collection of atoms is initially characteristic of amplified spontaneous emission. As the gain continues to increase the emission characteristics will become more like superfluorescence. The threshold for superfluorescence

occurs when the single-pass one-photon gain  $G^{(1)}L$  is on the order of 10-30 [27].

I find the single-pass one-photon gain on the  $|e\rangle \rightarrow |i\rangle$  transition in the three-level atomic medium using the density matrix equations to be

$$G^{(1)}L = \frac{4\pi\Delta N_o^{th} \left| \boldsymbol{\mu}_{ei} \cdot \hat{\epsilon} \right|^2 \omega L}{\hbar c \Gamma_{eq}} , \qquad (2.53)$$

and estimate the size of this gain using parameters typical for a two-photon optical gain medium (see Table 2.1). I find that  $G^{(1)}L \sim 640$ , well into the superfluorescence regime. This one-photon gain can be reduced in order to avoid superfluorescence only by reducing the number density (which also unfortunately reduces the two-photon gain!) or shortening the cavity length (which may be physically impossible depending upon the experimental situation). The number density must be reduced by a factor of about 20 to just avoid superfluorescence and by a factor of 100 to avoid significant depletion of the inversion. Yet for a 100-fold decrease in the number density, the loss-per-pass in the resonator must be less than about  $10^{-4}$  to achieve two-photon lasing. Such low-loss resonators can be constructed using recently developed super-polished mirrors, but 15 years ago this would have presented an impossible requirement. Note that in this low-loss situation the gain medium must be in contact with the mirrors that form the resonator because any other optics in the cavity will give too high of a loss.

## 2.4.4 Intermediate state detuning

As mentioned earlier, the two-photon rate coefficient scales inversely with the detuning from the intermediate state. But now it should be clear that working with small detunings is useful for a number of related reasons. Smaller detunings reduce the saturation intensity in the system, and lower saturation intensity.

sities make it easier to avoid competing nonlinear optical effect which become more prevalent at high intensities. In addition, the single-pass one-photon gain does not scale with detuning. Thus, as the two-photon rate coefficient increases with decreasing detuning, there is virtually no change in the one-photon gain. The relative size of the two-photon gain with respect to the competing one-photon gain increases favorably. Small detunings proved key in the realization of the two-photon maser and two-photon dressed-state laser.

#### 2.4.5 Frequency selection

In discussing potential methods for preventing one-photon lasing and superfluorescence from destructively interfering with two-photon lasing, the size of the two-photon gain sets constraints on the methods we can use. If the two-photon gain is large, simple elements with a frequency selective loss (like an etalon or birefringent filter) placed inside the cavity can be used to prevent lasing at competing frequencies. However, the gain is generally not high enough for this to be reasonable. Consider, for example, the dressed-state two-photon laser which displayed a two-photon gain of only 0.1%. Cavity losses greater than this 0.1% gain would prevent the system from making it above threshold and lasing on the two-photon transition. Yet an intracavity element such as a birefringent filter generally has a loss of at least 0.5% at the transmission peak, which is unacceptably high.

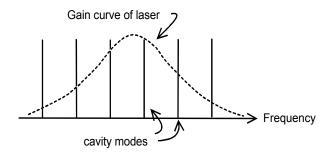
A different method of frequency selection involves using short (a few centimeters) optical cavities. In systems with relatively small intermediate state detunings, it becomes possible to force the free-spectral range<sup>2</sup> of the two-

<sup>&</sup>lt;sup>2</sup>The free-spectral range is defined as the frequency spacing between adjacent cavity modes, and is found in terms of the cavity length L as  $\Delta_{FSR} = c/2L$ .

photon laser cavity to be larger than the frequency splitting between the two-photon and one-photon gain features. If a cavity mode is then carefully aligned with the gain curve for the two-photon lasing frequency, it becomes impossible for one-photon lasing frequency to simultaneously match up with a laser cavity mode. In the case of the Raman system, in order to differentiate between the one- and two-photon gain features requires a free-spectral range of about 2 GHz, which corresponds to a cavity length of only 7.5 cm. Note, however, that because total two-photon gain increases with cavity length, working with small cavities sacrifices some precious two-photon gain.

In addition, we need to consider the gain bandwidth of the two-photon gain peak. As we have seen, the two-photon gain scales as one over the square of the detuning  $\Delta_{ig}$ . As a result, two-photon gain media displaying high gain have a reasonably narrow gain bandwidths; in the Raman system for example, the gain bandwidth is only on the order of 10-20 MHz. But now imagine the practical difficulties of matching this gain curve to a cavity mode. In typical laser systems, the gain medium has a very broad gain bandwidth such that a number of cavity modes lie under the gain curve (see Fig. 2.3a). The combination of the lasing transition lineshape with the resonant cavity modes gives the resulting output of the laser, and since all of the cavity modes under the gain curve can potentially lase, initiating lasing is straightforward. In the case of a two-photon laser, however, the initial alignment must be extremely precise. If the narrow gain bandwidth curve doesn't overlap with a similarly narrow cavity mode (see Fig. 2.3b), there will be no lasing!

It should have become obvious by now that many of the design constraints on a two-photon laser involve balancing the available two-photon gain with the



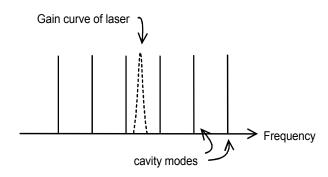


Figure 2.3: Comparison of the gain bandwidth for a one-photon and two-photon laser system. In (b), lasing will not occur unless the gain curve of the laser overlaps with a cavity mode.

occurrence and prevention of destructive competing effects. Few, if any, of the problems mentioned here would be impossible to overcome using the benefits of modern technology. They did, however, prove virtually insurmountable to researchers of ten and twenty years ago. Even now, it remains extremely difficult to overcome all of the problems and still be left with a *robust* experimental realization of a two-photon laser. The high two-photon gain and small detuning found in the Raman gain medium described in this thesis, however, gives us a significant edge. Though exact design considerations need to be explored, we will be able to construct a two-photon laser based upon two-photon stimulated

#### Raman scattering.

This chapter was intended to serve as a primer for a discussion on twophoton lasers and amplifiers. By looking at only a few simple quantities, we
were able to come to some understanding of the considerations that must go
into the design of a two-photon laser, and hence arrive at an understanding
of why building such a laser has proven to be a difficult task. However, the
discussion should have also given at least an intuitive understanding of why a
Raman gain medium that displays very high, spectrally resolved two-photon
gain should be useful in overcoming some of the experimental difficulties mentioned earlier. The next few chapters discuss experimental and theoretical work
in the realization of a high-gain two-photon amplifier.

## Chapter 3

## Experimental Apparatus

The goal of the experiment described in this thesis is to perform pump-probe spectroscopy in a potassium vapor cell as a means of producing and measuring high two-photon gain. In the past, the largest hindrance to the realization of a two-photon laser has been the lack of a suitable two-photon gain medium. This experiment uses Raman scattering to overcome earlier difficulties and achieve high gain. Future work will utilize this gain and expand upon the existing experimental apparatus in order to construct a two-photon laser.

This chapter discusses the experimental components and setup for pumpprobe spectroscopy. The necessary apparatus includes a 'pump' laser and
'probe' laser, the potassium vapor cell, and all of the necessary equipment
for data collection and analysis. A proportionately large amount of time is
spent discussing the diode laser (the probe laser), because unlike the commercial lasers this system was developed and built by us, and hence has no
accompanying instruction manual. It is also the first stabilized, tunable diode
laser in the physics department, and because we expect such lasers to become
standard laboratory equipment in the next few years a careful description of

them seems in order.

## 3.1 The Pump Lasers

This experiment requires a high-powered, tunable source of electromagnetic radiation to act as a pumping field for exploring light-matter interactions. I use a titanium-doped-sapphire laser pumped by an argon-ion laser for this purpose.

## 3.1.1 The Ti:Sapphire Laser

A Coherent Model 899-21 solid state Ti:Sapphire ring laser acts as the pump laser for the system. With the short-wave optics in the cavity, it is tunable from 700 to 825 nm. Both passive and active frequency control are used to obtain stable single-mode operation.

A series of intracavity elements with wavelength dependent losses force the laser into a single longitudinal mode. These include the birefringent filter (400 GHz free spectral range), the thick etalon (10 GHz free spectral range), and the thin etalon (225 GHz free spectral range). The birefringent filter is mounted at Brewsters angle inside the cavity and can be rotated about the beam axis. Light passing through the filter gets a frequency dependent polarization rotation, which, due to other cavity elements, translates into a frequency dependent loss. The etalons work in the standard manner, transmitting only those wavelengths with the proper relationship to the etalon spacing. Laser cavity modes are approximately determined by the requirement that an integral number of optical wavelengths spans the cavity, and are predicted to be spaced by about 150 MHz. Only the cavity mode with the most gain can lase at any one time,

and that mode will be the one that corresponds most nearly to the maximum transmission of all three of the wavelength dependent loss elements mentioned above.

Active frequency control is maintained by an electronic servo-loop which uses an error signal generated from the reference cavity when the laser frequency drifts. High-speed cavity length variations are corrected using a piezo-electrically driven mirror, while a rotating Brewsters plate compensates for lower speed length variations. Single-mode frequency scanning of up to 30 GHz is achieved by continuously varying the effective cavity length with the galvanometer driven Brewster plate.

Typically, the output of the Ti:Sapphire laser is about 800 mW at 770 nm with about 6 W of pumping power. Maintaining reasonably high powers on a day-to-day basis requires little maintenance beyond tweaking the control knobs to optimize the laser output. Over time, however, this daily tweaking can walk the cavity to a less efficient lasing mode, requiring removal of the etalon assembly and realignment of the empty cavity.

## 3.1.2 The Argon Ion Laser

A Coherent Innova model 310 argon-ion laser pumps the Ti:Sapphire laser. The active medium consists of an ionized gas plasma contained in a low-pressure tube, which is positioned inside an optical cavity consisting of two dielectrically coated laser mirrors. A DC current passing through the plasma tube creates a population inversion, thus providing the energy which is converted to laser light through the process of stimulated emission.

An intracavity beam shaping aperture adjusts the laser to run in approx-

imately a  $TEM_{00}$  Gaussian mode. System settings and control are accessed through a remote menu-controlled module. The laser uses a servo-controlled actively stabilized optical cavity which maintains a reasonably constant output power over the course of a day. It supplies about 6 W of laser power when 45 A and 200 V are applied across the plasma tube.

## 3.2 The Diode Laser

Diode lasers are fast becoming an invaluable tool for use in atomic physics and laser spectroscopy [28]. One reason for their popularity rests on their tuning flexibility – their emitted wavelength is sensitive to input current, temperature, and feedback from external reflecting surfaces. By controlling the temperature and forward injection current, the wavelength can be tuned a few nanometers to either side of the laser's principle operating wavelength, though there are often spectral gaps in this tuning curve. The unadulterated laser tends to run multimode, where each mode can have a linewidth on the order of 10-100 MHz. These tuning and linewidth characteristics are unacceptable for many physics applications. Locking the diode laser system to an external optical cavity, however, can force the laser to run in a single, narrow (~1 MHz) mode and allow continuous tuning over large spectral ranges. Such tunable, frequency-controlled lasers provide a simple and inexpensive method for probing atomic resonances.

The diode laser system uses frequency-selective optical feedback from a diffraction grating to narrow the laser linewidth and control the laser frequency [29]. An external cavity created by the back facet of the laser diode and the grating define the laser cavity length and hence the laser frequency. Slight

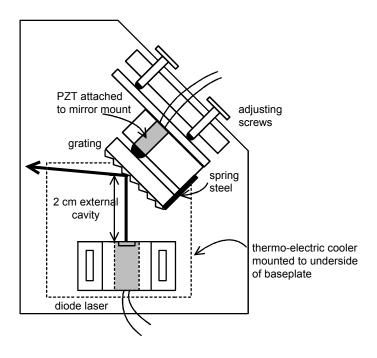


Figure 3.1: Top-view of diode laser apparatus

rotations of the grating alter the cavity length, tuning the laser frequency. To avoid output power fluctuations due to unwanted cavity length variations, the laser-grating system must be mechanically and thermally stable. In addition, the laser power supply must output a stable, low-noise current to the laser. In this section, I extensively discuss the diode laser system, its components, and its tuning behavior.

## 3.2.1 Laser System Components

A grating stabilized diode laser serves as the probe laser. The laser system itself is composed of the laser diode, a collimating lens, and a diffraction grating driven by a piezoelectric actuator (PZT), all mounted on a baseplate, as schematically indicated in Fig. 3.1. Descriptions of the components are given

below.

#### The laser and lens

I use an SDL-5401 50 mW continuous-wave single-mode laser diode with an operating wavelength of 780 nm. The collimating lens is made by Optima Precision and has a numerical aperture of 0.476. It is mounted with the laser in a small self-contained package, also made by Optima Precision, which offers the capabilities of precise three-dimensional positioning and locking of the lens in order to collimate and direct the beam. Collimation requires motion of the lens toward or away from the laser, while some aberrations, which appear when the lens is not properly centered and collinear with the laser, require corrections by translational lens placement in the directions perpendicular to the beam.

Collimation of the output beam proves remarkable easy using the Optima mounts. The diode laser outputs an elliptical beam with a polarization perpendicular to its major axis. The beam's departure from a circular cross-section leads to aberrations, most notably astigmatism, on it after passing through the lens. Upon propagation, astigmatism then causes the cross-section of the beam to undergo a distinct change where its elliptical cross-section gradually evolves into a circle, and then opens out into an ellipse rotated 90° from its initial orientation. The point at which the cross-section is circular is designated the "disk-of-least-confusion". Ideal beam collimation consists of adjusting the lens to move the disk-of-least-confusion as far from the laser as possible, which in turn involves adjusting the distance of the lens to the diode facet. Minor adjustments of the longitudinal lens position smoothly vary the beam between having a rapidly diverging output, being well-collimated, and having and a

focus only millimeters from the lens itself. I am typically able to place the disk-of-least-confusion ~4 m downstream of the laser. Once collimated, the beam is aimed directly down the laser axis, which was previously identified as the center of the dispersive laser output with no lens. The desired orientation of the laser in the mount produces a horizontally polarized output beam, and corresponds to the collimated elliptical output of the diode laser having its major axis vertical.

I should note that the lenses are by no means perfect. The far-field pattern ( $\sim 3$  m downstream) of the laser beam is not Gaussian, but instead has a lobed pattern with one or more dark stripes through the beam. I determined that the Optima lens caused this aberration, and tests of a number of different lenses found that virtually all physically small lenses, even those with high numerical aperture, cause similar aberrations in the far-field pattern. The only lens which seems to give a clean beam was a Melles Griot 06GLC002, but at the time the system was being assembled it was unavailable. I decided to live with the non-idealities of the beam. They do not cause significant problems for this work because the entire experiment takes place within  $\sim 2$  m of the diode laser itself.

#### The grating

The choice of grating is determined as a trade-off between greater feedback, and hence more frequency control, versus coupling out more power. This proves a difficult compromise. The laser needs to be pulled very far from its free-running wavelength – the  $D_1$  potassium resonance line is at 770 nm, while the laser runs at 780 nm – requiring a large amount of feedback. Yet seeing

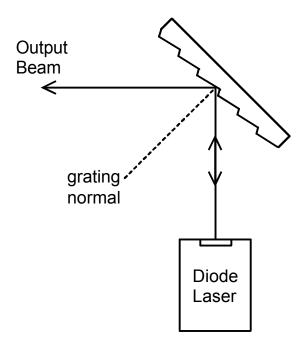


Figure 3.2: Grating feedback in the Littrow configuration.

a large two-photon gain feature, the experimental goal, requires high diode laser output power. Different groove spacings, blaze angles, and incident light polarizations were tested to determine what gives the best ratio of output light to feedback light in order to effectively lock the laser.

I use an Edmund Scientific 1800 lines/mm holographic grating with a visible blaze in the Littrow configuration. In Littrow, the diffracted beam is collinear with the incident beam and feeds back into the laser as shown in Fig. 3.2. The grating thus serves as an equivalent end mirror of the laser cavity, with the back facet of the diode providing the second end mirror. The output beam consists of the zeroth order, specularly reflected beam. When mounted, the grating has its rulings vertical (and thus perpendicular to the polarization of the laser) and the blaze points away from the output beam. This is different

from the usual blaze configuration where the blaze points in the direction of the output, yet empirically gives us the best feedback qualities. The zeroth-order output coupling is 30%, while the measured diffraction efficiency in the first order is 49%, strongly coupling the internal cavity modes to the external cavity. The external laser cavity is about 1.5 cm long, corresponding to an axial mode spacing of 10 GHz. In attaching the grating to its mount, I insure that the rulings are exactly vertical by forcing the diffracted beams to be in the same horizontal plane as the specularly reflected beam.

Because the output beam is taken directly from the grating, it is deflected horizontally as the wavelength is scanned. A common solution to this motion is to modify the external cavity by placing a beamsplitter between the collimating lens and the grating to pick off a stationary output beam. Unfortunately, this configuration introduces enough cavity losses that it becomes impossible to effectively lock the laser at the necessary wavelength. This does not pose a significant experimental problem, because once the laser is locked to the proper wavelength the scanned region is so small as to lead to negligible displacement.

#### The piezoelectric actuator (PZT)

As in all lasers, changes in the laser cavity length cause changes in the laser frequency. A PZT mounted between the back of the grating and the movable face of the mount rotates the grating about a vertical axis and precisely alters the cavity length with electrical control. Once the grating position for feeding back light at the 770 nm potassium resonance is set by hand, the PZT is used to scan the grating about this position. I use a Burleigh PZO-007 that provides a maximum of 5  $\mu$ m of displacement when 100 V is applied. Generally less

than 10 V is needed to fully scan through atomic resonance.

#### **Fluctuations**

Although the fact that changes in the laser cavity length cause changes in the laser frequency are used to our advantage in tuning the laser, undesired changes due to mechanical or thermal fluctuations must be avoided. I designed the external cavity to reduce random mechanical movement as much as possible. All electrical leads are clamped to the table to prevent motion, and a limp insulated wire is used for direct connections to the laser itself to prevent transmitting vibration to the structure.

In addition, laser frequency tunes with temperature because both the optical path length of the cavity and the wavelength dependence of the gain curve depend on temperature. The laser temperature is monitored using a thermistor inserted into the aluminum laser mount very near the center of the laser/lens package. Although precise temperature control is necessary for long term stability of the laser at a particular wavelength, and I did develop and test a temperature control circuit, I found that the system works satisfactorily with only a thermoelectric cooler used to set the temperature of the entire laser-grating system. The cooler is a square 1.5 inches on a side, and fits between the baseplate and an aluminum heatsink. A thin layer of heatsink compound is applied on both sides of the cooler to insure good thermal contact.

Unfortunately, chilling the laser can create condensation in and on the laser and mount. On very humid days condensation often causes the laser to become unstable, preventing accurate data collection. The laser is enclosed in a plexiglass box in order to aid temperature stabilization by reducing the

effects of air currents. I also put desiccant in the box, and circulated nitrogen through it to keep the laser dry. None of these solutions worked particularly well.

Despite great efforts, mechanical and thermal vibrations caused the tuning characteristics of the laser to be workable, but less than ideal. The laser mounts have since been redesigned based upon a design used at NIST that does an extremely effective job of isolating the laser from any mechanical vibrations. The new design encloses the lasers in a hermetically sealed box in order to further reduce the effects of air currents and to minimize humidity and condensation effects. Finally, the temperature controllers that I designed are now used to independently control the temperature of the laser diode and of the baseplate. The continuation of the work described in this thesis uses this new diode laser setup.

#### 3.2.2 Drive Electronics

The circuit diagram for the laser drive electronics is shown in Fig. 3.3, and a brief explanation of its workings is given below [30]. The drive electronics are designed to provide a stable, low noise current supply to run the laser. Normally for low noise applications diode lasers are driven by batteries. This setup proves impractical, however, if we wish to modulate the injection current. The amplitude and frequency output of diode lasers is modulated easily and rapidly by changing their injection current. This proves extremely useful for tuning the lasers, yet means that any fluctuations or noise in the current driving the laser will translate into frequency and power fluctuations in the laser output. Passive and active feedback (using capacitors and a gated FET in conjunction

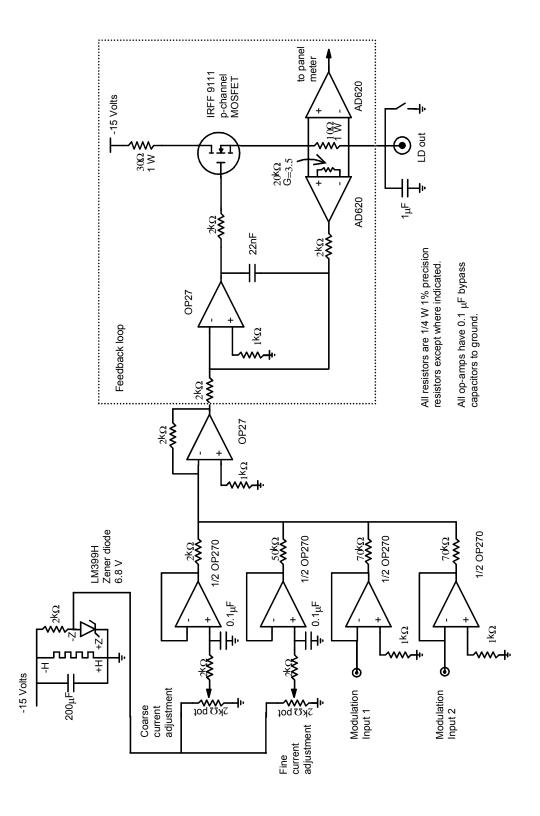


Figure 3.3: Diode laser current control circuit.

with a feedback loop) are used to reduce these fluctuations and noise signals. The supply output current is regulated through a FET before being sent to the laser diode. The current passes through a resistor, converting it to a voltage, and the feedback loop compares this voltage to a stable reference voltage. The loop is designed to quickly and efficiently eliminate any fluctuations from this reference. Creation of a stable feedback loop and stable reference voltage thus constitute the most important objectives in building the current supply.

Power to the circuit is provided by a -15 V voltage source connected to ground through a large capacitor and a zener diode. The capacitor deadens fluctuations in the -15 V signal and prevents any large transient spikes in the current upon turn on. The zener diode package, which includes a heater, acts as a temperature stabilized voltage reference. It has a stabilized breakdown voltage of 6.95 V, and the precision to which this zener maintains its breakdown voltage sets the precision of all other reference voltages in the circuit.

The actual current in the circuit is set by two potentiometers which act as ideal voltage dividers between the zener output and ground. The relative difference in the two resistances leads to a coarse and fine adjust for the voltage divider. The output of each potentiometer is buffered, passes through a resistor, and enters the summing amplifier. The output current can be modulated by sending a voltage into either of two modulation inputs, and any such modulation is also sent into the summing amplifier. The voltage set by the combination of the coarse and fine current adjustments and the modulation enters the feedback loop and acts as the stable reference voltage with which to compare the output voltage heading to the diode laser.

The feedback control loop is best understood as a whole. The steady-state

condition of the loop is such that the current and voltage at the inverting input of the controlling op-amp is zero. This input is a combination of the reference voltage set earlier and the supply output voltage, which is measured as the voltage output of the AD620 instrumentation amplifier. Assuming DC current through the circuit, the steady-state of the feedback loop is such that both input terminals are virtual grounds and a steady current is output by the opamp and passed through the FET. If the signal is not steady-state, the system should be stable such that any fluctuations are deadened. For example, if the FET gate voltage increases due to a positive fluctuation, a greater drain current will result. The AD620 senses a larger negative voltage drop, and creates a non-zero voltage reference at one terminal of the controlling op-amp. The difference between the positive and negative node voltages of the op-amp is negative and increasing, so the inverted output voltage is positive and increasing. This leads to an increase in the output current of the op-amp, reducing the gate voltage and opposing the original fluctuation. The loop is seen to be stable.

The laser current supply described above produces a very stable, low-noise output. I measure the noise of the output current by passing it through a resistor to ground and looking at the voltage on a spectrum analyzer. With the feedback loop, measurement shows that the supply is ~10dB quieter than a current source characterized by Poisson statistics below shot noise in the frequency range 0-200 kHz. Design specifications require all current modulation to fall within this frequency range.

Laser diodes are easily damaged by unwanted current or voltage spikes. Protection was built into the supply in the form of large capacitors to insure slow and even switching behavior. I also used resistors and LEDs in place of

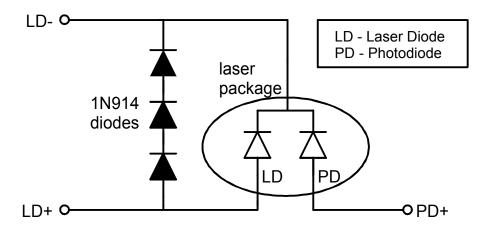


Figure 3.4: Protection diode wiring to laser

the laser while building and testing the power supply in order to check that the supply produced the proper currents and had no significant transients upon turn-on or turn-off. During these tests, I recorded power output and threshold measurements of the laser, both to insure it was working properly and to use as a comparison and analysis tool if the laser started misbehaving at a later date.

Despite these precautions, I did lose a few laser diodes, presumably to voltage or current spikes. A paper by Wieman et al. [28] suggested that "the lifetime of laser diodes is substantially increased by also connecting several forward biased diodes across the leads...These diodes have a large enough voltage drop that current does not flow through them under normal operation. However, if there is a large forward voltage, these diodes turn on allowing the current to flow through them instead of the laser diode." I installed these protective diodes as shown in Fig. 3.4, and have not since lost a single diode laser to catastrophic failure. Although this might be a result of better operating

procedures and finally clawing my way beyond the destructive phase of the learning curve, retaining these diodes seems like a good practice.

#### 3.2.3 Locking and Tuning the Grating

I have already said that the laser system uses a grating to provide frequency-selective feedback into the laser. For the feedback to effectively narrow the laser linewidth, allow continuous frequency tuning, and lock the laser to the feedback frequency (suppressing lasing at the natural frequency), the grating must be carefully positioned and aligned. This section describes how to position the grating for successful locking and tuning of the diode laser frequency.

#### Grating feedback

The system uses a diode laser with external, frequency selective optical feedback from a diffraction grating to provide a narrowband, continuously tunable source of light. Without external control, the diode laser output is typically 15 MHz wide and can be continuously tuned only over certain limited regions. Coupling an external cavity to the diode laser greatly increases the laser's effective cavity length, and thus narrows its linewidth. Strong coupling to an external cavity with a frequency selective element such as a grating also improves the frequency tuning of the laser. Optical feedback successfully narrows the bandwidth to under 1 MHz, and allows us not only to tune the laser over a region of about  $\pm 5$  nm, but also to continuously scan the laser frequency over a range of about 2 GHz.

A careful selection of the pivot point about which the grating is rotated allows us to simultaneously scan the cavity length and the grating feedback angle, thereby permitting a continuous single-mode scan over a limited range[31]. In

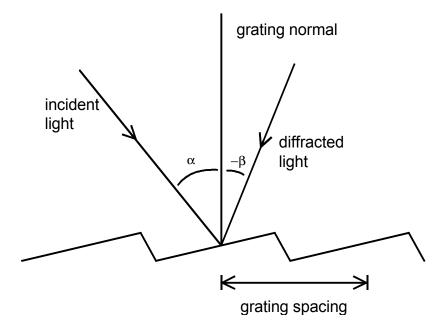


Figure 3.5: Geometry of light diffraction from a grating.

order to achieve this tracking, two relationships must be satisfied: the master grating equation (which determines the coarse tuning of the cavity)

$$\lambda_L = \frac{d}{m}(\sin\alpha + \sin\beta) ; \qquad (3.1)$$

and

$$\lambda_L = \frac{2}{N}L \;, \tag{3.2}$$

which simply states that the cavity length corresponds to an integral number of half wavelengths. In the above equations,  $\lambda_L$  is the lasing wavelength, L is the laser cavity length, m is the diffraction order  $(0, \pm 1, \pm 2, \text{ etc.})$ , and d is the grating spacing. Figure 3.5 defines the angles used in Eq. 3.1. For this system with lasing frequency 770 nm, cavity length 1.5 cm, and a grating spacing of 1800 lines/mm, the optimized grating pivot point was determined to be 3.0 cm at  $44^0$  from the laser facet. These measurements are incorporated into the

baseplate design shown in Fig. 3.1.

#### Locking the laser using grating feedback

The following procedure is used to lock the laser to the external cavity created between the grating and the rear facet of the diode. As a first approximation, the beam diffracted from the grating must return to the center of the lens after retracing its outgoing path. To do this, I place a punched hole in a computer card in front of the laser, allowing the beam to pass through the aperture. The return beam is visible on the back side of the card, and the horizontal and vertical adjusting screws on the grating mount are moved until the beam passes back through the hole in the card. I perform this entire procedure at a laser current setting well below the operating current, because when the laser locks to the feedback frequency the output power can suddenly increase by as much as a factor of two. Near normal operating currents this may take the laser above its maximum specified output power and optically destroy the front facet of the diode.

The locking characteristics of the diode are extremely sensitive to a precise vertical alignment of the return beam. Most references [29] suggest setting the diode current just above threshold and observing the intensity of the output beam while adjusting the vertical tilt of the grating. The output beam should significantly brighten at the exact vertical position that optimizes feedback into the diode. At this point, the laser should be operating with grating controlled feedback near its free-running wavelength. Unfortunately, this procedure did not work well for the SDL lasers. Numerous vertical settings of the grating appear to enhance the laser output near threshold, and the output beam often

consists of more than a single collimated spot. I attribute this unusual behavior to the special manufacturing processes used by SDL labs to produce narrow-band, single-mode output lasers. I developed my own alignment method in order to obtain good locking results.

I use an iterative procedure in which the laser threshold is slowly lowered to vertically align the return beam from the grating. The diode laser package has a built-in monitor photodiode whose output current is directly proportional to the output power of the laser. I pass this current through an current-to-voltage converter with a 10 kHz bandwidth, and continually monitor the resulting signal on an oscilloscope; this serves as a window into the workings of the laser. I use a triangle wave to modulate the diode current, and reduce the current until the laser is just below threshold throughout the entire modulation scan. The monitored laser output then simply mirrors the triangle wave modulation. I then adjust the vertical tilt of the grating while continually observing the effects of the adjustments using the monitor photodiode. At a vertical position that optimizes feedback, the laser can go above threshold at the peaks of the modulation. A distinct change appears in the monitored output: there is a severe change of slope at the modulation peaks where the laser power no longer mirrors the modulation, but instead increases rapidly due to stimulated (versus spontaneous) emission. These sharp peaks during the small part of the modulation scan that the laser goes above threshold are shown in Fig. 3.6. Because more than one vertical position enhances the laser output near threshold, every time the laser locks and goes above threshold, I reduce the current further (taking it below threshold again) and readjust the vertical position. The correct vertical grating position yields the *lowest* laser threshold current.

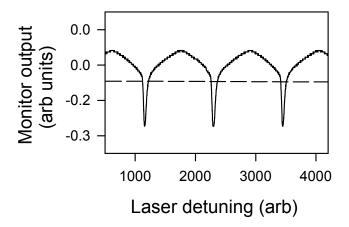


Figure 3.6: Monitor photodiode output where the laser is above threshold only at the peak of the modulation scan. A larger negative output corresponds to increasing laser output.

Although this procedure sounds quite straightforward, in fact it often proves quite nontrivial. If the alignment of the planets is in your favor, it may take only half an hour to achieve a good laser lock. At times, however, even after a full day the laser might not display ideal locking behavior. The key words for working with diode lasers really do seem to be patience, patience, patience!

#### Tuning the Grating

Once the vertical position of the grating is set, the laser frequency should be locked to the external cavity and the lasing wavelength can be tuned using the grating's horizontal adjustment screw. As explained before, the angle at which the first-order diffracted beam is emitted is wavelength dependent, so tuning the grating tunes the angle of the diffracted beam, and thus the laser wavelength, which makes it back into the laser.

There is a finite region over which the laser remains locked to the external cavity. This horizontal tuning range of the grating is identified using two independent methods. Near the end of the tuning range, part of the locking (diffracted) beam may spill off of the laser diode and illuminate the monitor photodiode directly. This significantly increases the apparent laser output power, determined from the photodiode current, and can initially fool the unwary experimentalist into believing that the laser has achieved a good lock. However, this increased photodiode signal is very large, smooth, and does not have mode hops or a frequency dependence as the grating is tuned further. This behavior is very different from the typical laser locking characteristics and is easily identifiable, so it can act as a first test for determining the end of the grating tuning range.

A second test can be performed while looking at the laser output at a current far above threshold. Again, near the end of the tuning range the laser may partially unlock and hop back and forth between two very different frequencies: the free-running frequency at which the laser operates without effective feedback; and the angle-dependent frequency set by the grating. This behavior may appear as a sharing of power between two separate output spots, or the output may literally hop between two output spots horizontally separated from one another. The points where I lose control of the laser output frequency empirically define the grating tuning range.

The grating tuning range as determined above extends only  $\pm 5$  nm about the laser's free-run, room temperature wavelength of 780 nm. The desired

wavelength, the potassium resonance at 770 nm, is significantly blue of this free-run wavelength, and reaching it is beyond the ability of simple grating control. I implement temperature control in addition to grating control to further pull the laser frequency to the blue. According to laser specifications, changing the diode temperature is predicted to shift the entire tuning range by 0.3 nm/°C. With the laser chilled down to about 5°C using a thermoelectric cooler, the laser can be successfully locked to the desired wavelength. At this temperature, however, the laser frequency is at the very edge of the horizontal grating tuning range determined above. Ideally the laser frequency should be positioned in the center of the gain curve, because far from the gain peak the range of continuous tuning decreases. At the natural laser wavelength of 780 nm it proves easy to scan over  $\sim 10$  GHz without hopping laser modes; at 770 nm it becomes difficult to scan even 2 GHz. Theoretically, chilling the laser further should continue to shift the gain curve until 770 nm is centered on it, hence improving the tuning characteristics. The condensation problem mentioned earlier, however, gets worse at lower temperatures and prevents further cooling.

A thermoelectric cooler is used to compensate for thermal drift and subsequent laser frequency changes. Over the course of a day, the laser current at which the diode laser scans through potassium resonance consistently drops, perhaps by 10 mA over 8 hours, due to slight increases in the ambient temperature. It is experimentally desirable to perform the experiments at the highest possible operating currents and powers. In order to keep the laser frequency constant at these high currents, it becomes necessary to chill the laser a bit more as the day wears on and the system heats up. This variation is

not a problem over the data collection time scales, but it is obvious that independently temperature stabilizing the laser and baseplate would reduce the laser frequency thermal drift and subsequent changes in the cavity and grating alignment.

After any significant horizontal tuning of the laser, the vertical grating alignment needs to be rechecked using the threshold current method. There is noticeable cross-coupling between the horizontal and vertical adjustments of the grating, especially near the edge of the tuning range. In order to walk the laser down to 770 nm while maintaining a frequency lock, it proves necessary to tune the wavelength by small amounts (0.5-1 nm) and then re-optimize the vertical position before going any further. This iterative process leads to the highest rate of success.

The previous discussion, hints, and suggestions were derived from many hours (days, weeks, and months, even!) spent fiddling with the diode laser, redesigning the current supply, and going through numerous iterations of the mounting apparatus. Some of the 'tricks of the trade' are necessarily specific to this laser and mounting scheme. Much of the discussion is, however, general enough to apply to other grating feedback schemes.

The initial design and construction of these diode laser systems required a great deal of time and patience (and a large supply of laser diodes!). The final product is, however, well worth the effort. Once constructed, the diode lasers are extremely well-behaved: their frequency behavior is very consistent even after being turned on and off over a number of weeks; they have very little noise or laser jitter on the output; and they can remain locked to an atomic resonance frequency for hours at a time. With a workable design in hand, diode

lasers thus seem ideal for many atomic and optical physics applications.

## 3.3 Wavelength Selection

Because the experiment involves working with two tunable lasers (the diode laser and the Ti:Sapphire laser), it becomes both necessary and convenient to have some method of determining the output wavelengths at any given time. These wavelengths change with drive current, temperature adjustments, grating feedback tuning (for the diode laser), and etalon/birefringent filter changes (for the Ti:Sapphire laser). A wavemeter, which can measure the wavelength of a tunable laser to better than one part in a million, provides a simple method of wavelength determination.

#### 3.3.1 The wavemeter

The wavemeter was constructed by Hugh Robinson, based on a design by Hui-Rong, Benson and Hänsch [32]. It measures wavelength by comparing an unknown laser wavelength to the known 632.8 nm reference wavelength of a HeNe laser, where the reference wavelength is actively stabilized against thermal drift by equalizing the intensities of the two active orthogonal components of polarization (see Sec. 3.3.2). A schematic of the wavemeter is shown in Fig. 3.7. The basic components include a beamsplitter, two steering mirrors, and a moving cornercube retroreflector. Upon entering the interferometer, the beamsplitter divides both the unknown and reference beams into two equal intensity components. These travel down the arms of the interferometer and retroreflect from the moving cornercube. Because the beams travel down variable path lengths, when they recombine with themselves back at the beamsplitter inter-

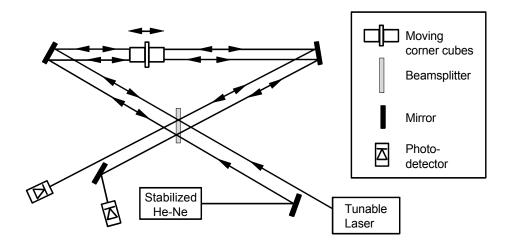
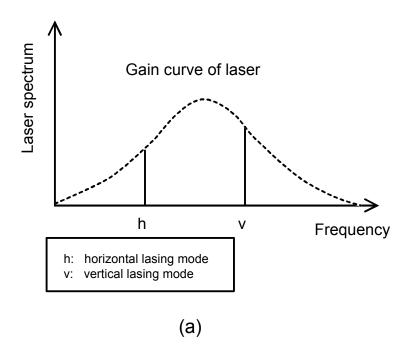


Figure 3.7: The wavemeter

ference fringes are formed. As the fringe pattern scrolls by with the motion of the cornercube, the fringes are detected and counted. The ratio between the number of fringes counted for the two lasers is used to calculate the wavelength of the unknown laser.

#### 3.3.2 Stabilized Helium-Neon Laser

As described above, the wavemeter measures unknown wavelengths through comparison with the known wavelength of a He-Ne laser. The stabilization of the He-Ne wavelength determines the ultimate precision of wavemeter measurements, so I built a He-Ne laser with active frequency control [33] in order to suit my purposes. If the cavity length is chosen correctly, the gain bandwidth of He-Ne gas lasers is such that two modes with orthogonal polarizations generally lase simultaneously. This is the case for our 7 inch laser tube, and Fig. 3.8a illustrates the two lasing modes in the laser spectrum. I split the



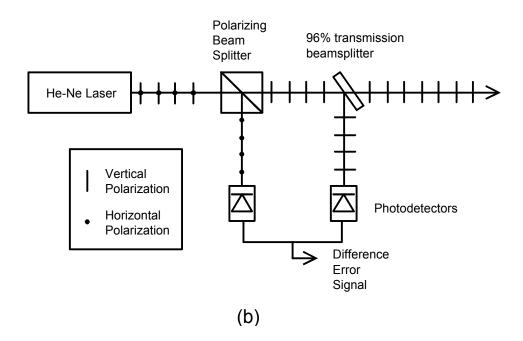


Figure 3.8: The polarization stabilization scheme

two polarizations into separate outputs and detect them with separate photodiodes as shown in Fig. 3.8b. Electronic circuitry generates an error signal by comparing the intensities of the modes, where a nonzero error signal indicates that the modes have different intensities, corresponding to being asymmetrically disposed under the gain curve. The error signal passes through a negative feedback loop which controls the laser cavity length, and hence the frequency, by heating or cooling the discharge tube.

Figure 3.9 shows a detailed schematic of the error electronics used in the laser. Light incident upon the photodetectors is subtracted and sent into a current-to-voltage converter. The signal passes through an inverting operational-amplifier equipped with an RC filter to prevent oscillations, and then enters the feedback loop. The feedback loop controls the laser current, and hence frequency, through a heater attached to the laser tube. The feedback cannot work, however, if the laser modes are far from their balanced position and hence outside of the domain of control for the loop. A preset constant bias voltage heats the laser close to a zero error signal so that when the feedback loop activates the laser will stabilize.

# 3.4 The Potassium Cell and Heat Pipe

Before discussing the potassium cell itself, it seems logical to explain why I chose to work potassium. The alkali atoms all share characteristics which make them ideally suited for Raman scattering work. They have a hyperfine-split ground state, where transitions between the ground state levels are easily induced. Raman transitions with ground states as the initial and final states are particularly nice to work with, as ground states have an effectively infinite

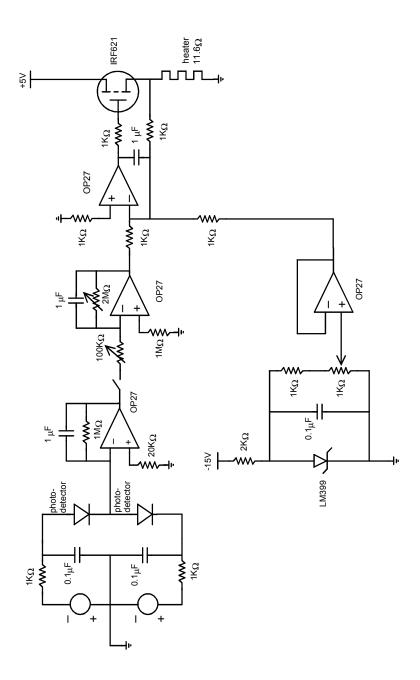


Figure 3.9: Stabilization electronics

lifetime (except for optical pumping), and thus a narrow linewidth. In addition, the alkali *D*-line transitions (transitions between the ground state and first excited state, generally at red to near-IR wavelengths) greatly enhance the Raman scattering probability. Potassium and rubidium are particularly easy to work with in this respect, as their excited state resonances are easily accessible using existing diode laser technology. After some exploration with both of these elements, I chose to concentrate my efforts on potassium-39, which has a smaller ground state splitting than either rubidium isotope (462 MHz versus GHz). At some point in the future, the grous expects to return to rubidium in order to characterize the effects of different ground state splittings in terms of two-photon Raman scattering. For the present, however, I have had exceptional success working with potassium.

Potassium, atomic number 19, is an alkali metal. It is solid and silvery in appearance at room temperature, with a vapor pressure of  $6.4 \times 10^{-10}$  mm Hg. It melts at  $63.5^{\circ}$ C and boils at  $758^{\circ}$ C. Its ground state configuration is  $4s^{1}$  around an argon-like inner core. Virtually all naturally occurring potassium occurs in two I=3/2 isotopes,  $^{39}K$  (93.26%) and  $^{41}K$  (6.73%). Due to the abundance of the  $^{39}K$  isotope I focus on it for these experiments, though the effects of  $^{41}K$  present in the sample cannot be experimentally neglected. Familiarity with the level structures of both isotopes thus proves helpful in spectral identification.

The relevant level structure of both potassium isotopes is shown in Fig. 3.10. The ground state isotope shift is 235 MHz. Both isotopes have a ground state hyperfine splitting, 461.8 MHz for  $^{39}K$  and 254 MHz for  $^{41}K$ . The transition of interest for this work is the  $D_1$   $4S_{1/2} \rightarrow 4P_{1/2}$  transition in  $^{39}K$ , where the  $D_1$  excited state has a radiative lifetime of 25.8 ns and a transition

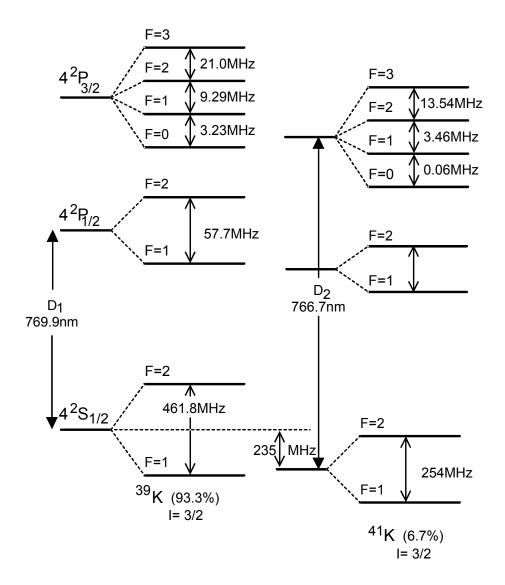


Figure 3.10: Hyperfine structure of the  $4^2S_{1/2}$ ,  $4^2P_{1/2}$ , and  $4^2P_{3/2}$  states of the two abundant isotopes of K. The isotope shift is 235 MHz and the excited-state lifetime is 25.8 ns.

wavelength of 7698.98 Å in vacuum. The electric dipole matrix element for the  $4S_{1/2}$  (F=1)  $\rightarrow 4P_{1/2}$  transition is  $\mu_o/\sqrt{2}$ , while that for the  $4S_{1/2}$  (F=2)  $\rightarrow 4P_{1/2}$  transition is  $\mu_o\sqrt{5/6}$ . I describe calculations of these matrix elements in Section 5.5.1.

Potassium is dangerous in contact with water, releasing hydrogen with sufficient heat to cause ignition or explosion. It may cause caustic and thermal burns if it comes in contact with eyes or skin, and can cause severe burns if ingested. Luckily, the potassium is well contained in its glass cell! The potassium cell is a 25 mm diameter, 75 mm long standard glass, natural-abundance potassium cell from Environmental Optical Sensors. The vapor pressure of potassium at room temperature is so low as to make it difficult to observe a resonant fluorescence or absorption signal. The vapor cell is heated to about 425 K (vapor pressure  $5.49 \times 10^{-4} \text{ mm Hg}$ ) in order to bring the number of atoms in the interaction region up to a workable density of about  $N=10^{13} \text{ atoms/cm}^3$ .

At room temperature, potassium appears as a shiny silver metal. If, during or after heating, the cell has a temperature gradient across some part of it of more than about 20°C, the potassium atoms preferentially condense on the coolest part of the cell. This is only acceptable if the coolest parts of the cell are *not* its windows – light generally does not travel well through metal-coated surfaces! Overheating the pyrex cell also must be avoided. Somewhere above 150°C, pyrex becomes soft enough that the alkali can embed itself in it, turning the glass black and effectively ruining the optical quality of the cell. In order to keep the cell at fairly even and controllable temperatures, it is placed in the heat pipe described below and illustrated in cross-section by Fig. 3.11.

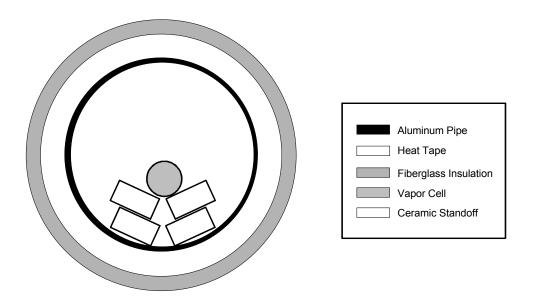


Figure 3.11: Cross-sectional view of the heat pipe and potassium cell

The heat pipe consists of a 6 inch diameter, 1 foot long aluminum pipe which was then wrapped with resistive heating tape. The pipe is significantly longer than the cell itself because it could only be directly heated around its circumference, yet the windows of the cell (nearest to the unheated ends of the pipe) needed to be kept warm enough to prevent condensation. The pipe was then insulated with glass fiber insulation and covered in aluminum foil to reflect heat. The ends of the pipe, though unheated, were well covered with insulation and foil and only had small holes in the covering in order to allow the laser beams to pass through unhindered. The cell itself was supported on a series of ceramic standoffs inside the pipe. Ceramic was chosen because it would not conductively transfer large amounts of potentially damaging heat to the cell. A thermistor was attached to the center of the cell, and an Omega CN370 temperature control unit used thermistor readings and electronic feedback to

control the temperature to an externally set value.

## 3.5 The Optical Layout

The optical layout for performing pump-probe spectroscopy in a vapor cell is detailed in Fig. 3.12. All of the previously described apparatus as well as all of the optical elements are mounted to a  $4' \times 12'$  Newport optical table. The probe laser beam exits the diode laser apparatus with an elliptical cross section. It immediately passes through a pair of Melles Griot anamorphic prisms which modify one axis of the elliptical pattern to circularize the beam shape. It is useful to circularize the beam so that focusing lenses work with more efficiency and less aberration, and for better overlap with the circular pump beam inside of the cell. The spot size upon exiting the prism pair is approximately 3 mm. Typically 3-5% of the probe laser power is lost upon passing through the prisms.

Two periscoping mirrors raise the probe laser beam height to that of the Ti:Sapphire beam and rotate the polarization perpendicular to the table. The laser beam reflects off of a steering mirror and then passes through a 400 mm focal length lens. The optical path length from the laser to the lens is approximately 110 cm. The beam focuses to a predicted beam waist of 65  $\mu$ m in the cell, another 25 cm downstream. A final steering mirror directs the beam into the side of a polarizing beamsplitter. Roughly 10% of the probe power is lost here. The beamsplitter combines the opposite polarization pump and probe beams along nearly copropagating paths. Alignment of the polarizing beamsplitter is a delicate task, as the beams must cross in the center of the cell with as much overlap as possible at an angle of less than 15 mrad. The

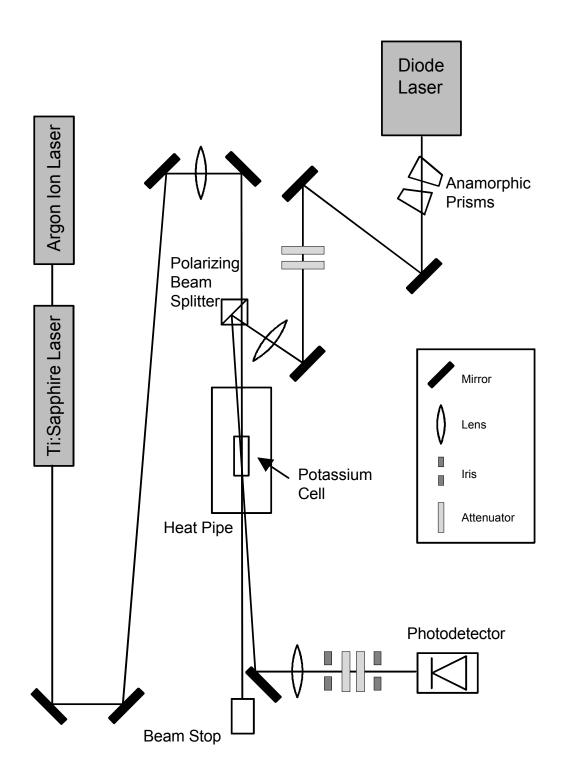


Figure 3.12: Experimental optical layout

crossing angle critically depends on both the position and angle of the probe beam upon entering the beamsplitter.

The pump (Ti:Sapphire) laser is emitted with a polarization perpendicular to the table, but four mirrors are immediately used to rotate the polarization  $90^{\circ}$  without changing the beam height. The beam is directed to the far end of the table with three steering mirrors, travelling about 3 m before being collimated with a 700 mm lens. Typical spot size on the lens is approximately 5 mm in diameter. The beam then passes through the polarizing beam splitter and into the cell. The predicted beam waist in the cell, about 70 cm from the lens, is  $150 \ \mu\text{m}$ , though self-defocusing effects have a pronounced, but not easily characterized, effect on actual beam size and shape.

Upon exiting the cell, the two beams are allowed to freely propagate for about one meter, separating them enough so that I can selectively pick off the transmitted probe beam for direction into a photodetector while allowing the pump beam to pass by into a beam dump. Once the transmitted probe beam has been captured, the beam is refocused so that the spot size on the photodetector is about 2 mm in diameter. The probe beam passes through two apertures as it approaches the detector to block off-axis light, since any stray or scattered pump light only adds excess noise to the signal. A linear polarizer placed in front of the detector screens unwanted pump light that makes it through the apertures and has not been depolarized through scatter or interaction in the cell.

Neutral density filters attenuate the probe beam in various amounts for various data runs. These attenuators are placed in the probe beam before entering the polarizing beamsplitter and/or in the transmitted beam before entering the detector. Special care needs to be taken in the placement of transmissive elements such as these on the table, because the effect of unwanted optical feedback into the lasers due to reflections off of lenses and neutral density filters can be quite pronounced.

# 3.6 Data Acquisition

Data collection consisted of varying an experimental parameter, such as probe laser power or pump-probe crossing angle, and then recording the transmitted probe field in the detection region. The transmitted field is characterized by the optical spectrum, measured as a function of frequency. The probe frequency is scanned up to 2 GHz by supplying the PZT on the back of the grating with a triangular wave, amplitude 0.1-10 V and frequency 10-12 Hz. For any given parameters, the probe intensity, crossing angle, and pump-probe overlap must all be optimized to observe the largest two-photon gain.

The time evolution of the transmitted probe intensities are measured using a fast UDT-020D photodiode. The detector has a built in current-to-voltage converter and a number of externally controllable gain settings for output amplification. The detector signal is monitored on an oscilloscope. It proves convenient to trigger the oscilloscope using the TTL output from the function generator in order to view a stable waveform as the PZT is scanned.

A 486 PC microcomputer serves as the central piece of the data acquisition system. It is equipped with a National Instruments AT-MIO-16 analog, digital, and timing I/O board and numerous software packages that facilitate collection and analysis of the data. The collection program was written using National Instruments LabVIEW for Windows software. LabVIEW is graphi-

cal based programming system which has application specific libraries for data acquisition and storage and allows easy adjustment of data collection parameters through an interactive user interface. The TTL function generator pulse triggers the program to accept a waveform which reproduces the observed oscilloscope trace. Typical scans take 2000 data points at a rate of 20,000 point/sec, corresponding to a frequency resolution of about 2 MHz per data point. The data is then written out to a file in a form usable by other graphing and analysis programs. Jandel Scientific's Sigma Plot for Windows was used to graph and analyze the collected data. Subtracting out background light, calibrating the frequency scan, and calculating the gain is all straightforward using the capabilities of this program.

# Chapter 4

# **Experimental Procedures and Results**

Previous chapters reported on the theoretical basis and the equipment used in our current work developing a new two-photon gain medium. This chapter discusses experimental procedures and results in this endeavor. I perform pump-probe spectroscopy in a potassium vapor cell and look at the transmission spectrum of the probe wave interacting with a strongly driven atomic vapor when the probe wave is nearly copropagating with the driving field. I characterize the transmitted field through a measurement of the probe intensity as a function of probe frequency. I explain all of the features in the probe-beam transmission spectrum, including the appearance of amplification due to two-photon Raman scattering. The experimental results described in this chapter are compared with theoretical predictions in Chapter 5.

Before delving into the experimental nitty-gritty, I once again emphasize the accomplishment this work represents. I have seen  $\sim 30$  % two-photon gain, easily surpassing the best previous results of  $\sim 0.1$  % seen in a dressed-atom gain medium. This success is in large part due to the relative insensitivity of the Raman scattering process (upon which our gain is based) to broadening

mechanisms. As a result the gain features are very narrow, allowing us to resolve features on a MHz scale. Previous work displayed two-photon gain on a large background of one-photon gain, while in our experiment the gain features are well separated and spectrally resolved.

### 4.1 Review of Raman Scattering

A brief review of Raman scattering in potassium, our atomic gain medium, follows. Understanding Raman scattering is important for our experiment, which observes significant two-photon gain in a new type of laser-driven two-photon optical amplifying medium based on a two-photon Raman scattering process. The initial and final states used in the Raman transition are the F=1 and F=2 hyperfine sublevels of the  $4S_{1/2}$  <sup>39</sup>K ground-state manifold.

One-photon Raman Stokes scattering, shown in Fig. 4.1a, involves one pump photon  $\omega_d$  and one scattered probe photon  $\omega_p$  in making a transition from the initial state  $| a \rangle$  to the final state  $| c \rangle$  via a virtual state associated with the excited state  $| b \rangle$ . In order for a one-photon Raman transition to take place between these states, the difference frequency of the applied fields (i.e., the probe-pump detuning frequency) must equal the 462 MHz hyperfine frequency splitting of the ground states. Application of a strong driving field at  $\omega_d$  then generates new scattered frequencies at  $\omega_p = \omega_d \pm 462$  MHz. The intensity of the scattered signal increases with the pump intensity until saturation occurs. In our system, the scattering process amplifies the radiation at the frequency  $\omega_p = \omega_d - 462$  MHz because optical pumping has created a population imbalance in which state  $| a \rangle$  is more populated than state  $| c \rangle$ . This will be further discussed in Section 4.3.2. The amplification is, of course,

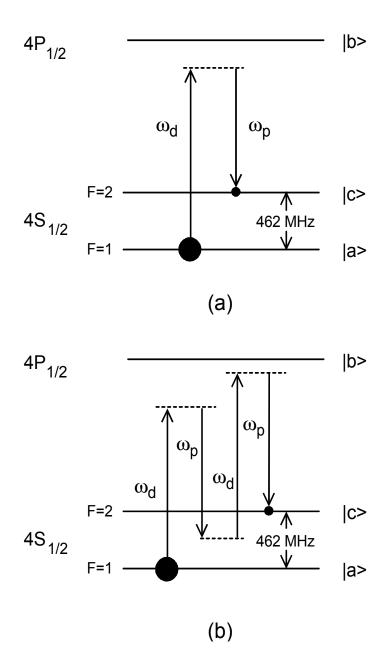


Figure 4.1: One-photon and two-photon Raman Stokes scattering in  $^{39}$ K. Larger dots indicate larger populations in the given states

at the expense of the pumping laser – one laser photon is lost for each Stokes photon that is created. Absorption is expected due to the corresponding anti-Stokes process, which involves a transition from  $|c\rangle$  to  $|a\rangle$  at frequency  $\omega_{as} = \omega_d + 462$  MHz. In our experiment, the inversion is not such that this process will, of itself, be amplified.

A two-photon Raman process is shown in Fig. 4.1b. It involves the absorption of two pump photons and emission of two Raman photons in making the transition between states |a> and |c>. The two-photon process occurs at frequency displaced from the driving field by half of the ground-state splitting,  $\omega_p=\omega_d-231$  MHz. The intermediate scattering level |b> nearly equidistant from each ground state serves to significantly enhance the transition. Even so, the two-photon Raman transition is a second order effect, and hence has a cross-section for occurrence far smaller than the one-photon cross-section. In addition, the two-photon gain coefficient is intensity dependent, differing from the usual constant gain coefficient fixed by the experimental parameters of the system.

The small cross-section and intensity dependence of two-photon gain lead to predictions concerning the expected gain behavior in the Raman system. For a typical transition the probe gain due to one-photon Raman scattering increases with the incident probe intensity until the saturation intensity is reached. The saturation intensity depends on a number of parameters<sup>1</sup> and is inversely proportional to the absorption cross-section/gain coefficient. Because the one-photon gain coefficient  $(B^{(1)})$  is much larger than that for two-photon

<sup>&</sup>lt;sup>1</sup>Recall that in Chapter 2 we defined  $I_{sat}=c\hbar\omega q_{sat}/V_c$  where the one-photon saturation photon number is found as  $q_{sat}^{(1)}=\gamma/2B^{(1)}$  and the two-photon saturation number is  $q_{sat}^{(2)}=\sqrt{\gamma/2B^{(2)}}$ .

gain  $(B^{(2)})$ , I expect the maximum gain (at the saturation intensity) to be quite large. However this gain saturates quickly, so high intensities will actually reduce the observed amplification. Because the cross section of a two-photon transition is so much smaller than that of a one-photon transition, the two-photon saturation intensity is much higher. The two-photon gain will then increase with probe power over a much larger range, but eventually it too may become saturated. At this point, there is the possibility of observing higher order multi-photon processes. To test these predictions, I look at Raman gain in the potassium cell as a function of probe power. The experimental procedures used are described below.

## 4.2 Single-beam Spectroscopy

Here I describe simple absorption spectroscopy in a glass potassium vapor cell. Initially absorption spectroscopy was performed as a test of the diode laser, and allowed determination of the laser's short- and long-term frequency stability and the tuning behavior of the laser frequency. I also optimized the laser temperature, current, and mechanical arrangement for smooth and stable operation. Later, finding and scanning about the potassium absorption resonance became part of the daily turn-on procedure for two-photon gain spectroscopy.

### 4.2.1 Tuning the diode laser to resonance

The diode laser first needs to be tuned to the resonant atomic transition. The procedure used, and that described here, is taken directly from the procedure given in the paper by Wieman *et al.* [28]. We tune the laser close to the known atomic transition wavelength as measured using the wavemeter; for best results,

we need to be within 0.5 Å of the transition wavelength at this stage.

We then pass a moderately strong beam through the cell, and observe its path using an IR viewer. In order to efficiently search for resonance, we wavelength tune the laser both by mechanically tuning the grating and by modulating the laser current. When the laser frequency is tuned within the Doppler profile of the absorption line, a strong track of fluorescence is visible in the cell. The current modulation is used so that if the laser has a tuning discontinuity that encompasses the desired wavelength, some point in the current modulation should still hit the right wavelength. Iteration of this procedure should produce results.

If grating and current tuning are unsuccessful in finding fluorescence, Wieman suggests that the temperature can be changed up or down slightly and the whole procedure repeated. I never found this to be necessary, however, because as long as the laser remained locked at the proper wavelength, grating and current tuning proved sufficient. (The few times it proved difficult to locate the atomic resonance, it was later discovered that the laser was running at its unlocked natural wavelength, many nanometers from the potassium resonance.)

The gross changes to the laser frequency induced by current modulation prove extremely useful for finding the initial fluorescence track. For spectroscopy, however, the probe laser output power should not vary as it does with current modulation. Instead, I stabilize on resonance using a *constant* current and then scan the laser frequency by tuning only the grating *position*,

which then alters the laser cavity length. To modulate the grating position, the PZT mounted to the back of the grating is driven with a 10-12 Hz, 10 V peak-to-peak, triangle wave from a function generator. A large DC offset keeps the modulation signal positive, necessary for keeping the PZT happy. Usually it is not difficult relocate the resonant fluorescence track after changing the frequency scan from one due to current modulation to one caused by a PZT scan at a fixed current.

Observation of a fluorescence track along the path of the laser beam through the cell indicates that the laser is within the Doppler profile of the absorption line. It does not, however, give any indication of how far in frequency the laser is scanning or whether the laser frequency is scanning smoothly. I derive this information by observing the beam transmitted through the cell with a photodiode detector and an oscilloscope. I trigger the oscilloscope from the function generator TTL output in order to get a stable display as the PZT drive is adjusted. As the laser frequency scans through resonance a dip should be seen in the transmitted beam intensity due to resonant absorption. On a practical note, in order to observe this dip the beam generally needs to be attenuated to prevent saturating the detector. The necessary attenuation is put in the beam before it enters the cell, both to prevent the optical transition itself from saturating and to increase relative change in signal strength due to absorption. The cell is also heated to increase the number density of interacting atoms, correspondingly increasing the absorption. Depending on the temperature and saturation properties, there may be anywhere from a 5-100% reduction in the signal as the laser scans through resonance. This is indicated in Fig. 4.2, which shows the single-beam absorption dip for differing cell temperatures.

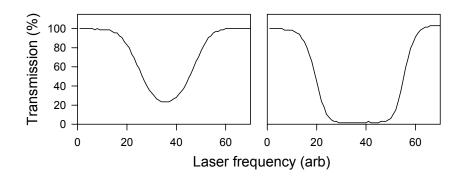


Figure 4.2: Single-beam absorption dip. (a) At low temperature the absorption dip profile appears Gaussian. (b) At higher temperature the absorption saturates.

#### 4.2.2 Scanning the atomic resonance

The goal now is to get the laser to smoothly scan at least 2 GHz about the absorption line, with few or no modehops. In a full 2 GHz scan, it is likely that "discontinuous steps of photodiode output occur across the oscilloscope trace, and part of the absorption dip may appear on a number of these steps. These steps, or mode hops, correspond to transitions from one longitudinal external cavity mode to another, and exhibit somewhat random spacing and hysteresis [28]." Figure 4.3 displays a typical frequency scan through resonance where the laser modehops near the center of the absorption dip. The lasing frequency after the modehop is again slightly to the red of the atomic resonance, and hence the laser scans the absorption dip a second time. There are various ways to try to reduce the number of mode hops and get a smooth scan about the resonant absorption line, most of which are rather unscientific and depend on

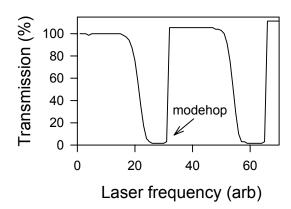


Figure 4.3: Diode laser frequency scan showing modehops

how well you commune with the laser on any given day. Small tweaks to the grating angle and diode drive current are the best methods for optimizing the wavelength scan. Adjustments to the laser temperature and the amplitude and offset of the modulation may also prove beneficial. Patience and luck are your best friends for this adjustment.

Oftentimes after the atomic resonance is found and the laser is smoothly scanning through it, the laser is not at its optimal operating current of about 75 mA (for the SDL-5401 lasers we use). It is best to try to run as close to the operating current as possible, because higher currents shorten the laser lifetime while lower currents reduce the power output of the laser. We do have some control over the current at which we can scan through the absorption resonance. Due to mode hops in the diode laser such as those just described, the atomic resonance is typically found simultaneously at several operating

currents periodically spaced by about 35 mA. Temperature tuning is used to shift a resonance until it occurs at or near the operating current. For example, the atomic resonance is often found at currents of about 50 mA and 85 mA, and either the 50 mA resonance needs to be shifted to higher current, or the 85 mA resonance to lower current. To shift an absorption line found at 50 mA up to higher current, recall that increasing laser current heats the laser. To track the resonance, we then further cool the laser and mount using the thermoelectric cooler (TEC) mounted beneath the laser baseplate. Similarly, to shift the 85 mA absorption line to a lower current, we reduce the laser current, cooling the laser. To compensate for this change, then slightly heat (or more accurately, cool less) the laser and mount. For this experimental setup, a TEC current between about 600 and 700 mA reliably chills the laser such that its locked wavelength is at (or very near) the atomic resonance when the laser is near its operating current<sup>2</sup>.

### 4.3 Two-beam spectroscopy

The absorption-dip spectroscopy described in the previous section is used to put the diode laser (probe laser) on resonance. Resonant absorption, such as that described above, appears with only a single beam incident upon the potassium cell. New effects become apparent when a second beam interacts with the first in the atomic medium. To study such interactions, we shine a second resonant laser in the cell and look at the effects of this pumping laser

<sup>&</sup>lt;sup>2</sup>Recall from Sec. 3.2.3 that because we do not actively temperature control the laser, the optimal TEC current will change slightly on a day to day basis due to changes in the ambient temperature. It will also change during the course of a day as the laser and mount heat up during use.

on the probe absorption. I previously described the optical layout for probepump spectroscopy in Sec. 3.5, and the new spectral features created by the probe-pump interaction will be described in a later section. First, though, a few of the details concerning both the second laser and the relative positioning of both lasers need to be discussed.

### 4.3.1 The pump laser

The actively stabilized Ti:Sapphire ring laser acts as the pump laser, and the first order of business requires locking the Ti:Sapphire laser to resonance. This involves first tuning the laser frequency close to the atomic resonant frequency by turning the laser's birefringent filter to approximately the right angle (given by the laser wavelength calibration) using the micrometer adjustment screw. A reading of 0.730 on the micrometer corresponds to 770 nm. Smaller frequency adjustments about this set point are made by scanning the thin etalon. Although the laser output can be directed into the wavemeter in order to explicitly read out the laser frequency, this is unnecessary unless the laser proves to be extremely uncooperative. Instead, we pick off about a 40 mW beam and direct it into the potassium cell. If the pump is set near the proper frequency, fluorescence from the atoms should be plainly visible as the lasing frequency is continuously scanned by up to about 25 GHz. Maximum pump output power at the potassium resonance is about 1 W.

Once both the Ti:Sapphire (pump) beam and the grating stabilized diode laser (probe) beam are on resonance, the two lasers are brought to a common focus in the center of our 7 cm long potassium vapor cell and are adjusted to cross at about a 12 mrad angle. Nearly copropagating beams are used in order

to get good probe-pump overlap throughout the length of the cell, and hence open the door for probe-pump interactions to take place. With the beams crossing in the cell, the pump laser now serves a dual purpose, simultaneously stimulating two independent processes to occur in the potassium atoms.

### 4.3.2 Optical pumping

First, the pump field optically pumps atoms from the F=2 to F=1 potassium ground-state hyperfine level ( $\Delta_{hfs} = 462$  MHz) as they move into the beam, thus creating the necessary inversion for gain to take place. Optical pumping is a pump-only effect – like resonant absorption, it requires only a single laser beam. The pump beam interacts with both atomic ground states and causes potassium atoms that drift into the strong pump beam to have their populations modified such that a large fraction of the atoms are moved to their lowest ground state.

The basic premise behind optical pumping is fairly straightforward. Potassium has two closely spaced ground-state levels between which the unexcited atoms in any sample are virtually equally distributed<sup>3</sup>. Optical pumping utilizes the fact that absorption and scattering of resonant light can lead to large population imbalances in atomic ground states and excited states. In our case, the pump laser frequency is slightly red detuned from resonance. "For [red] detuning the pump-field absorption rate for the F=2 state is larger than that

$$\frac{N_2}{N_1} = \exp\left(-\frac{E_2 - E_1}{kT}\right) .$$

However, with the ground state frequency difference of only 462 MHz, we calculate  $N_2/N_1 = 1.0001$  near room temperature, a negligible population difference.

<sup>&</sup>lt;sup>3</sup>Boltzmann's principle states that the relative populations of any two energy levels  $E_1$  and  $E_2$  in a collection of atoms in thermal equilibrium at temperature T is given by

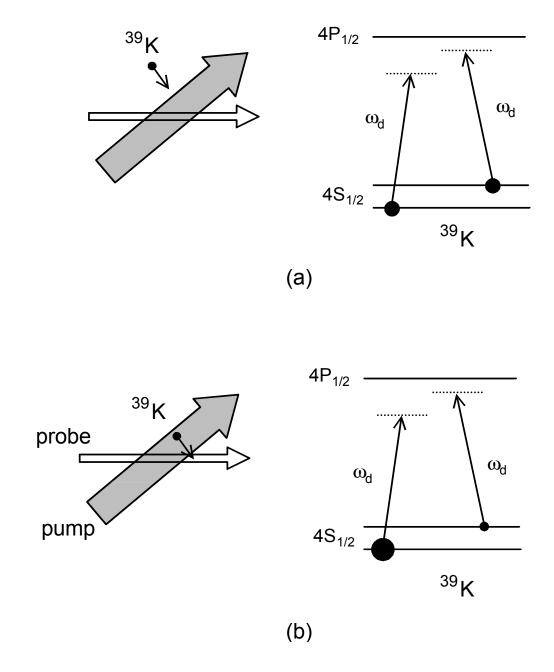


Figure 4.4: The effect of optical pumping on the potassium ground-state populations. (a) The ground state populations are evenly distributed in thermal equilibrium (i.e., when the atom is not interacting with any light fields); (b) The accumulation of population in the lowest ground state due to optical pumping.

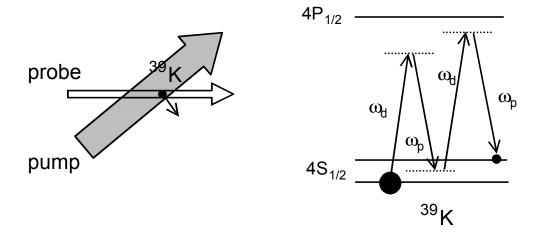


Figure 4.5: Raman scattering resulting from pump-probe interactions

for the F=1 state, whereas the decay of the excited  $[P_{1/2}]$  state into F=1 and F=2 states is determined by the branching ratio, which is independent of frequency detuning" [34]. This cycle serves to preferentially populate the F=1 ground state. Note that the unequal population distributions offers the opportunity to see optical gain due to population transfer from the F=1 to F=2 ground state.

### 4.3.3 Stimulating field

In addition to optical pumping, the pump beam also acts as the field which supplies photons to initiate the two-photon Raman process. When the optically pumped atoms move into an area filled by both the pump beam and the probe beam, new interactions are stimulated due to the presence of multiple, nearly-resonant light fields. Processes such as one- and two-photon Raman scattering result from probe-pump effects in which both beams play an integral role. Figure 4.5 schematically indicates the appearance of probe-pump effects. The

relationship between optical pumping and Raman scattering proves critical in our results. *Gain* on the Raman transitions requires a population inversion between the potassium ground states.

### 4.3.4 Probe-pump alignment

The probability of probe-pump interactions like Raman scattering processes taking place relies on good probe-pump alignment and overlap in the cell. In addition, for best results the diode laser output should be linearly polarized orthogonal to the pump laser<sup>4</sup> and the relative pump and probe beam intensities must be carefully controlled. I use a 700 mm focal length lens to collimate the 920 mW pump beam to a beam waist of 64  $\mu$ m (intensity 1/e radius) as it passes through the cell, corresponding to intensities of about 7 kW/cm<sup>2</sup>, and a 400 mm focal length lens to collimate the probe beam to a predicted diameter of 28  $\mu$ m (intensity 1/e radius) inside the cell<sup>5</sup>. I study the normalized transmission of a probe beam through the cell as a function of its frequency for several different probe beam powers, and vary actual probe power levels using neutral density filters. The probe laser has a maximum output power of about 10 mW, of which about 3 mW are always lost before the beam enters the cell. I further attenuate the beam with filters ranging from optical densities of zero to 2.6 (transmittances from 1 to  $2.5 \times 10^{-3}$ ), giving predicted probe beam intensities between about 0.71 W/cm<sup>2</sup> and 285 W/cm<sup>2</sup>.

Relatively small angles are maintained between the beams in order to opti-

<sup>&</sup>lt;sup>4</sup>A study of the relevant product matrix elements for one-photon Raman transitions shows that linear orthogonal polarizations of the pump and probe laser beams maximizes the transition probability[35].

<sup>&</sup>lt;sup>5</sup>As described in Section 1.3, there is a fair amount of uncertainty in the calculated beam sizes of both the pump beam and the probe beam due to self-defocusing effects in the cell that are difficult to quantify.

mize the region of pump-probe overlap in the cell. A secondary benefit of small crossing angles is that they effectively eliminate the Doppler contribution to the Raman linewidth. Raman interactions involve pairs of photons in making a transition between atomic states, where the transition takes place only when a resonance condition – the detuning  $\Delta_p$  between the incident laser beams is equal to the fixed ground state splitting of the atom – is satisfied in the reference frame of the atom. Yet in the special case where the pump and probe beams are copropagating, this detuning is unaffected by atomic motion.

Consider a pump-probe spectroscopy experiment in which the beams are copropagating and we account for atomic motion. A moving atom sees the pump and probe frequencies  $\omega_d$  and  $\omega_p$  Doppler shifted by almost an equal amount  $\omega_D$ , giving apparent laser frequencies  $\omega_d^D = (\omega_d - \omega_D)$  and  $\omega_p^D = (\omega_p - \omega_D)$ . The Doppler averaged pump-probe detuning, denoted  $\Delta_p^D$ , relevant for a Raman transition is then

$$\Delta_p^D = \omega_p^D - \omega_d^D = (\omega_p - \omega_D) - (\omega_d - \omega_D) = (\omega_p - \omega_d) = \Delta_p. \tag{4.1}$$

The effects of atomic motion have no effect on the detuning, thus allowing the Doppler broadening of an absorption line to be completely eliminated. Although copropagating beams or crossing angles significantly smaller than 12 mrad could not be used due to the appearance of four-wave mixing<sup>6</sup> processes, the small crossing angles used are still quite close to the ideal of perfectly copropagating beams.

In order to set the crossing angle, both the pump and the probe beam have two steering mirrors before entering the polarizing beamsplitter which are used for aligning and overlapping the beams in the cell. I relied on two

<sup>&</sup>lt;sup>6</sup>Four-wave mixing is described further in Section 4.7.

easy and commonly used methods for effecting this overlap. First, I look at the horizontal separation between the pump and probe beams at symmetric positions before and after the cell. The separation distance on either side of the cell should be equal, while the pump and probe beam positions should reverse, indicating a crossing in the cell. As a second check, I place a mirror at the cell entrance a distance x from the center of the cell, and reflect the two beams to an accessible location. If the beams are properly aligned, at a spot a symmetric distance x downstream from the mirror they will intersect and overlap.

### 4.3.5 Optimization of parameters

Once the lasers overlap and cross in the center of the cell, I scan the laser frequencies about the atomic resonant frequency and look for an indication of a significant pump-probe interaction, given by the appearance of new spectral features in the probe spectrum after exiting the cell. Because the optimal frequency at which to fix the pump laser in order to stimulate scattering processes is unknown, initially I scan the frequency of both lasers simply to increase the chances of noticing anything interesting. Once an interaction is seen, however, I fix the pump laser at a frequency red detuned from the atomic resonance (for optical pumping reasons) and only scan the probe laser. If the initial alignment is done carefully, distinct gain or loss features in the probe transmission spectrum near the atomic resonance frequency (i.e., within a few GHz) will be observed. Even if no features are seen at first, it usually not difficult to modify the beam crossing angle in order to create a more optimal beam crossing, and then, as if by magic, the interaction features will appear. If this proves difficult, the chance of good overlap is increased by removing the lens from

the pump beam, enlarging the beam in the cell. Because finding at least some small gain feature from which to start has never proved problematic, I have few other words of wisdom other than "Make sure the lasers are on resonance" and "Make sure the beams cross/overlap in the cell, not before or after it!" The initial locking of both lasers to resonance and finding a gain feature generally takes one or two hours.

### 4.3.6 One-photon Raman transitions

One-photon Raman transitions are one of the most common and easily identifiable pump-probe interactions. Because the Raman transitions in our experiment take place between two long-lived potassium ground states, and because Doppler broadening of the Raman transitions can be effectively neglected, the Raman gain features should be very narrow – only a few MHz full width at half maximum. The expected narrowness of these features will allow us to distinguish them from other scattering features which should appear much broader.

A first stab at optimizing the experimental parameters thus involves finding and optimizing the gain due to one-photon Raman transitions. Because the probe beam is focused so tightly, the beam intensities are high enough to saturate the one-photon Raman transition. As a result, in order to see the highest gains I strongly attenuate the probe beam before it enters the cell. The best results are seen with probe beam powers of less than 1  $\mu$ W. I then adjust the pump-probe crossing angle in the cell and the beam intensities by changing the positions and focal lengths of the lenses used to focus the beams. In addition, I test the effects of varying the detuning of the pump laser from the atomic resonance and set the pump at its approximate optimal detuning.

The detuning is non-zero because if it is too large, few transitions will be stimulated and the one-photon Raman gain will decrease, yet if the detuning is too small other nonlinear will processes dominate and swamp out the Raman gain. For best results (largest gain with fewest competing effects) the pump laser is tuned approximately 1.4 GHz below the 770 nm  $4S_{1/2}$  (F=1)  $\rightarrow 4P_{1/2}$  (F=2) potassium  $D_1$  transition. This detuning is small enough that we don't interact with the 766 nm  $D_2$  ( $4S_{1/2} \rightarrow 4P_{3/2}$ ) optical resonance. The optimal detuning is somewhat variable as other parameters are altered.

To further increase the one-photon Raman gain once the crossing angle, detuning, and intensities are set, the cell temperature is gradually increased to 150°C, corresponding to a number density of about 10<sup>13</sup> atoms/cm<sup>3</sup>. Higher temperatures correspond to higher number densities in the potassium cell, and with more atoms taking part in the transitions this increases the gain until saturation occurs. In one of our first experiments, we mapped out one-photon Raman gain versus temperature up to 150°C with a 1.3 mW probe beam, as shown in Fig. 4.6. We found continuing increases in gain over this full range, though perhaps early saturation effects are manifesting themselves at the highest temperatures. Increasing the temperature further should continue to increase the gain. However, we are reluctant to take the temperatures higher than the operating temperature of 150°C, because at much higher temperatures glass becomes soft enough that the potassium can embed itself in it and destroy the optical quality of the cell [36]. With only a single cell to work with, we could not perform our own tests of the temperature at which the cell is destroyed. However, future work in this area might warrant trials at higher temperatures.

The parameter optimization just described, including the strong attenua-

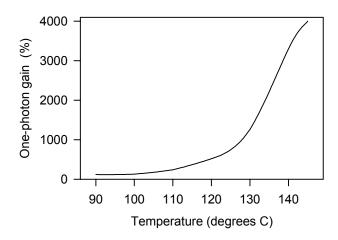


Figure 4.6: One-photon Raman gain as a function of cell temperature

tion of the probe beam, sets up our system such that high one-photon Raman gain is observed. In fact at times the gain is so high, >10,000%, that no other spectral features are seen above the noise level of the system! We tend not to go to extremes in this endeavor, however, since the parameters that give the best one-photon Raman gain are not identical to those giving the best two-photon Raman gain, and two-photon gain represents our eventual goal. The temperature and detuning can be set fairly accurately at this stage, and the crossing angle will only change slightly between the optimization of one-photon and two-photon Raman gain. The beam intensities, however, change dramatically, as one would expect since two-photon gain is an intensity dependent effect. Without modifying any other parameters, the next step involves increasing the probe beam power in order to get to a regime where one might expect to see

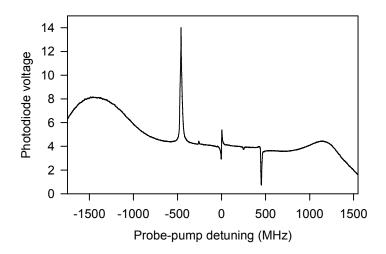


Figure 4.7: Typical probe transmission spectrum

two-photon Raman gain. First, however, Fig. 4.7 shows a typical probe beam output spectrum taken with an incident probe power of about 0.5 mW. A brief description of the general spectral features follows, as does a description of the data collection and analysis procedures used in creating this spectra.

# 4.4 General spectral features

Experimentally I measure the probe transmission spectrum as a function of pump-probe detuning. A typical spectrum is shown in Fig. 4.7, and has a number of easily distinguishable features. I interpret these resonances, starting from the left, as follows.

The large, spectrally broad amplification seen at both the far left and the far right are so-called Rabi resonances. These AC-Stark shifted resonances result from the shifting and splitting of atomic energy levels when the atom interacts with a strong electromagnetic field like our pump beam. I discuss Stark shifting in more detail in Chapter 5, but the general principles are illustrated in Fig. 4.8 [37]. For simplicity the Stark effect is illustrated for a two-level atom, but the ideas (though not the exact splittings) are equally applicable to an atom with more than two levels. A laser field at frequency  $\omega_d$  that is detuned from resonance by frequency  $-\Delta$  creates a pair of virtual atomic levels, shown as dashed lines. At high laser intensities, the energy-level structure is modified by the AC-Stark effect to become pairs of real levels separated by the generalized Rabi frequency  $\Omega'$ . Rabi resonances then result from a three-photon effect in which the atom simultaneously absorbs two pump-laser photons and emits a probe photon at frequency  $\omega_d + \Omega'$ , consequently making a transition to the excited state. As a result of this process, the probe wave experiences gain at the frequency  $\omega_p = \omega_d + \Omega'$ .

If I extend these principles to the potassium atom, I must include at least three levels in the treatment – each of the hyperfine split ground-state levels, as well as the excited state level<sup>7</sup>. In this case, each atomic energy level splits into three levels split by various frequencies that are functions of the pump detuning and the ground-state hyperfine splitting. A number of potential Rabi resonances are then predicted, because transitions can take place between each triplet of ground-state levels to any of the states in the excited state triplet. However, as a result of significant Doppler broadening in the medium only one very broad resonance is experimentally seen. The individual peaks are unresolvable and have been combined into a single broad feature. This is

<sup>&</sup>lt;sup>7</sup>In a careful treatment, the splitting of the excited state into two levels is also taken into account.

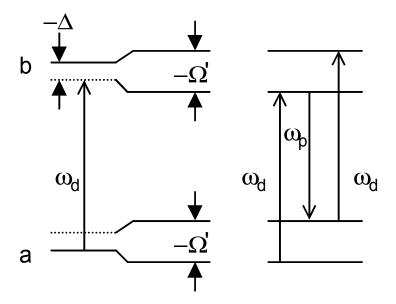


Figure 4.8: The creation of Rabi resonances in a two-level atom

theoretically verified in Chapter 5. Doppler broadening also causes the wings of the leftmost Rabi feature to create a non-zero, spectrally broad amplification throughout the region of two-photon gain. Eliminating this background effect is a priority in future work.

The tall, narrow peak shifted from the pump by about the 462 MHz groundstate hyperfine splitting of potassium,  $\omega_p = \omega_d - \Delta_{hfs}$ , is a result of saturated one-photon Raman Stokes gain [38] from <sup>39</sup>K and corresponds to the transition illustrated in Fig. 4.1a. The mechanics of Raman gain have been discussed earlier, and the observation of gain at this frequency simply indicates that the lower energy ground state must be the more populated one. The very small gain peak just to the right results from an identical one-photon Raman Stokes gain process occurring in <sup>41</sup>K, where the <sup>41</sup>K ground-state hyperfine splitting is  $\Delta_{hfs} = 254$  MHz. This feature is much smaller than that of <sup>39</sup>K because the natural abundance of  ${}^{41}K$  is only 6.7%.

The dispersive-shaped feature near zero detuning in the transmission spectrum represents stimulated Rayleigh gain (and absorption) due to population oscillations between the ground state hyperfine levels [39]. Rayleigh gain only occurs when the pump-probe detuning is less than the inverse of some characteristic response time. The superposition of the pump and probe beams inside the atomic medium creates a beating field, where the beat frequency is equal to the pump-probe detuning. The response time of the atomic medium sets the time scale of field fluctuations that the atom can effectively follow. The frequency response of the atom is then given by the inverse of the response time. When the detuning, and hence the beat frequency, is larger than the frequency at which the atoms can respond, the atoms see only the constant, averaged field. When the pump-probe detuning is small enough to be shorter than the frequency response of the atoms, however, the atoms see the varying field and the populations of the atomic levels can couple with the strong beat frequency. An atom may then absorb a pump (or probe) photon and re-emit a probe (or pump) photon without changing energy levels, thus cycling population between the ground state and some excited virtual state. The line shape of this Rayleigh scattering process appears dispersive whenever the pump is detuned from resonance. This has been explained in terms of the frequency dependence of the oscillation probability [40, 41].

The spectrum has a distinct symmetry about the dispersive Rayleigh resonance centered at a probe-pump detuning of zero. On the blue side of the Rayleigh resonance (positive probe-pump detunings), the Raman scattering taking place transfers population from the F=2 to F=1 ground state, as shown

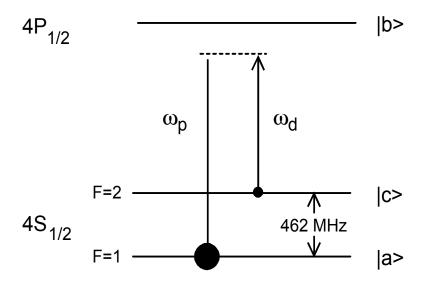


Figure 4.9: Anti-Stokes Raman scattering

in Fig. 4.9. Optical pumping has already depleted the F=2 state, and hence I observe loss rather than gain due to these anti-Stokes Raman scattering processes. The small absorption dip and larger narrow dip correspond to one-photon Raman anti-Stokes loss of  $^{41}K$  ( $\omega_R = \omega_P + 254$  MHz) and  $^{39}K$  ( $\omega_R = \omega_P + 462$  MHz), respectively. The rightmost broad peak is then the Rabi resonance already discussed. In many of the spectra, this last Rabi resonance is superposed on the leading edge of the Doppler broadened resonant absorption dip, explaining the decrease in the transmission spectrum at the largest blue detunings.

To summarize, at relatively low probe beam powers ( $\sim 0.5$  mW) spectral features include the standard one-photon Raman Stokes and anti-Stokes processes (one-photon Raman resonances) at probe-pump detunings equal to the atomic ground-state splittings. A dispersive Rayleigh resonance is found around the point of zero probe-pump detuning, and broad Rabi resonances

are seen at frequencies displaced from the pump by an amount related to the generalized Rabi frequency.

## 4.5 Data Analysis

While optimizing experimental parameters in the system, I observe the transmitted probe beam power as a function of probe frequency in real time using an oscilloscope attached to a photodetector that looks at the probe beam after exiting the cell. When taking data such as that shown in Fig. 4.7, however, I send the photodetector signal directly to an IBM 486 clone for data storage and analysis. The collection program mimics the output of a digital storage oscilloscope.

The data for a given set of experimental parameters involves collection of three individual data scans: the probe transmission spectrum taken with both beams passing through the cell; the probe beam absorption spectrum, recorded with the pump beam blocked; and a baseline of scattered pump light recorded with the probe beam blocked. Using simple data transformations and manipulations I calculate the actual probe gain and the frequencies of the resonance features. A polarizer in front of the detector blocks pump light that has been scattered by the cell windows into the direction of the probe beam. Additionally, unwanted, scattered light is minimized before reaching the detector by using apertures in the probe beam to block stray pump light from the probe beam output. In order to eliminate background light that has escaped these measures, I subtract the measured pump-beam background signal from the desired probe transmission signal. The probe-only spectrum then defines a zero-line for gain calculations (y-axis in all of our data): wherever

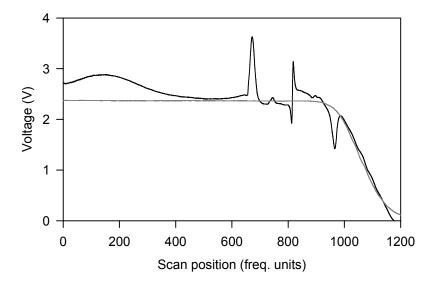


Figure 4.10: Illustration of data used for gain/loss calculations. The gray line is the probe-only spectrum. Pump-probe features from the full spectrum that are above this line represent gain; features below the line represent loss.

the transmission spectrum is above this baseline, the probe beam has experienced gain; below this line it has experienced loss. This is illustrated in Fig. 4.10, which shows a typical (non-optimized) data spectrum superposed on the baseline probe absorption dip. I have normalized the probe transmission to the measured transmission of the probe beam in the absence of the pump beam with the probe laser detuned well outside the wings of the Doppler broadened absorption line.

The x-axis, collected in uncalibrated units representing the frequency scan of the diode laser, is converted to real frequency units as follows. First, I make the assumption that the PZT motion moving the grating leads to a linear

frequency scan of the laser. This turns out to be a very good approximation, as the Burleigh PZTs are guaranteed linear to better than 4%. I then assign 462 MHz to the frequency between the one-photon Raman gain feature and the Rayleigh scattering feature at the pump frequency, where the difference is taken between the peak of the Raman gain and the point at which the central slope of the Rayleigh scattering feature crosses the line of exactly 100% probe transmission. This calibration sets the entire frequency scale. I neglect the small amount of Stark shifting and level splitting seen at our operating Rabi frequencies that would serve to modify the frequency scale.

### 4.6 Spectra versus probe power

At this point we are on the brink of some very exciting physics. The experimental parameters leading to the best one-photon Raman gain have been optimized, and we are prepared to study the gain as a function of probe power. As has probably become clear, pump-probe spectroscopy is relatively straightforward in terms of the necessary equipment (lasers, optical apparatus, and such) and optical layout. The largest difficulty, and the part which requires a great deal of patience, concerns the endless adjustment of the beam crossing angles, intensities, and focus points in order to optimize the spectral features of interest. This optimization has already been performed for one-photon Raman gain. As the probe laser intensity increases, however, we expect to see the appearance of two-photon Raman gain, and this two-photon process will serve as the focus for the rest of our work.

In order to study the probe transmission spectrum as a function of probe intensity, I took a series of data sets with differing amounts of attenuation in

front of the cell. The filters serve to adjust the probe intensity without changing any of the other experimental parameters. I did, however, continually check that the insertion of the filters into the probe beam did not steer the beam enough to make any noticeable change in the transmission spectrum due to crossing angle modifications – all changes resulted from power level differences. In what follows, I specify the *power* in the probe beam rather than its intensity since the effects of self-defocusing and defocusing of the probe beam by the gradient index of refraction set up by the pump beam make it difficult to know the exact spatial profile of the probe beam in the cell. This then makes a calculation of the beam intensities rather uncertain, while I easily measure the probe power incident upon the cell.

A typical low-probe-power data plot is taken with filters totalling an optical density of 2.6 (transmittance  $2.5 \times 10^{-3}$ ) in front of the vapor cell, yielding an incident probe power of  $15\mu$ W. We observe large (>5000%) amplification of the probe laser due to one-photon Raman scattering when  $\omega_p \approx \omega_d - \Delta_{hfs}$ . Even at these low powers, however, the gain is saturated – as I continue to attenuate the probe beam the maximum one-photon amplification increases rapidly. I have not yet reached the limit of one-photon amplification at the weakest probe power levels, yet the sensitivity of our detection system prevents me from going much below a probe power of  $1\mu$ W, which gives an incredible 14,000% gain! At these large gains, the full width at half maximum of the gain peak is very narrow, only a few MHz. As the laser power increases, the one-photon Raman resonances decrease in peak height due to saturation and increase in width due to power broadening. At a probe power of about 2 mW

the width has increased to about 50 MHz<sup>8</sup>.

So far I have concentrated exclusively on the one-photon Raman resonances, yet changes in the probe power affect a number of the other resonant features as well. The peak of the Rabi feature appears to move to smaller probe-pump detunings at higher probe laser powers. I do not have a good explanation for this, as we would expect this feature to move to larger detuning at higher pump intensities due to the correspondingly larger Stark shifts increasing the resonant Rabi frequencies. Large probe powers/intensities can affect the atomic levels, but again one would intuitively expect higher beam intensities to increase the probe-pump detuning at which we observe resonance. This problem will be further explored in the next chapter, where I explore a theoretical model of our system. The final important effect to note concerns the appearance of new resonances as the probe intensity is increased high enough.

### 4.6.1 Demonstration of two-photon gain

Figure 4.11 shows a sequence of measured transmission spectra for several different probe laser powers<sup>9</sup>, and Fig. 4.12 displays the same data over a smaller detuning range. The spectral features described in Section 4.4 are the only resonances that occur at low probe beam powers. As the laser power increases, however, the main Raman resonance shows power broadening effects and the gain profile exhibits the emergence of resonances at subharmonics of the ground-state splitting. I attribute these intensity dependent spectral features

<sup>&</sup>lt;sup>8</sup>Recall that working with small angles between the beams effectively eliminates the Doppler contribution to the Raman linewidth. Residual width may derive from power broadening (at high beam intensities) and frequency jitter between the two lasers.

<sup>&</sup>lt;sup>9</sup>This series of spectra was actually taken after optimizing the two-photon gain, as described in the next paragraph.

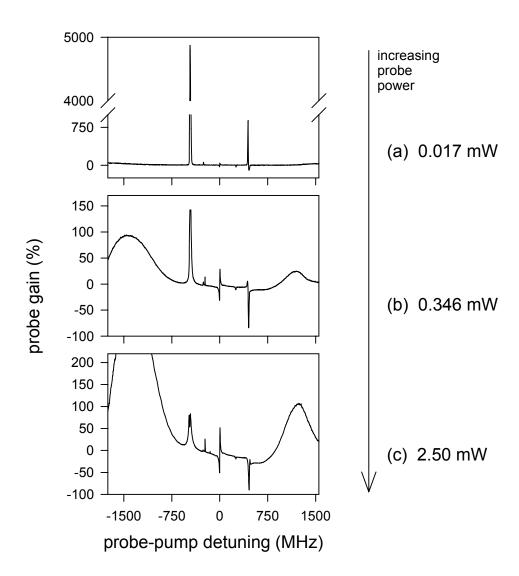


Figure 4.11: Wide-view showing dependence of the probe transmission spectrum on probe beam power.

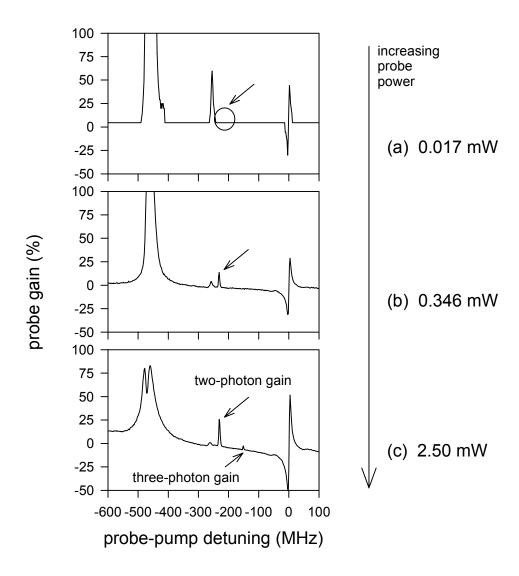


Figure 4.12: Detail showing the dependence of the probe transmission spectrum on probe beam power.

to two- and three-photon gain. High probe powers (and correspondingly high intensities) are essential to bring the nonlinear gain into operation because two- (and three-) photon scattering has an intensity dependent cross-section.

Once the probe power is increased enough to observe two-photon gain, I readjusted all of the experimental parameters in order to optimize the two-photon gain feature. This is the point at which parameters originally set to optimize one-photon Raman gain are adjusted to optimize two-photon Raman gain. The sequence of measured transmission spectra displayed in Figs. 4.11 and 4.12 were taken by again swapping neutral density filters into the system to vary the attenuation after I had already optimized the two-photon gain. I need to emphasize the importance of patience for this optimization. In a span of perhaps 15 minutes, initial tweaking can create conditions displaying 3-5% two-photon gain. Increasing the gain beyond this point, however, can often take hours. For this optimization, the crossing angle and the lenses setting the pump and probe beam intensities are the most critical parameters. Moving a focusing lens a centimeter toward or away from the cell or adjusting the crossing angle by as little as 1 mrad can make a significant difference in the observed gain.

The Raman gain shown in the spectra of Fig. 4.11 display all of the expected behaviors. Because two-photon gain is intensity dependent, the two-photon amplification increases with increasing probe-beam power until saturation occurs. On the other hand, the one-photon gain saturates quickly, so high intensities actually reduce the amplification. This progression is evident in Fig. 4.11a-c. As I approach probe powers of about 1.5 mW, the one-photon Raman gain decreases dramatically and a new gain feature appears at

 $\omega_R \approx \omega_P - \Delta_{hfs}/2 = \omega_P - 231$  MHz. I attribute this new feature to two-photon Raman-based optical amplification because it occurs at the expected frequency and it is not present for low probe-beam intensities, as expected for the two-photon stimulated emission process. I should note that in order to see the largest two-photon gain, I actually had to attenuate the probe beam, and even when attenuated the intensity was large enough to saturate the two-photon transition, as evidenced by the appearance of a small peak at frequency  $\omega_R \approx \omega_P - \Delta_{hfs}/3$  which I attribute to three-photon Raman amplification ( $\sim 5\%$  gain). Just as two-photon gain only appears once the one-photon gain has been saturated, three-photon gain appears only after the two-photon gain has been saturated. The three-photon gain peak disappears as the probe intensity is lowered below the two-photon saturation intensity.

Our best results show  $\sim 30\%$  two-photon amplification of the probe beam in a single pass through the cell, as shown in Fig. 4.13. As mentioned before, this is two orders of magnitude higher than previously observed gain of  $\sim 0.1\%$ . Thirty percent gain should be sufficient to observe two-photon lasing once we put a cavity around the vapor cell, though of course higher gain would be even better.

What might we be able to do in order to increase the observed gain beyond the 30% I have already measured? I believe a limiting factor in the gain seen involves the rate at which optical pumping can transfer atoms from the F=2 to F=1 potassium ground state. Raman gain transitions transfer atoms in the opposite direction, from F=1 to F=2. At high gain rates where the Raman transfer rate from F=1 to F=2 is quite fast, optical pumping may not be able to maintain the necessary inversion, thus capping the maximum gain. Increasing

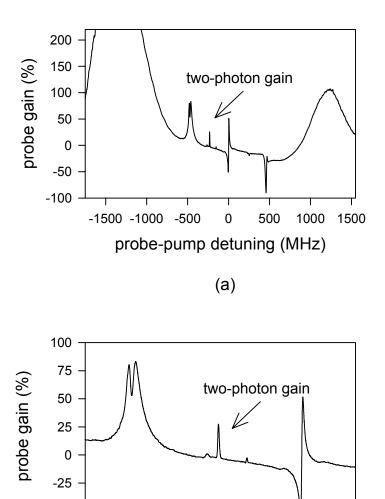


Figure 4.13: Demonstration of 30% two-photon Raman gain

probe-pump detuning (MHz)

(b)

-600 -500 -400 -300 -200 -100

100

-50

the optical pumping rate (as described in Chapter 8) thus has potential for increasing the two-photon gain beyond our best to date.

As a final observation, I note that the two-photon Raman gain from  $^{39}K$  at  $\omega_R \approx \omega_P - 231$  MHz and the one-photon Raman gain from the  $^{41}K$  isotope at  $\omega_R \approx \omega_P - 254$  MHz are separated by only 23 MHz, yet are spectrally resolved from each other. In the work with dressed-state two-photon lasers, the two-photon gain was not even spectrally resolved from the one-photon gain caused by the *same* isotope over 200 MHz away. The gain I observe is thus even more impressive due to the excellent resolution of all of the spectral features, and in particular the spectral isolation of the two-photon gain.

## 4.7 Four-wave mixing

Despite the impressive data shown above and the theory that will be described in the next chapter substantiating our results, there are those who would claim that we have not observed gain due to a pure two-photon stimulated emission process, but rather see gain due to a parametric interaction such as four-wave mixing (FWM). In 1981 a research group thought they had demonstrated two-photon lasing [42], but it was later realized that the observed effect was due to a parametric process. It has since become well recognized that gain seen as a result of multi-photon parametric process can mimic true gain processes. Due to this original case of mistaken identify, in two-photon gain and lasing experiments it has become extremely important to prove that the gain is due to some type of true two-photon stimulated emission and not due to wave-mixing or other parametric processes. Because four-wave mixing requires phase matching of the four beams involved, this can serve as a distinguishing characteristic

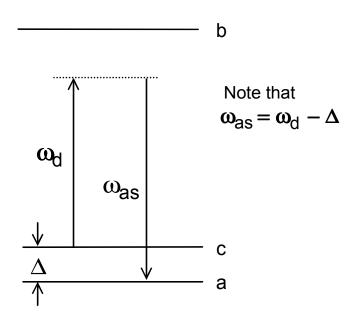


Figure 4.14: Anti-Stokes Raman scattering

between FWM processes and pure gain processes that do not have such a requirement.

A brief description of the relevant FWM process and its relationship to anti-Stokes Raman scattering seems in order. Anti-Stokes Raman scattering is shown in Fig. 4.14, where the scattered photon has a frequency higher than the incident photon<sup>10</sup> by the amount shown. Generally the anti-Stokes resonance, which appears at a probe frequency blue detuned from the pump, will show loss in our system because optical pumping has decreased the population of level c such that it is much smaller than the population of level a. Yet there is a FWM process that can demonstrate gain at the same frequency as the anti-Stokes resonance, as shown in Fig. 4.15. An interaction between the pump wave at

<sup>&</sup>lt;sup>10</sup>For simplicity, most of the following description deals explicity with the one-photon Raman Stokes and anti-Stokes processes. All of the ideas, however, are equally applicable to twophoton processes.

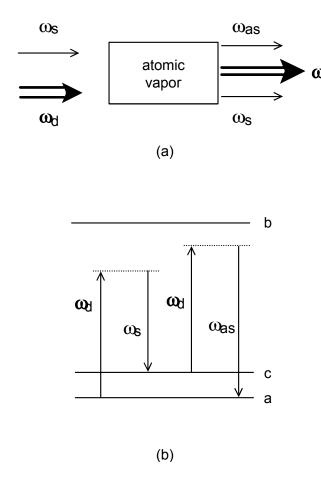


Figure 4.15: The mechanics of four-wave mixing

frequency  $\omega_d$  and the Stokes wave<sup>11</sup> at frequency  $\omega_s$  (generated by the Raman scattering process described earlier) initiates the FWM scattering process, so significant Raman scattering must have already built up a strong wave at the Stokes frequency before this FWM process takes place. The nonlinear response of the medium to the pump and probe waves then generates a field at the anti-Stokes frequency  $\omega_{as}$ . In this four-photon parametric process which returns

<sup>&</sup>lt;sup>11</sup>This is exactly the red-detuned frequency at which we have observed one-photon gain, while in our system the anti-Stokes frequencies occur on the blue side of resonance at positive probe-pump detunings.

the atom to its original state, two pump wave photons are annihilated, one photon is added to the wave at the Stokes frequency, and one photon is added to the wave at the anti-Stokes frequency. This actually creates the wave at the anti-Stokes frequency, while that at the Stokes frequency is amplified.

There have been a number of both theoretical and experimental studies on four-wave parametric interactions resulting from the non-linear response of a two-level atomic system [43]. If I adapt these treatments to the three-level system at hand, it can be shown that optimum generation at the Raman Stokes frequency requires a very large phase mismatch between the pump, probe, and Raman generated waves. This effectively decouples the waves so that the Stokes wave grows due to pure Raman scattering (non-phase matched), while absorption is seen at the anti-Stokes frequency. This point deserves to be emphasized: Raman Stokes scattering is a "pure" gain stimulated emission process, and as such does not depend on the relative phase differences between the pump and the probe fields.

However, anti-Stokes gain can occur and can in fact be quite large, but it appears only as a result of Raman-resonant four-wave mixing, which becomes significant only when the driving field, Stokes field, and anti-Stokes field are nearly phase-matched. Figure 4.16 diagrams the relationships between the waves (a) when they are exactly phase matched and (b) when there exists a measurable phase mismatch. In general optimal Stokes gain will not occur at perfect phase matching [44], so we can conclude from these studies that we should not expect FWM to occur when the Raman Stokes wave is optimized (as it is in our experiment).

What do I actually see experimentally, and in particular what do I observe

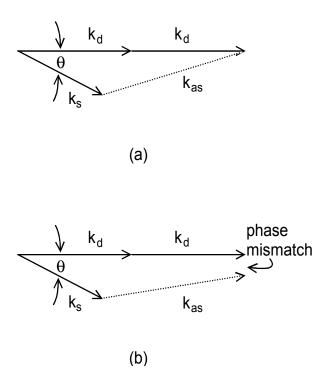


Figure 4.16: Phase matching requirement for anti-Stokes Raman scattering taking place at the anti-Stokes Raman frequency? Whereas in general anti-Stokes Raman scattering shows absorption, at small angles when the pump, probe, and output waves can become phase matched it may display gain. In some cases, we observe anti-Stokes gain as large as 50% of the Stokes gain! In addition, due to Stokes-anti-Stokes coupling as the anti-Stokes gain increases gain at the Stokes frequency may increase as well. Any such increase is, however, by definition *not* due to pure two-photon Raman scattering, and hence represents a competing process we need to avoid.

Small crossing angles (where phase matching becomes possible) prove very interesting in terms of the changes they produce in the probe transmission spectrum. Strange background features appear and cause the observed scat-

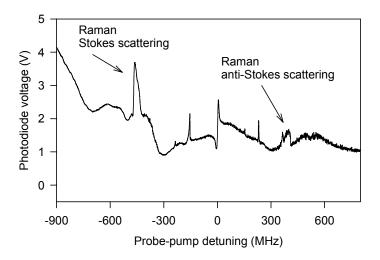


Figure 4.17: Probe transmission spectrum showing some effects of four-wave mixing

tering features to be superposed on wavy nonuniform baseline, rather than the steady, smooth baseline typically seen. A probe transmission spectrum displaying some four-wave mixing effects is shown in Fig. 4.17. The change from a smooth background to a wavy one is rather abrupt and hence easily experimentally identifiable. It thus proves straightforward to avoid these regions where the FWM processes become prevalent.

As well as displaying a crossing angle dependence, for a given crossing angle I am able to identify experimentally different pump detunings that lead to significant anti-Stokes gain. Changing the detuning parameter modifies the phase of the waves, hence altering the phase mismatch. When the phase mismatch is small enough as to give large anti-Stokes amplification, the four-

wave mixing and other competing effects that take place again severely alter the probe transmission spectrum. If I then tune to larger phase mismatches, the four-wave coupling decreases and decreases the anti-Stokes wave accordingly. In many cases, at phase-matched crossing angles and detunings the features at the two- and three-photon gain frequencies appear quite large<sup>12</sup>, which might initially seem to be ideal. However, because their symmetric features on the blue side of resonance (at the anti-Stokes frequencies) also display gain rather than the loss that would be expected for non-phase-matched scattering, this indicates that much of the amplification is due to FWM and not pure Raman scattering. Again I steer away from regions of high FWM. At what we deemed the optimal detuning and crossing angle (used for the data displayed in Fig. 4.13), the spectrum shows only minor gain at the anti-Stokes frequency due to a FWM parametric process and it seems clear that the majority of the gain is due to pure Raman scattering.

Although I make the claim that the majority of the two-photon gain seen is pure Raman gain (and not a result of four-wave mixing), I have not yet explicitly verified this assertion. As the group progresses toward a two-photon laser and places a cavity around our cell, two methods will allow us to distinguish Raman gain from parametric gain. Recall that the two-photon laser exhibits novel threshold behavior in which the threshold depends on both the population inversion and the photon number in the cavity. It displays a discontinuous first-order phase transition at threshold, and this behavior has been both predicted and experimentally verified. A parametric oscillator, however, even one based on high order processes, has threshold behavior basically iden-

 $<sup>^{12}</sup>$ See, for example, the peak at the three-photon gain frequency (probe-pump detuning of  $^{-154}$  MHz) in Fig. 4.17.

tical to that of a normal laser. The transition to lasing is thus a continuous second-order phase transition. Testing of the observed threshold in our system will indicate the gain process upon which the lasing is based, and hence differentiate between pure Raman gain and parametric gain.

In addition, any amplified light at the anti-Stokes frequency will be emitted at a non-zero angle with respect to both the pump and the probe beams in order to phase-match the output. (Recall that phase-matching is not required for typical Stokes gain, so light due to Stokes gain should be emitted in the same direction as the pump beam.) If the laser cavity is arranged such that the anti-Stokes wave cannot oscillate, perhaps through selective use of apertures in the cavity, this will effectively eliminate all but the Raman oscillation. Any lasing must then be due to a true Raman scattering process and not a parametric process.

## 4.8 Experimental parameters

In order to complete the experimental description, it seems worthwhile to give a careful accounting of the experimental parameters utilized in the realization of 30% two-photon gain. Such a summary serves two purposes. Closely duplicating the successful experimental setup should prove useful in further work for reproducing and then improving on the best gain seen to date. In addition, the next chapter involves a semiclassical theory of a driven three-level atom which models our experiment. Although the theory is not yet well-developed enough for an exact quantitative comparison between theory and experiment, a qualitative comparison still benefits from setting parameters such that they correspond with experimental values.

The most important experimental parameters over which we have significant control, and hence those I describe in what follows, are the beam intensities, crossing angles, probe-pump detuning, and cell temperature. The atomic decay rates, broadening mechanisms, and dipole matrix elements are set by the atom we work with - <sup>39</sup>K. Although any theory requires accurate estimates of these quantities, we have little experimental control over them. For this reason, I defer a discussion of these atom-specific variables to the next chapter.

### 4.8.1 The pump detuning

An initial estimate for the pump detuning from resonance of  $\sim 1-2$  GHz comes directly from examining the experimental spectra and estimating the frequency spacing between the line-center probe absorption dip and the pump frequency as taken from the Rayleigh scattering feature. However, I work in a regime where the transition is highly saturated and the wings of the absorption dip are separated by over 2 GHz. In addition, the diode laser in its current configuration has a finite frequency scan of only  $\sim 2$  GHz before mode hopping. It thus proves impossible to view both the scattering resonances and the entire absorption dip using a single diode laser frequency scan. This leads to a rather large uncertainty in the initial detuning estimate. I refine the estimate using computer code written for the theory described in Chapter 5 in order to match the shape and position of the measured weak-field absorption dip to the dip that is calculated at various pump detunings. Theoretical results must account for both Doppler broadening and weak-field propagation effects. My final estimate of the pump detuning is -1440 MHz.

### 4.8.2 Temperature

The cell temperature is carefully monitored and maintained within the heat pipe. Radiative heat loss is minimized using fiberglass insulation, and air currents that might cause convective heat loss or heat fluctuations are also minimized. Thermocouples are attached directly to the cell in order to get an accurate temperature measurement, and we maintain the cell temperature at 150°C.

### 4.8.3 Crossing Angle

The experimental crossing angle at which the best two-photon gain is observed is known from the measured separation between the pump and probe beams at some distance from their crossing point. The centers of the pump and probe beams were 1.2 cm apart a distance 1 m from the cell, giving a crossing angle of 12 mrad. I experimented with both smaller and larger crossing angles, covering the range between about 4 and 20 mrad. Four-wave mixing effects show distinctive destructive effects on the two-photon gain for angles smaller than about 6 mrad. At larger crossing angles the pump-probe interactions decrease simply because the pump-probe overlap significantly decreases. As stated earlier, the best balance of experimental parameters occurred at the crossing angle of 12 mrad.

#### 4.8.4 Beam Intensities

The power P incident on the cell in our pump beam is measured to be 920 mW, and the unattenuated probe power entering the cell is 6.9 mW. From these powers I want to calculate the predicted beam intensities, and easy task

once the beam spot sizes are known. I use a 10  $\mu$ m pinhole mounted on an xyz translation stage to map out the spatial profile of the focused beams at the beam waists  $w_o$ , which are centered in the cell during an experimental run. Fitting the beam profile to a Gaussian determines the spot size at the beam waist as the distance from the beam center such that the beam intensity decreases to 1/e its maximum value. We find  $w_o^{pump} = 64 \ \mu \text{m}$  and  $w_o^{probe} = 28 \ \mu \text{m}$ , and calculate the pump and (unattenuated) probe beam intensities using  $I = P/\pi w_o^2$  to be 7.0 kW/cm<sup>2</sup> and 285 W/cm<sup>2</sup>, respectively. (For readers more familiar with beam sizes quoted in terms of the intensity full width at half maximum, the pump beam intensity FWHM is about 150  $\mu$ m, while the probe beam intensity FWHM is about 65  $\mu$ m.) These predicted beam intensities, however, could be as much as a factor of 2, 4, or more too large due to self-defocusing effects occurring in the cell with unpredictable effects.

## Chapter 5

## Semiclassical Theory of a Driven Three-Level Atom

A very basic understanding of two-photon Raman scattering, such as that described in the last chapter, is all that is needed to realize its potential as a two-photon gain mechanism. I took this understanding into the lab and performed an experiment which demonstrated two-photon gain more than two orders of magnitude higher than the best previous results. Now I would like to theoretically delve a bit deeper into Raman scattering and the other interactions taking place in our experimental gain medium. A theory should help us to identify the important effects taking place in the cell and comprehend the relationships between the numerous experimental parameters. In addition, we hope it should provide us with at least minimal predictive capabilities.

## 5.1 Introduction

It is well known that the interaction of a strong electromagnetic wave with an atomic medium can affect the populations of the atomic states as well as modify the atomic eigenstates, leading to level shifting [45] and splitting [46]. When two waves couple with the atomic system, nonlinear effects such as Raman and multi-photon processes may occur. Absorption, saturation, and optical pumping also affect the light-matter interaction. An accurate theory of a driven atomic medium needs to account for all of these phenomena, which is not necessarily an easy task. In addition the energy level structure of an atomic electron can involve numerous levels, further complicating any complete theory.

There are a few general theoretical approaches for dealing with the interaction between light and matter, especially when dealing with laser behavior. One of the simplest approaches uses rate equations, such as those that will be described in Chapter 7. Rate equations are simple and intuitive, which is why we use them to gain an understanding of the steady-state behavior and stability properties of a two-photon laser. However, they are incomplete in that they do not deal with atomic coherences, which can play a critical role in the eventual laser behavior. In addition, they do not consider propagation effects such as the spatial evolution of the light-field intensity within the nonlinear gain medium. A second approach to light-matter interactions uses Schrödinger amplitudes of motion, derived from Schrödinger's equation and the wave equation, to describe laser dynamics. However, a formalism based upon the atomic wave function has no good way of incorporating atomic decay or collisional (dephasing) effects, limiting the usefulness of such an approach. Perturbation theory, a third common theoretical approach, is not adequate when dealing with more than one strong field.

This chapter presents a semiclassical theory of a driven three-level atom based on density matrix equations of motion. The semiclassical density-matrix equations of motion explicitly consider atomic level populations and the evolution of the atomic dipoles, and effectively account for all of the nonlinear phenomena described above. In addition, this formalism is capable of treating collisional and other broadening effects, and can be applied to both strong and weak electromagnetic fields. Knowledge of the density matrix elements allows one to derive the physical parameters describing the behavior of an atomic system in an optical field, and is useful for predicting experimental observations. Most importantly for our purposes, it is possible to express the atomic absorptive response in terms of the amplitude of the off-diagonal density matrix elements. We intend to use this theory to qualitatively, and perhaps quantitatively, describe our experimental results of the probe gain spectra after passing through a driven atomic vapor.

#### 5.1.1 Comparison of our model with previous theories

The density matrix formalism has long been used to describe the theory of interaction of a single field in a system of two- or three-level atoms [47]. Within the past decade, the interaction of two strong fields in a system of two-level atoms was considered [41], and there have been a number of studies considering two strong fields in a system of three-level atoms. However, previous studies generally only allowed one laser field to interact on any given transition, as indicated in Fig. 5.1a, failing to consider that each laser beam may be coupled to both transitions with non-zero dipole matrix elements. Many higher-order effects, including two-photon Raman gain, can only be explained by considering this more general coupling interaction. This became explicitly evident in a 1991 study [48] examining a three-level, two-beam system that only allowed the beams to interact on a single transition. It predicted only

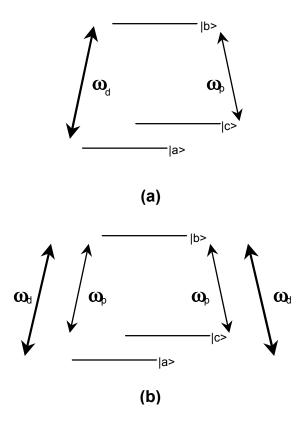


Figure 5.1: Representation of a three-level atom interacting with two incident fields. (a) The field at frequency  $\omega_d$  interacts only on the  $a \leftrightarrow b$  transition, while the field at frequency  $\omega_p$  interacts only on the  $c \leftrightarrow b$  transition. (b) Both fields interact on both atomic transitions.

the *odd* subharmonic Raman resonances (one-photon, three-photon, etc.), and hence could not explain the two-photon resonances we wish to study.

I consider the interaction of two strong fields with a three-level atom and allow both input beams to be strong and nearly resonant with all electronic transitions, as indicated in Fig. 5.1b. This adds a fair amount of complexity to the system, and is one way in which this system differs from most previous three-level, two-beam systems. To my knowledge, only one previous group [49] considered a two-beam, three-level system where each input beam can be strong

and resonant with numerous transitions simultaneously. They worked with pulsed lasers, and hence were interested only in the short-time atomic response. This allowed a direct numerical integration of the density-matrix equations of motion over the time scale of interest. In our system using continuous-wave lasers, I study the long-term and average atomic response, making a direct numerical integration prohibitively time-consuming.

In a two-beam pump-probe saturation spectroscopy experiment such as the one I performed, one typically determines how the response of the medium to the probe wave is altered by the presence of the pump wave. The character of the nonlinear processes is profoundly modified when the intensity of the pump laser is increased to the extent that perturbation theory is not sufficient to describe the interaction. At this point, effects associated with the breakdown of perturbation theory, such as spectral line broadening and Stark shifting, can be quite pronounced and significantly alter the dynamics of the system. The majority of previous theories are valid only in the perturbation theory limit. Even approaches which take perturbation theory out to extremely high order [50] run into difficulties when dealing with large laser intensities. I work at high enough intensities that the theory is forced to go beyond the perturbation theory limit and account for these new effects.

A final difference between this model and many previous models is the common assumption of negligible population transfer between the atomic levels. This simplification would lead to significant errors in the theoretical predictions, as our fields are strong enough to populate the excited state even when far detuned from resonance. Not only must I account for changes to the excited state populations, but population transfer via optical pumping between

the two lower levels also plays a vital role in our experimental system and must be included in the theory.

#### 5.1.2 Usefulness of the theory

Before exploring the details of my theoretical approach to the pump-probe interactions in the potassium cell, I will jump ahead and state that the theory successfully reproduces the important features in our experimental spectra. This is quite exciting, and validates the theoretical approach. I should note, however, that the theory is limited. It does not include the polarization properties of the laser beams or the full magnetic hyperfine structure in the ground and excited states. In addition, the theory fails to account for any spatial variations in the pump or probe beams, or propagation effects as the beams pass through the atomic medium.

Despite these potential difficulties, it seems reasonable to hope that the theory can predict the expected spectral shape and approximate gain due to various scattering processes given the proper experimental parameters. This would allow optimal laser Rabi frequencies and detunings to be numerically determined. Taking things a step further, perhaps the effectiveness of other alkali metals, such as lithium, sodium, or rubidium, in generating high two-photon gain could be theoretically tested. These elements all have unique ground-state splittings, decay rates, and matrix elements, and an alkali other than potassium could prove far superior for our purposes. Yet it is significantly faster, cheaper, and easier to examine the properties of new elements using computer code than by building or buying new lasers to probe their resonances.

# 5.2 Application of the density matrix to spectroscopy experiments

A review of the origin of the density matrix equations was previously given in Sec. 2.1.1. The rest of this chapter formulates a description of the interaction of optical fields with a nonlinear medium through use of the density matrix equations of motion. Why might this be useful? The density matrix equations generally describe a single-atom treatment of quantum optical interactions. In the most complete approach to the problem, from a solution of the density matrix we calculate the single-atom susceptibility of the medium, and hence the microscopic atomic polarization. When applied to a specific atomic system (with a specific number density, for example), this yields knowledge of the total atomic polarization. The polarization then acts as a source term in the macroscopic wave equation and Maxwell's equations, from which we can calculate the propagation effects of the incident field (or fields) through the medium<sup>1</sup>. A self-consistent calculation of this sort yields a complete, time-dependent description of the light-matter interactions taking place in our system.

Although an eventual goal of the theory includes incorporation of these propagation effects, such a calculation is beyond the scope of this thesis. This theory looks at a simpler problem in which I extract the single-atom absorptive response of the medium (calculated at its input face) from the density matrix solutions for the coherences. A plot of the absorptive response as a function of the probe-pump detuning should then correctly identify the frequencies at which to expect a nontrivial spectral response of the medium.

<sup>&</sup>lt;sup>1</sup>Propagation effects account for attenuation (or amplification) of the incident fields as they pass through the medium. They also consider the creation of new fields which can then interact in the medium, for example.

Because I experimentally measure spectral responses (as described in Chapter 4), this calculation proves directly relevant to a comparison between theory and experiment.

The absorptive response of the atomic system at the probe beam frequency  $\omega_{ba}$  is given by [51]

$$\alpha_{ba} = \frac{2\operatorname{Im}(\sigma_{ba})}{\Omega_{ba}/\Gamma_{ba}} \,, \tag{5.1}$$

while the response at the probe beam frequency  $\omega_{bc}$  is given by

$$\alpha_{bc} = \frac{2 \operatorname{Im}(\sigma_{bc})}{\Omega_{bc}/\Gamma_{bc}} \ . \tag{5.2}$$

In Eqs. 5.1 and 5.2,  $\sigma_{ij}$  represents the slowly varying coherence related to the density matrix coherence  $\rho_{ij}$ . In both cases the response has been made unitless by normalizing with respect to the appropriate Rabi frequency  $\Omega_{ij}$ , which has in turn been normalized to the atomic dephasing rate  $\Gamma_{ij}$  of the transition. The total absorptive response for our three-level atomic system is given by the sum of  $\alpha_{ba}$  and  $\alpha_{bc}$ .

Due to limitations in the theory, most notably ignoring the many magnetic sublevels in the atom and ignoring the propagation effects mentioned above, the calculated atomic response cannot be exactly compared with the experimentally measured transmission of the probe beam after passing through the atomic cell. It can, however, give an accurate qualitative picture of the interactions taking place in the system. The calculated spectral frequencies at which interaction features appear, for example, should be accurately known, though the exact peak heights and widths cannot be reliably determined. A direct comparison between theory and experiment does requires Doppler averaging the absorptive response over the atomic velocities in the medium. This

is further explored in Sec. 5.4.3.

To summarize, given the density matrix equations of motion our task is to numerically evaluate the density matrix coherences, and from them evaluate the Doppler averaged absorptive response of the probe beam as a function of the probe-pump detuning. I then compare the results with experimental data by plotting the theoretical probe absorption coefficient as a function of the detuning. As described in the remainder of this chapter, I find the calculated probe transmission spectra from the three-level theory to be qualitatively similar to the experimentally observed spectra. An eventual goal is to use the theory for predicting parameter values which should optimize the spectral features of interest, such as two-photon gain.

## 5.3 Three-level atom equations of motions

I begin a study of the density matrix equations of motion for a three-level atom interacting with two strong fields by starting with the equations of motion for a *single* strong field interacting with both atomic levels, as previously shown in Fig. 5.1a. I start here for two reasons. First, it is possible to solve this problem analytically, so it acts as a first step toward solving the more complicated problem which involves two fields. Additionally, the treatment of a single field interacting with both levels of a three-level atom models the optical pumping process occurring in our system, from which we can watch the expected change in atomic level populations due to this pumping.

I treat the driving field as a monochromatic plane wave

$$\mathbf{E}_d(\mathbf{r},t) = \mathcal{E}_d(\mathbf{r},t)e^{-i\omega_d t} + c.c. , \qquad (5.3)$$

where  $\omega_d$  defines the frequency of the incident driving field. Using the convention that detunings are positive when the fields are tuned to the blue side of resonance, I write the pump field detunings as  $\Delta_{ba} = \omega_d - \omega_{ba}$  and  $\Delta_{bc} = \omega_d - \omega_{bc} = \Delta_{ba} - \Delta_g$ , where  $\Delta_g \equiv \omega_{ca}$  is the ground state splitting. Recall that the only non-zero dipole matrix elements are  $\mu_{ba}$  and  $\mu_{bc}$ . The driving field Rabi frequencies, which measure how effectively the laser stimulates transitions in an atom, are then identified as

$$\Omega_{ba} = \frac{2\mu_{ba} \cdot \mathcal{E}_d(\mathbf{r}, t)}{\hbar} \tag{5.4}$$

and

$$\Omega_{bc} = \frac{2\boldsymbol{\mu}_{bc} \cdot \mathcal{E}_d(\mathbf{r}, t)}{\hbar} \ . \tag{5.5}$$

As I did in Sec. 2.1.1, I define slowly varying coherences (specified by  $\sigma_{ij}$  rather than  $\rho_{ij}$ ) such that

$$\rho_{ba} = \sigma_{ba} e^{-i\omega_d t} \tag{5.6}$$

and

$$\rho_{bc} = \sigma_{bc} e^{-i\omega_d t} \ . \tag{5.7}$$

The coherence  $\rho_{ca}$  already represents a slowly varying quantity, as it oscillates with a frequency close to  $\omega_{ca}$  which is much less that the typical optical frequency. For this reason, I simply rename  $\rho_{ca} = \sigma_{ca}$ . The rotating wave approximation now keeps only resonant terms and effectively factors out terms which oscillate at optical frequencies, significantly simplifying the problem.

With all of these substitutions and definitions for a three-level system, Eqs. 2.7 and 2.8 are used to write the equations for the slowly varying coherences and populations,

$$\frac{\partial \sigma_{ba}}{\partial t} = (i\Delta_{ba} - \Gamma_{ba})\sigma_{ba} + \frac{i}{2}(\Omega_{ba}\sigma_{aa} + \Omega_{bc}\sigma_{ca} - \Omega_{ba}\sigma_{bb}), \qquad (5.8)$$

$$\frac{\partial \sigma_{bc}}{\partial t} = (i\Delta_{bc} - \Gamma_{bc})\sigma_{bc} + \frac{i}{2}(\Omega_{ba}\sigma_{ac} + \Omega_{bc}\sigma_{cc} - \Omega_{bc}\sigma_{bb}), \qquad (5.9)$$

$$\frac{\partial \sigma_{ca}}{\partial t} = (-i\Delta_g - \Gamma_{ca})\sigma_{ca} + \frac{i}{2}(\Omega_{cb}\sigma_{ba} - \Omega_{ba}\sigma_{cb}) , \qquad (5.10)$$

$$\frac{\partial \sigma_{aa}}{\partial t} = (\gamma_{ba}\sigma_{bb} + \gamma_{ca}\sigma_{cc} - \gamma_{ac}\sigma_{aa}) + \frac{i}{2}(\Omega_{ab}\sigma_{ba} - \Omega_{ba}\sigma_{ab}) , \qquad (5.11)$$

$$\frac{\partial \sigma_{cc}}{\partial t} = (\gamma_{bc}\sigma_{bb} - \gamma_{ca}\sigma_{cc} + \gamma_{ac}\sigma_{aa}) + \frac{i}{2}(\Omega_{cb}\sigma_{bc} - \Omega_{bc}\sigma_{cb}) , \qquad (5.12)$$

and

$$\frac{\partial \sigma_{bb}}{\partial t} = -(\gamma_{ba} + \gamma_{bc})\sigma_{bb} + \frac{i}{2}(\Omega_{ba}\sigma_{ab} + \Omega_{bc}\sigma_{cb} - \Omega_{ab}\sigma_{ba} - \Omega_{cb}\sigma_{bc}) .$$
 (5.13)

Conservation of population within the system,

$$\sigma_{aa} + \sigma_{bb} + \sigma_{cc} = 1 , \qquad (5.14)$$

can be used to eliminate the  $\sigma_{bb}$  equation. Equations for the coherences  $\partial \sigma_{ab}/\partial t$ ,  $\partial \sigma_{cb}/\partial t$ , and  $\partial \sigma_{ac}/\partial t$  are found as the complex conjugates of the first three equations. The above equations serve as a basis from which to study both the shifting of energy levels due to a strong pump field and explore the populations of the atomic levels as a function of the pump intensity.

## 5.3.1 Optical Stark Effect

When the wavelength of a laser is scanned across an atomic transition, the phase and amplitude of the transmitted light change because both the refractive index and the absorption coefficient of the atom are functions of frequency. If the laser is resonant or near resonant with the transition, two other effects come into play – the AC Stark effect and Rabi oscillations. Application of a

strong field to a gas of three-level atoms cause the ground state populations to move about, resulting in an oscillation of the population inversion between the ground and excited states at a characteristic frequency equal to the Rabi frequency; these population oscillations are called Rabi oscillations. A strong laser field also modifies the energy-level structure of the atom, splitting and shifting energy levels and resulting in qualitatively new atomic resonances. The splitting is analogous to the familiar DC Stark effect in which atomic energy levels are shifted by a constant electric field. In the AC Stark effect, sometimes known as the Autler-Townes splitting [46], the energy levels are split by the oscillating electric field of the laser beam.

In a three-level atom each energy level will be split into a triplet of levels. This is most easily understood in the dressed-atom basis, but I do not intend to delve into any details concerning dressed states here, both because they have been extensively discussed in a number papers and textbooks [52] and because a complete discussion goes beyond the realm of this thesis. Rather than calculating the level splittings in the dressed-state basis, we remain in the bare-atom basis and use the density matrix equations of motion to describe this system. Level splittings create qualitatively new resonances in a probe absorption or fluorescence spectrum due to the new resonant frequencies they introduce. To monitor these changes, I allow a single strong laser to interact between both optical transitions in the system while a weaker probe laser couples a single system level to a fourth level outside of the system. When the strong laser is switched on, the system level coupled by the probe laser will be split into three sub-levels, causing the familiar absorption curve (like that of Fig. 4.2) to now display three separate dips.

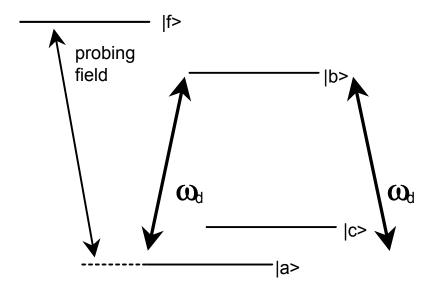


Figure 5.2: Use of a probe field to study level-shifting effects due to a strong driving field (frequency  $\omega_d$ )

More explicitly, in order to examine the splitting and shifting of level a, for example<sup>2</sup>, I consider a three-level atom pumped by a strong field on both the  $b \to a$  and  $b \to c$  transitions. A weak probe between state a and another state in the system f examines how the level a shifts relative to f, as shown in Fig. 5.2. The weak probe should examine the system without affecting either the population distribution or the level shifts caused by the strong driving field. I also assume that the weak field will not significantly populate level f, so  $\rho_{ff} \approx 0$ . Since the populations in our system remain unchanged (they are described by Eqs. 5.11 – 5.14), the only new system dynamics involve the coherences to the new state:  $\rho_{fa}$ ,  $\rho_{fb}$ , and  $\rho_{fc}$ .

Applying the general density matrix equation of motion, Eq. 2.8, to a

<sup>&</sup>lt;sup>2</sup>An exactly analogous process with probing fields between levels  $b \leftrightarrow f$  or  $c \leftrightarrow f$  are used to look at the shifts in these levels. For brevity's sake, I only describe the mathematics for level a.

system with a weak probe between level f and level a gives

$$\frac{\partial \rho_{fa}}{\partial t} = (-i\omega_{fa} - \Gamma_{fa})\rho_{fa} + \frac{i}{\hbar}(\boldsymbol{\mu}_{fa}\rho_{aa} - \boldsymbol{\mu}_{ba}\rho_{fb}) \cdot \mathbf{E}(\mathbf{r}, t) , \qquad (5.15)$$

$$\frac{\partial \rho_{fb}}{\partial t} = (-i\omega_{fb} - \Gamma_{fb})\rho_{fb} + \frac{i}{\hbar}(\boldsymbol{\mu}_{fa}\rho_{ab} - \boldsymbol{\mu}_{ab}\rho_{fa} - \boldsymbol{\mu}_{cb}\rho_{fc}) \cdot \mathbf{E}(\mathbf{r}, t), (5.16)$$

and

$$\frac{\partial \rho_{fc}}{\partial t} = (-i\omega_{fc} - \Gamma_{fc})\rho_{fc} + \frac{i}{\hbar}(\boldsymbol{\mu}_{fa}\rho_{ac} - \boldsymbol{\mu}_{bc}\rho_{fb}) \cdot \mathbf{E}(\mathbf{r}, t) . \tag{5.17}$$

I write these coherences in terms of slowly varying quantities by applying the usual rotating wave approximation transformations in which I factor out the optical frequency time dependences (as described by Eqs. 5.6 and 5.7), with the addition of the equations

$$\rho_{fa} = \sigma_{fa} e^{-i\omega_f t} \quad , \quad \rho_{fc} = \sigma_{fc} e^{-i\omega_f t} \quad , \tag{5.18}$$

and

$$\rho_{fb} = \sigma_{fb} e^{-i(\omega_f - \omega_d)t} \ . \tag{5.19}$$

I then define the detuning  $\Delta_{fa} = \omega_f - \omega_{fa}$  and arrive at the equations

$$\frac{\partial \sigma_{fa}}{\partial t} = (i\Delta_{fa} - \Gamma_{fa})\sigma_{fa} + \frac{i}{2}(\Omega_{fa}\sigma_{aa} - \Omega_{ba}\sigma_{fb}) , \qquad (5.20)$$

$$\frac{\partial \sigma_{fb}}{\partial t} = [i(\Delta_{fa} - \Delta_{ba}) - \Gamma_{ba}]\sigma_{fb} + \frac{i}{2}(\Omega_{fa}\sigma_{ab} - \Omega_{ab}\sigma_{fa} - \Omega_{cb}\sigma_{fc}), (5.21)$$

and

$$\frac{\partial \sigma_{fc}}{\partial t} = \left[ i(\Delta_{fa} + \Delta_g) - \Gamma_{ca} \right] \sigma_{fc} + \frac{i}{2} (\Omega_{fa} \sigma_{ac} - \Omega_{bc} \sigma_{fb}) . \tag{5.22}$$

In steady-state this system reduces to a set of simultaneous algebraic equations from which I easily solve for the coherence of interest, in this case  $\sigma_{fa}$ since we are probing the  $f \to a$  transition. For notational compactness we define the quantities

$$D_1 = 2\left[ (\Delta_{fa} + \Delta_g) + i\Gamma_{ca} \right] , \qquad (5.23)$$

$$D_2 = 2 [(\Delta_{fa} - \Delta_{ba}) + i\Gamma_{ba}],$$
 (5.24)

and

$$D_3 = (\Delta_{fa} + i\Gamma_{fa}) . (5.25)$$

With a little bit of algebra (which of course is left to the careful reader) the  $\sigma_{fa}$  coherence can then be written

$$\sigma_{fa} = \left(\frac{D_{1}D_{2} - |\Omega_{bc}|^{2}}{D_{3}(D_{1}D_{2} - |\Omega_{bc}|^{2}) - D_{1} |\Omega_{ba}|^{2}}\right) \times \left[\sigma_{aa} + \frac{D_{1}\Omega_{ba}}{D_{1}D_{2} - |\Omega_{ba}|^{2}} \left(\sigma_{ab} + \frac{\Omega_{cb}}{D_{1}}\sigma_{ac}\right)\right].$$
(5.26)

As described in Sec. 5.2 the absorptive response of the probe beam,  $\alpha_{fa}$ , is then

$$\alpha_{fa} = 2 \operatorname{Im} \left( \frac{\sigma_{fa}}{\Omega_{fa}/\Gamma_{fa}} \right) . \tag{5.27}$$

Because features in the absorption spectrum result from transitions between atomic states, level splittings and shiftings which can qualitatively change both the number and positioning of atomic levels then also change the absorption spectrum. In order to examine level-splitting effects I use a simple peak-finding routine to extract the features (peaks and dips) in the spectrum described by the absorptive response. Tracking the frequencies at which these features appear as a function of the pump Rabi frequency then maps out the atomic level structure.

I mapped the level shifts for all three states in the system, as shown in Fig. 5.3. In the calculations, I set the potassium ground-state splitting to  $\Delta_g =$  460 MHz and the detuning of the pumping beam from the  $b \leftrightarrow a$  resonance

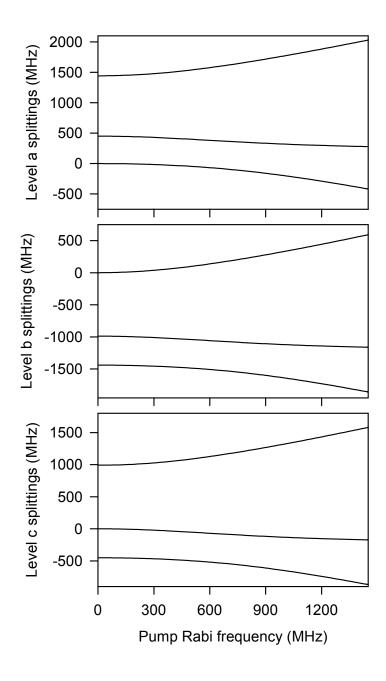


Figure 5.3: Splitting and shifting of atomic energy levels due to interaction with a strong electromagnetic field

to  $\Delta_{ba} = -1440$  MHz. Other parameters (listed in the figure caption) well describe the experimental system.

The splittings are shown as a function of the strength of the pump beam Rabi frequency. As expected, each level becomes a triplet of levels, and the frequency splittings at zero Rabi frequency are directly related to the detuning and ground state splittings. The levels that begin at a zero frequency splitting are the natural levels of the system (i.e., those that exist in the atom when it is not interacting with a light field). Note that the splittings for each level are quite similar – the only real difference is in where the new levels are created relative to the natural atomic levels. As the pumping Rabi frequency increases, the splittings increase and the levels tend to repel each other, leading to spectral resonances at larger detunings. The most important new resonances caused by the level splittings in terms of the observed spectral features are the Rabi resonances. As described in Chapter 4, these resonances correspond to simultaneous absorption of two pump laser photons and emission of a probe laser photon in making a transition to the excited state.

Of special interest to us is the change in the splitting between the Raman transition levels c and a. The spectral position of all Raman features is critically dependent on this splitting, which in a bare potassium atom is equal to the hyperfine splitting  $\Delta_g$ . Although both the c and a levels are affected by the dynamic Stark shift (as is clearly shown in Fig. 5.3), Fig. 5.4 illustrates that their difference stays relatively constant until the Rabi frequencies exceed about 860 MHz. Experimentally, I believe the largest pump Rabi frequencies to be  $\sim 750$  MHz which, though large, should *not* cause significant spectral changes of the Raman peaks due to level shifts. This is an important conclusion which

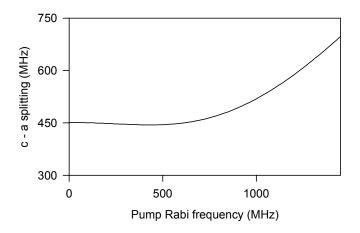


Figure 5.4: Change in the splitting between levels c and a as a function of pump Rabi frequency. Parameter values model the potassium atom, where the ground-state splitting is taken to be 450 MHz. The pump detuning is taken to be -1440 MHz.

affects both the theoretical and experimental frequency calibrations.

In addition to exploring the Stark shifted levels, I also solved Eqs. 5.11 – 5.14 for the level populations as a function of the pump Rabi frequency. This allows a determination of the frequency at which significant population redistribution begins to take place in the system. As shown in Fig. 5.8, there is a population inversion between levels a and c at low Rabi frequencies. This is exactly what we want and need in order to see gain on the one-photon and two-photon  $a \to c$  Raman transitions. It is interesting to note, however, that at pump Rabi frequencies above about 830 MHz, population redistribution reverses the inversion: now level c is more populated than level a. This redistribution becomes noticeable when the pump Rabi frequency is more than

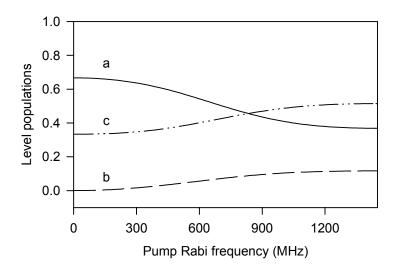


Figure 5.5: Level populations as a function of pump Rabi frequency

about twice the atomic ground-state splitting. At these high frequencies, the pump field interacts with both levels in a fairly equal manner, as the splitting no longer seems significant. This causes the optical pumping cycle to break down because the level populations are now set more by the decay branching ratio of the excited state (which tends to populate level c) than the pump field absorption rate (which previously depopulated level c).

## 5.4 Modifications for a second field

To the system involving a single electromagnetic field describe in Sec. 5.3, I now want to add a second (probe) field,

$$\mathbf{E}_{p}(\mathbf{r},t) = \mathcal{E}_{p}(\mathbf{r},t)e^{-i\omega_{p}t} + c.c. . \qquad (5.28)$$

This situation was modelled in Fig. 5.1b. With the addition of the probe field at a frequency  $\omega_p$ , the theoretical system now mimics our two-beam probepump spectroscopy experiment.

How will the addition of a second field affect our equations? It turns out that the driving field and the probe field beat with each other and lead to harmonic modulations of the atomic populations and coherences. This can be modelled by performing the substitutions

$$\Omega_{ba} \to (\Omega_{ba})_d + (\Omega_{ba})_p e^{-i\Delta_p t}$$
 (5.29)

and

$$\Omega_{bc} \to (\Omega_{bc})_d + (\Omega_{bc})_p e^{-i\Delta_p t} ,$$
 (5.30)

in Eqs. 5.8 – 5.13, where I have introduced the probe-pump detuning  $\Delta_p = \omega_p - \omega_d$  and I explicitly identify the pump and probe Rabi frequencies for each transition.

With the addition of the second field, an exact solution for the populations and coherences cannot easily be found. The nonlinear response of the atomic medium to the applied fields introduces all possible harmonics of the pump/probe beat frequency. If the probe field is weak, and hence has only a weakly nonlinear response, only the first few harmonics are important and perturbation theory well describes the interaction. If, however, both beams are taken strong enough to saturate the optical transitions (as they are in our experiment), in theory all of the harmonics become important to accurately model the interaction. To deal with these difficulties, I decompose the populations and coherences into a Fourier sum with the ansatz

$$\sigma_{ij} = \sum_{n} (\sigma_{ij})_n e^{-in\Delta_p t} \tag{5.31}$$

for i>j (i.e., i is a higher atomic energy level than j) and

$$\sigma_{ij} = \sum_{n} (\sigma_{ij})_n e^{+in\Delta_p t} \tag{5.32}$$

for i < j. My strategy involves finding a solution correct to all orders in the pump field and any chosen order in the probe field, then only requiring the retention of a finite number of terms in this sum.

Assuming constant coefficients  $(\sigma_{ij})_n$  since I am interested in the steadystate response, I rewrite the system of equations (given by Eqs. 5.8 – 5.14) in terms of the Fourier sums. Equating Fourier coefficients then yields recursion relations for the coherences,

$$[\Gamma_{ba} - i(\Delta_{ba} + n\Delta_{p})](\sigma_{ba})_{n} = \frac{i}{2}[(\Omega_{ba})_{d}(\sigma_{aa})_{n} + (\Omega_{ba})_{p}(\sigma_{aa})_{n-1}$$

$$+ (\Omega_{bc})_{d}(\sigma_{ca})_{n} + (\Omega_{bc})_{p}(\sigma_{ca})_{n-1}$$

$$- (\Omega_{ba})_{d}(\sigma_{bb})_{n} - (\Omega_{ba})_{p}(\sigma_{bb})_{n-1}],$$

$$[\Gamma_{bc} - i(\Delta_{bc} + n\Delta_{p})](\sigma_{bc})_{n} = \frac{i}{2}[(\Omega_{ba})_{d}(\sigma_{ac})_{-n} + (\Omega_{ba})_{p}(\sigma_{ac})_{-n+1}$$

$$+ (\Omega_{bc})_{d}(\sigma_{cc})_{n} + (\Omega_{bc})_{p}(\sigma_{cc})_{n-1}$$

$$- (\Omega_{bc})_{d}(\sigma_{bb})_{n} - (\Omega_{bc})_{p}(\sigma_{bb})_{n-1}],$$

$$[i(\Delta_{g} - n\Delta_{p})](\sigma_{ca})_{n} = \frac{i}{2}[(\Omega_{cb})_{d}(\sigma_{ba})_{n} + (\Omega_{cb})_{p}(\sigma_{ba})_{n+1}$$

$$- (\Omega_{ba})_{d}(\sigma_{cb})_{-n} - (\Omega_{ba})_{p}(\sigma_{cb})_{-n+1}],$$

$$- in\Delta_{p}(\sigma_{aa})_{n} = \frac{i}{2}[(\Omega_{ab})_{d}(\sigma_{ba})_{n} + (\Omega_{ab})_{p}(\sigma_{ba})_{n+1}$$

$$- (\Omega_{ba})_{d}(\sigma_{ab})_{-n} - (\Omega_{ba})_{p}(\sigma_{ab})_{-n+1}]$$

$$+ \gamma_{ba}(\sigma_{bb})_{n},$$

$$(5.37)$$

and

$$-in\Delta_p(\sigma_{cc})_n = \gamma_{bc}(\sigma_{bb})_n + \frac{i}{2}[(\Omega_{cb})_d(\sigma_{bc})_n + (\Omega_{cb})_p(\sigma_{bc})_{n+1}$$
 (5.38)

$$-(\Omega_{bc})_d(\sigma_{cb})_{-n}-(\Omega_{bc})_p(\sigma_{cb})_{-n+1}].$$

The conservation of population equation becomes

$$(\sigma_{aa})_{n=0} + (\sigma_{bb})_{n=0} + (\sigma_{cc})_{n=0} = 1.$$
 (5.39)

The conjugate coherence equations can be found from Eqs. 5.33 - 5.35 by making the substitutions

$$i \rightarrow -i$$
, (5.40)

$$\Omega_{lm} \rightarrow \Omega_{ml} , \qquad (5.41)$$

$$(\sigma_{lm})_n \rightarrow (\sigma_{ml})_n , \qquad (5.42)$$

and

$$(\sigma_{ll})_n^* \to (\sigma_{ll})_{-n} . \tag{5.43}$$

The last equation follows because the populations are real.

### 5.4.1 Computational issues

In order to find the populations and coherences for this three-level atomic system interacting on *both* relevant transitions with *two* electromagnetic fields, I numerically solve the system of equations for the time-dependent diagonal and off-diagonal density matrix elements. Although the system is technically in the form of an infinite matrix, and hence of infinite order, generally fewer than the first 15 terms are needed to accurately describe the behavior.

If I look at the system of equations in terms of its Fourier components, each order effect needs to be calculated from the component of the induced polarization at the proper frequency. Note from Eqs. 5.31 and 5.32 that if only the n = 0 term in the sum is kept, this corresponds to an exact solution

for the driving field with no applied probe field as described by Eqs. 5.8 – 5.14. Introducing the  $n = \pm 1$  terms represents the probe field acting to lowest order, with a frequency response at the pump-probe detuning  $\Delta_p$ . The n=0and  $n = \pm 1$  terms dominate for a strong pump and weak probe beam; this represents the perturbation theory limit. Higher order pump-probe effects correspond to higher terms in the sum, which generally become important as the probe beam intensity is increased. In order to predict second order effects like two-photon gain I must include at least one additional term in both the pump and the probe fields, though saturation of the two-photon gain requires many  $(\geq 5)$  higher-order terms. Third (and higher) order effects require the inclusion of even more terms in each field. At a bare minimum, I keep terms to at least one order higher than the effect we are interested in studying, so, for example, I will calculate to at least third order when looking a two-photon gain. A check for consistency and convergence involves insuring that the numerical results do not change significantly with the addition of more terms. Most of the calculations retained 7 terms.

The size of the matrix system I need to solve scales as the square of the number of terms kept in the calculation. The solitary n=0 term creates a  $9 \times 9$  matrix from the original nine equations and nine unknowns. Including the n=+1 term increases the number of equations to 18, thus yielding an  $18 \times 18$  matrix. Because computations scale as a high power of the dimension of the matrix, solving the matrix system can quickly become unmanageable in terms of the computation time involved. However, I can exploit some of the symmetry and term relationships of the problem in order to decrease the number of calculations that need to be completed. A direct inspection of

the equations shows that any given Fourier coefficient  $(\sigma_{lm})_n$  is written only in terms of other coefficients with Fourier index  $\pm n$  and  $\pm n \pm 1$ . When the recursion relations are written in matrix form, the matrix is sparsely populated and nearly block diagonal. As more terms in the sum are retained and the matrix grows in size, exploiting the sparsity of the total matrix becomes even more important.

With this in mind, it proves most efficient to use a sparse-matrix solving package which implements standard mathematical techniques to quickly reduce and solve our matrix equations. I use Sparse 1.3: A Sparse Linear Equation Solver [53] that uses routines capable of solving large systems of linear equations, handling both real and complex matrices, performing matrix initialization, exploiting sparsity to reduce unnecessary computation, and performing all arithmetic operations and numerical storage using double precision for more accurate results.

I wrote a C++ program (with the help of William J. Brown) which defines the experimental parameters and sets up the matrix system for the given number of terms we wish to include in the calculations. Once the system has been created, it calls Sparse 1.3 to initialize the matrix, solve for the coherences, and calculate the absorptive response. In order to properly mimic the experimental data, the program is designed to calculate the theoretical spectra as a function of the detuning frequency, where the pump frequency is fixed while the probe frequency scans across the hyperfine resonances. Though Sparse 1.3 is one of the fastest packages on the market, the routine requires about 0.1 seconds of computing time (on a PC with a 90 MHz Pentium processor) to solve the matrix equations at each value of the probe-pump detuning when terms out to

#### 5.4.2 General spectral features

What sort of spectra do the calculations and computations predict? A representative output spectrum is shown in Fig. 5.6, where part (a) includes the entire range of probe-pump detunings explored experimentally, and part (b) focuses on a smaller range in order to more easily label a few features for identification purposes. The parameter values used to calculate this spectrum are shown in the figure caption and are further discussed in Sec.5.5.

Although the origin of the labelled features has already been discussed in Chapter 4, I briefly recap here the multiphoton processes resulting in these resonances. The dispersive peak at the pump frequency (peak a) is due to Rayleigh scattering. Rayleigh scattering involves a pump photon and a probe photon of approximately the same frequency and returns the atom to its initial state. Peak b, centered at the  $\Delta_g = 450$  MHz frequency equal to the  $c \rightarrow a$  splitting input into the program, is due to saturated one-photon Raman scattering. Two-photon Raman scattering, which occurs at a frequency equal to one-half of the  $c \rightarrow a$  splitting (225 MHz) accounts for peak c. Though not shown here, the theory also reproduces the resonant absorption dip, which is off-scale to the right in Fig. 5.6.

The general appearance of the spectral features looks a bit different from the data presented in the last chapter. In particular, experimentally we used the narrowness of the Raman features with respect to other scattering features as a means of identification. Yet in the theoretical spectra shown there are a number of features narrower than the Raman ones, especially since the one-photon

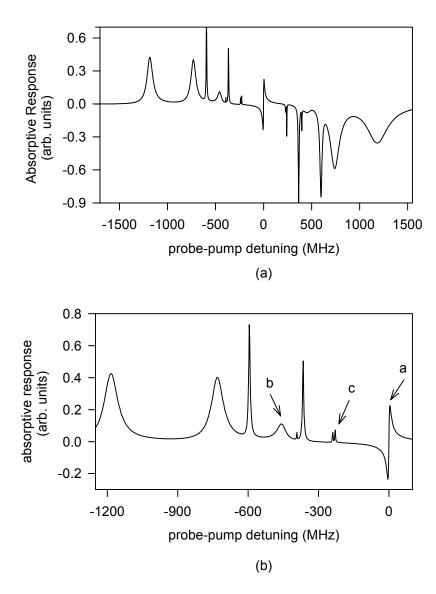


Figure 5.6: Typical output spectrum of our theoretical calculations. The parameter values used in this plot are:  $(\Omega_{ba})_d = (\Omega_{bc})_d = 625$  MHz;  $(\Omega_{ba})_p = (\Omega_{bc})_p = 130$  MHz;  $\Gamma_{ba} = \Gamma_{bc} = 3.2$  MHz;  $\Gamma_{ca} = 1.0$  MHz;  $\gamma_{ba} = 2.1$  MHz;  $\gamma_{bc} = 4.2$  MHz;  $\gamma_{ca} = 1.3$  MHz;  $\gamma_{ac} = 0.32$  MHz;  $\Delta_g = 450$  MHz; and  $\Delta_p = -1440$  MHz.

Raman peak already shows some power-broadening effects. This discrepancy is in fact quite easy to explain. The above calculations have not yet taken Doppler broadening (or any other broadening effects) into account. Until this is done, a first order approximation to the full width at half maximum of all the (unsaturated) features is their natural linewidth, approximately 6 MHz.

In addition to the general narrowness of the features, a large number of peaks in the spectra predicted by the numerical calculation remain unlabeled. These features might, on first glance, seem difficult to explain in terms of a simple three-level atom, especially as I have already identified the obvious physical processes and effects. A number of different effects contribute to the complexity of the spectra and these new resonances, perhaps the most important of which are the splitting and shifting of atomic energy levels in a strong applied field that were described in Sec. 5.3.1. Recall that the strong pump field created level triplets in the three-level atom. Rabi transitions between these new levels appear at a multitude of frequencies, and explain all of the new resonant features in the calculated absorptive response.

Despite the creation of new resonances due to AC Stark shifting, experimentally we do not see a multitude of new features appearing in the probe transmission spectra. Again, this is at least partially due to Doppler broadening effects which have not yet been incorporated into our theory.

## 5.4.3 Doppler Averaging

The results of the previous analysis do not (and should not be expected to!) yield spectra that correspond well with our experimental results. In order to accurately describe our physical system, I also need to perform a Doppler average

over the atomic velocities in the gain medium. Performing a Doppler average consists of integrating the single-atom absorptive response over a distribution of suitably averaged atomic velocities.

I follow the averaging procedure used in Ref. [41]. For simplicity I assume two exactly copropagating beams, which reduces the three-dimensional averaging to the one-dimensional average performed by the integral

$$\alpha^{D}(\omega_{D}, \omega_{p}) = \frac{1}{\sqrt{\pi}} \int_{-\infty}^{+\infty} d\omega_{D} \ \alpha(\Delta_{p} - \omega_{D}/T_{2}^{*}) \exp[-\omega_{D}^{2}] \ , \tag{5.44}$$

where  $\omega_D$  is the Doppler shift experienced by both the pump and probe waves and all quantities have been normalized to the dephasing rate. The quantity

$$T_2^* = \frac{\lambda}{2\pi} (m/k_B T)^{1/2} \tag{5.45}$$

is the effective Doppler dephasing time, and can be orders of magnitude smaller than the dephasing rate for a naturally broadened atom. In potassium,  $T_2 = 50$  ns while  $T_2^* = 0.41$  ns. This leads to a Doppler broadened linewidth of  $\sim 400$  MHz, as compared to the 6 MHz naturally broadened linewidth.

There are two final notes to make about the Doppler averaging. First, our experimental data has a nonzero residual Doppler linewidth which is not included in our theory, because in reality the beams crossed at a finite angle. A future version of the theory will account for this effect. Second, the probepump detuning  $\Delta_p$  in Eq. 5.44 should really be the Doppler averaged detuning. However, as shown in Chapter 4, for counter-propagating beams the Doppler averaged and non-Doppler averaged detunings are identical.

Figure 5.7 illustrates the dramatic effect Doppler averaging has on the theoretical results, where the averaging was performed on the spectra previously shown in Fig. 5.6. The most obvious effect is the broadening and flattening

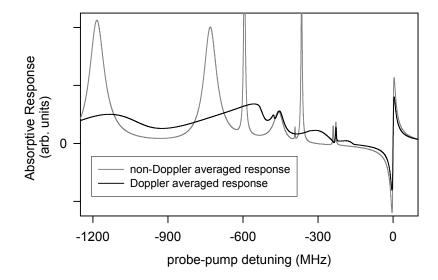


Figure 5.7: Comparison of a Doppler averaged spectrum with one that has not been Doppler averaged. Parameter values are the same as those used in Fig. 5.6.

of the numerous individual Rabi peaks. This smooths the general appearance of the spectrum by making many of the features created by Rabi transition between Stark levels unresolvable. *All* Rabi features are significantly affected by Doppler broadening – not only do they broaden, but their Doppler averaged amplitude is generally only a small fraction of their original amplitude.

The Raman peaks, on the other hand, are only marginally affected by the Doppler averaging. Raman interactions involve pairs of photons in making a transition between atomic states, where the transition takes place only when a resonance condition – the detuning between the incident laser beams is equal to the fixed ground state splitting of the atom – is satisfied. Yet in the special

case where the pump and probe beams are copropagating, this detuning is unaffected by atomic motion, so Doppler averaging plays little role in defining the transition profile. In a similar manner, the Rayleigh scattering feature is relatively unaffected by the effects of atomic motion. At a zero probe-pump frequency detuning, copropagating waves are again Doppler shifted by exactly the same amount, effectively cancelling the Doppler effect. In addition, further analysis shows that the width of the resonance is approximately independent of the atomic velocity [41], so the spectral shape of the Rayleigh scattering feature away from zero detuning remains virtually unchanged. Figure 5.7 clearly illustrates the constancy of the size and shape of the Raman and Rayleigh resonances.

Doppler averaging proves computationally intensive, requiring an average over the atomic velocities at each and every probe-pump detuning in the spectrum. I found it most efficient to change the convolution integral (of the non-averaged spectra with a Gaussian velocity distribution) represented by Eq. 5.44 to an ordinary differential equation,

$$\frac{d\alpha^D(\omega_D, \omega_p)}{d\omega_D} = \frac{1}{\sqrt{\pi}} \alpha(\Delta_D - \omega_D / T_2^*) \exp[-\omega_D^2] . \tag{5.46}$$

I continue to use the sparse matrix solving routine described previously to find the non-averaged absorptive response at each point. Then I use a canned Numerical Recipes fourth-order Runge-Kutta numerical integration routine with variable step size [54] to evaluate the Doppler averaged probe absorption. Computation time for the Doppler averaged spectrum was about 10 seconds at each probe-pump detuning.

## 5.5 Theoretical parameter values

As I have said earlier, the theory is not yet advanced enough to make an exact quantitative comparison between experiment and results. Such a comparison would require computation of the absorption coefficient rather than the absorptive response, which involves both proper normalization of the parameters to the experimental system and a careful accounting of propagation effects. We would also need to include effects resulting from the full level structure of potassium, and account for the Gaussian, rather than constant, beam profiles. Despite these factors it remains both useful and valid to run theoretical calculations in which actual experimental parameters are input in order to model the experimental system. At a minimum, this allows a check to see if the theory produces both the expected features and the expected general trends as the parameter values are adjusted.

In the last chapter, I identified some of the important experimental parameters used to realize high two-photon gain. In addition, the theory requires knowledge of atomic parameters such as the spontaneous emission rates and electric dipole matrix elements. Knowledge of matrix elements in conjunction with laser intensities is used to calculate Rabi frequencies of the incident fields input into the theory. Estimates of these parameters, which I then use to compare our theoretical absorptive response to actual experimental spectra, are described below.

## 5.5.1 Calculation of the electric dipole matrix elements

While studying the  $4P_{1/2} \to 4S_{1/2}$  transition in potassium, incorporation of the  $4S_{1/2}$  ground state hyperfine splitting proves crucial for our results because the

Figure 5.8: Level scheme used in the calculation of dipole matrix elements

Raman transition of interest explicitly involves both these levels in transferring population from one ground state to the other. As a result, I model the atom using three levels, two ground states (labelled a and c) and one excited state (labelled b) as shown in Fig. 5.8. Even this does not completely represent the atom, however, because the coupling of the total electronic angular momentum F with the nuclear angular momentum F leads to a magnetic hyperfine structure which we have ignored up until this point.

A more complete diagram of the relevant potassium levels is shown in Fig. 5.9. Both states have two hyperfine structure F levels, which then in turn have 2F + 1 magnetic sublevels labelled by M. When selection rules permit, there are nonzero electric dipole matrix elements between all of the excited-state hyperfine levels and sublevels and all of the ground-state hyperfine levels and sublevels. These matrix elements can be calculated (in the LS coupling

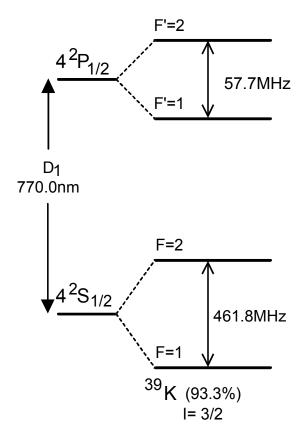


Figure 5.9: Level diagram for potassium

approximation) using the Wigner-Eckart theorem, which states

$$\left\langle (j'I')F'M' \mid \mu_q^{(1)} \mid (jI)FM \right\rangle = (-1)^{F'-M'} \begin{pmatrix} F' & 1 & F \\ -M' & q & M \end{pmatrix} \times \left\langle (j'I')F' \parallel \mu(1) \parallel (jI)F \right\rangle . (5.47)$$

Here primed terms indicate the excited state and the unprimed ones represent the ground state. The dipole matrix element is written as a first-order tensor operator  $\mu_q^{(1)}$ , where q is the polarization of the light used and q=0 represents  $\hat{z}$  polarization.

	F=1	F=2
F'=1	-1/2	$-\sqrt{5}/2$
F'=2	$\sqrt{5}/2$	$-\sqrt{5}/2$

Table 5.1: Values of the reduced matrix element  $\langle F' \parallel \mu(1) \parallel F \rangle$ . Each element in the table should be multiplied by the factor  $\mu_o$ .

I find the reduced matrix element in the above equation as

$$\langle (j'I')F' \parallel \mu(1) \parallel (jI)F \rangle = \delta_{I'I}(-1)^{j'+I+F+1} \sqrt{(2F'+1)(2F+1)} \times \mu_o \left\{ \begin{array}{ccc} j' & I & F' \\ F & 1 & j \end{array} \right\}.$$
 (5.48)

The constant  $\mu_o$  is defined equal to the matrix element  $\langle j' \parallel \mu(1) \parallel j \rangle$ , which is actually independent of j and j'. The Wigner three-j and six-j symbols in the above equations are calculated using *Mathematica*. Using Eqs. 5.47 and 5.48, Table 5.1 summarizes the reduced matrix elements for the  $4P_{1/2} \rightarrow 4S_{1/2}$  transition in potassium. Table 5.2 lists the  $\hat{z}$  component of the electric dipole moment between the states, where the electric field orientation is assumed to be aligned with the z axis of the potassium atoms.

Electric dipole matrix elements are used to calculate a number of important quantities, such as laser beam Rabi frequencies, individual spontaneous emission lifetimes, and the strength of a transition between levels. Before they can be effectively used in this manner, however, a numerical value for the constant  $\mu_o$  must be found in order to explicitly evaluate the matrix elements in terms of some known quantity. This can be done through knowledge of the experimentally observed spontaneous lifetime of 1/(25 ns) for the <sup>39</sup>K excited state.

Using Eq. 4.23 in Ref. [55], the spontaneous emission rate (also called the Einstein A coefficient) can be written in terms of a sum over the possible decay

		F=2	F=2	F=2	F=2	F=2	F=1	F=1	F=1
F'	M'	M=2	M=1	M=0	M=-1	M=-2	M=1	M=0	M=-1
2	2	$\frac{1}{\sqrt{6}}$	0	0	0	0	0	0	0
2	1	0	$\frac{1}{2\sqrt{6}}$	0	0	0	$\frac{1}{2\sqrt{2}}$	0	0
2	0	0	0	0	0	0	0	$\frac{1}{\sqrt{6}}$	0
2	-1	0	0	0	$\frac{-1}{2\sqrt{6}}$	0	0	0	$\frac{1}{2\sqrt{2}}$
2	-2	0	0	0	0	$\frac{-1}{\sqrt{6}}$	0	0	0
1	1	0	$\frac{1}{2\sqrt{2}}$	0	0	0	$\frac{-1}{2\sqrt{6}}$	0	0
1	0	0	0	$\frac{1}{\sqrt{6}}$	0	0	0	0	0
_1	-1	0	0	0	$\frac{1}{2\sqrt{2}}$	0	0	0	$\frac{1}{2\sqrt{6}}$

Table 5.2: Relative values of the z component of the electric dipole matrix elements for the potassium  $4^2P_{1/2} \rightarrow 4^2S_{1/2}$  resonance. Each element in the table should be multiplied by the factor  $\mu_o$ .

routes,

$$A_{\substack{out \ of \\ F'=1,2}} = \frac{4e^2\omega^3}{3\hbar c^3} \frac{1}{2F+1} \sum_{F} \sum_{qM'M} |\langle F'M' \mid \vec{r} | FM \rangle|^2$$

$$= \frac{32\pi^3}{3\hbar \lambda^3} \frac{1}{2F+1} \sum_{F} |\langle F' \parallel \mu(1) \parallel F \rangle|^2 ,$$
(5.49)

where I have represented  $\vec{\mu} = e\vec{r}$ . I can explicitly write out the terms appearing in the above sum,

$$\sum_{F} |\langle F' \parallel \mu(1) \parallel F \rangle|^{2} = |\langle 1 \parallel \mu(1) \parallel 1 \rangle|^{2} |\langle 1 \parallel \mu(1) \parallel 2 \rangle|^{2}$$

$$= \left[ -\frac{\mu_{o}}{2} \right]^{2} + \left[ -\frac{\sqrt{5}\mu_{o}}{2} \right]^{2},$$
(5.50)

where I have used Table 5.1 to evaluate the given matrix elements. Because the spontaneous emission rate and value of the summation in Eq. 5.49 is known, the only unknown is then  $\mu_o$ . Solving in terms of natural atomic units (with a wavelength of  $\lambda = 770$  nm) then gives

$$\mu_o = 4.23ea_o.$$
 (5.51)

From this I now need to calculate the total effective matrix elements between the  $4S_{1/2}$  (F=1)  $\rightarrow 4P_{1/2}$  manifold  $(a \rightarrow b)$ , and between the  $4S_{1/2}$  (F=2)  $\rightarrow 4P_{1/2}$  manifold  $(c \rightarrow b)$ . These will involve a sum over all of the possible levels in the  $4P_{1/2}$  manifold that can decay to the F=1 ground state in the first case, or the F=2 ground state in the second case. Using the results in Table 5.2, the total effective matrix elements are found as

$$|\mu_{ba}| = \left[ \sum_{F'} \left| \left\langle F'M' \left| \mu_o^{(1)} \right| 1M \right\rangle \right|^2 \right]^{1/2} = \frac{\mu_o}{\sqrt{2}}$$
 (5.52)

and

$$|\mu_{bc}| = \left[ \sum_{F'} \left| \left\langle F'M' \left| \mu_o^{(1)} \right| 2M \right\rangle \right|^2 \right]^{1/2} = \mu_o \sqrt{\frac{5}{6}} .$$
 (5.53)

For one familiar with such matrix element calculations, these results are not unexpected: the matrix elements differ only by the square root of the ratio of the number of magnetic sublevels in the initial state (five to three).

## 5.5.2 The Rabi frequency

An important conclusion reached from Eqs. 5.52 and 5.53 is that because the matrix elements differ, they result in different Rabi frequencies for transitions between the states  $b \to a$  and  $b \to c$  even for the same pump and probe intensities.

The Rabi frequency for a transition between two atomic states was previously defined in Eq. 5.4 to be  $\Omega_{ij} = 2\mu_{ij} \cdot \mathcal{E}(\mathbf{r},t)/\hbar$ . Given that the field intensity is

$$I = \frac{c}{2\pi} \left| \mathcal{E}(\mathbf{r}, t) \right|^2 , \qquad (5.54)$$

I solve for the Rabi frequency as

$$\Omega_{ij} = \frac{2\mu_{ij}}{\hbar} \sqrt{\frac{2\pi}{c}I} \ .$$

After performing a few unit conversions, I write the Rabi frequency in the following useful form,

$$\Omega_{ij} \text{ (MHz)} = 1.12 \ \mu_{ij} \text{(ea}_o) \ \sqrt{I \ \text{(mW/cm}^2)} \ ,$$
 (5.55)

where I have indicated that the matrix element is specified in units of  $ea_o$  and the intensity in units of  $mW/cm^2$ . The resulting Rabi frequency is given in MHz.

The intensities for various pump and probe beam settings were calculated in Sec. 4.8.4, and reasonable values of the effective dipole matrix elements were just derived in Sec. 5.5.1. From these numbers, I arrive at pump beam Rabi frequencies of about  $(\Omega_{ba})_d \simeq 7.5 \times 10^3$  and  $(\Omega_{bc})_d \simeq 1.0 \times 10^4$ . After attenuation, the range of probe Rabi frequencies I typically work with is  $(\Omega_{ba})_p \simeq 75 - 1500$  MHz and  $(\Omega_{bc})_p \simeq 97 - 1950$  MHz. As described a bit later, however, I believe these estimates to be significantly larger than the working Rabi frequencies.

#### 5.5.3 Spontaneous emission rates

Calculation of the individual spontaneous emission rates from the b manifold (involving all of the levels in the  $4P_{1/2}$  state) to levels a and c is the final problem to solve using the dipole matrix elements. The spontaneous emission rate for any individual transition can be calculated as

$$A_{F'\to F} = \frac{32\pi^3}{3\hbar\lambda^3} \frac{1}{2F+1} \left| \langle F' \parallel \mu(1) \parallel F \rangle \right|^2 . \tag{5.56}$$

The only difference between the above equation and Eq. 5.49 is that the experimentally observed spontaneous emission rate necessarily sums over all possible transitions allowed by the Wigner-Eckart theorem. The observed rate

is thus larger than any of the individual rates between the states. Note that Eq. 5.56 has no dependence on the magnetic sublevels M or M'.

Using Eq. 5.56 we calculate the total decay rate out of level b to level a as

$$\gamma_{ba} = A_{F'=1 \to F=1} + A_{F'=2 \to F=1} = 1.33 \times 10^7 \,\text{sec}^{-1}$$
, (5.57)

and the rate out of level b to level c as

$$\gamma_{bc} = A_{F'=1\to F=2} + A_{F'=2\to F=2} = 2.66 \times 10^7 \,\text{sec}^{-1}$$
. (5.58)

The branching ratio for spontaneous decay from the excited state to the lower ground state versus the upper ground state is then one to two.

#### 5.5.4 Ground state decay

Although the theory allowed a calculation of the spontaneous decay rates out of the excited state, I cannot perform such a calculation for the population decay rates  $\gamma_{ca}$  and  $\gamma_{ac}$ . This results from the fact that both levels c and a are ground states, and hence have theoretically infinite lifetimes. In the theory calculations, this might indicate we should take the population decay between the ground states to be identically zero. However, I want to use parameter values that well represent the experimental situation, and due to resonant scattering processes taking place in the experimental atomic medium, there is a measurable (though small) population transfer rate between the states. These rates can even be unequal due to the different number of magnetic sublevels in each state.

In virtually all of our theoretical calculations, I model the population transfer between levels  $c \leftrightarrow a$  with nonzero population decay rates. Typical values used in the calculations are  $\gamma_{ca} = 0.64$  MHz and  $\gamma_{ac} = 0.32$  MHz. In addition,

nonzero population decay rates necessarily lead to a nonzero dephasing rate from c to a, because the total dephasing rate  $\Gamma_{ca}$  is always greater than or equal to the dephasing rate due only to natural broadening,  $\Gamma_{ca}^o = 0.5(\gamma_{ca} + \gamma_{ca})$ . A typical dephasing rate is  $\Gamma_{ca} = 0.8$  MHz.

#### 5.5.5 What are the working intensities?

In conjunction with the experimental parameters described in Chapter 4, estimates of the matrix elements, decay rates, and Rabi frequencies should results in spectra that reasonably reflect the experimental conditions. Initial tests of the theory parameters, however, produced atomic responses quite different from what I expected. A bit of testing quickly demonstrated that this resulted from Rabi frequency estimates that were likely far too large.

Theoretical results in conjunction with comparisons to experimental spectra lead me to believe we are not actually working at the high intensities predicted by the estimates of the beam sizes (and powers) in the vapor cell given in Sec. 4.8.4. I do not notice any effects indicating the huge differential Stark shifts that would result from such high beam intensities. Nor do I see Rabi scattering features detuned from the pump field by 2 or 3 GHz, as they would be at these intensities. In addition, at very high intensities the ground state populations are moved around in such a way as to destroy any Raman gain. This was shown in Fig. 5.8, where numerical theory verified the extinction of Raman gain for Rabi frequencies more than a few times the given ground state splitting. Because it is indisputable that significant Raman gain was experimentally seen, I believe that the actual pump and probe beam intensities are smaller than those given in Sec. 4.8.4.

There are a few possible explanations as to how we can be working at lower intensities than those measured using the beam profile technique, and hence I do not worry too much about this apparent disagreement. First, self-defocusing effects are visibly present in the beam and prevent an exact determination of the beam diameter inside the potassium cell. Self-defocusing comes about when temperature changes in the cell change the potassium vapor pressure, which changes the index of refraction of the sample, and hence the beam overlap and absorption in the cell. At high enough temperatures, as the probe beam nears and scans through resonance, the beam blooms to three times is normal size and at times even displays a distinct ring pattern. This self-defocusing causes the beam to partially break up, reducing the intensity seen by the atomic medium. It is difficult to determine the exact magnitude or effect of self-defocusing, but a factor of two, five, ten, or more difference in calculated versus actual beam intensity is not farfetched.

In addition, the theory assumes a constant intensity profile even through the beams are measured to be approximately Gaussian. Because the pump and probe beams intersect at a finite crossing angle, the probe beam atoms in the interaction region then see a spatially varying intensity profile. To make things even more complicated, it is quite possible that the two-photon Raman transition is saturated in the center of the actual probe beam profile, and not saturated toward the beam edges.

How might the variable, and perhaps saturated, beam profile affect the results? Recall that the gain proved to be critically dependent on the beam focus and crossing angle. Due to saturation, the gain in the wings of the beam could be one or two orders of magnitude higher than that in the center of

the beam. It is quite possible that in tweaking up the two-photon Raman gain, the best effects were seen when the probe beam sits on the tails of the pump beam, away from the tight focus and high intensities. The transitions of interest would no longer be saturated, yet there would still be a steady flow of optically pumped atoms across the probe beam profile. The measured optical spectrum could then correspond to intensities in the wings of the pump beams, intensities which are far lower than those predicted at the beam center.

Due to these factors, it seems necessary to revise my estimate of the pump and probe Rabi frequencies significantly downward. I feel that new, reasonable estimates for the pump Rabi frequency are  $(\Omega_{ba})_d \simeq 1200$  MHz and  $(\Omega_{bc})_d \simeq$ 1800 MHz, while the probe Rabi frequencies fall in the range  $(\Omega_{ba})_p \simeq 6 - 120$ MHz and  $(\Omega_{bc})_p \simeq 8 - 150$  MHz

# 5.6 Comparison between theory and experiment

Now comes the time to test the theory in a comparison of the shape of the theoretically predicted absorptive response with actual experimental data. I want to see what gain and loss features are predicted by the theory and where they are located when parameter values closely corresponding to experimental circumstances are input into the computer code.

Figure 5.10 shows the Doppler-averaged, single-atom response of the driven system as a function of the probe-beam frequency for various probe-beam intensities. Qualitatively, the theory produces the correct intensity dependence of the Raman transition probabilities, as seen through comparison with Fig. 4.12. At low probe Rabi frequencies, the one-photon Raman gain is quite large

– up to a few thousand percent gain. As the probe Rabi frequency increases, the one-photon transition saturates, two-photon gain becomes apparent, and then when it too saturates three-photon Raman gain is seen as well. The Raman peaks are appropriately spaced at the hyperfine splitting (and its subharmonics) of the modeled atomic ground state. Note that here I have explicitly quoted the theoretical probe beam intensities, whereas in Chapter 4 uncertainty in the beam sizes due to effects such as self-focusing forced us to specify the probe power rather than the probe intensity. It should be obvious that the theory reproduces the correct general trends in the intensity dependent spectrum.

As explicitly demonstrated in Fig. 5.11 for a single value of the probe beam intensity, there is excellent qualitative agreement between the theoretical curves and the experimental data. (The experimental data is taken from that shown previously in Fig. 4.12b.) All of the correct features are duplicated, including the one-photon Raman gain, two-photon Raman gain, dispersive Rayleigh resonance, and broad Rabi resonance. The only peak in the experimental data not duplicated by the theory is due to one-photon Raman gain from the  $^{41}K$  isotope present in our vapor cell. As the theory is a single-atom theory, and I input parameter values corresponding only with the  $^{39}K$  isotope, it would be worrisome if the theory did predict this isotopic gain peak!

As one would expect in an incomplete theory, the quantitative agreement is not as exact. The heights of the Raman peaks relative to each other and to the Rabi resonances do not always match as well as they appear to in Fig. 5.11. Especially at high pump and probe Rabi frequencies the Raman resonances show a sensitive dependence on the choice of  $\gamma_{ca}$  and  $\gamma_{ac}$  decay rates. At high Rabi frequencies the atomic populations are severely modified by the laser

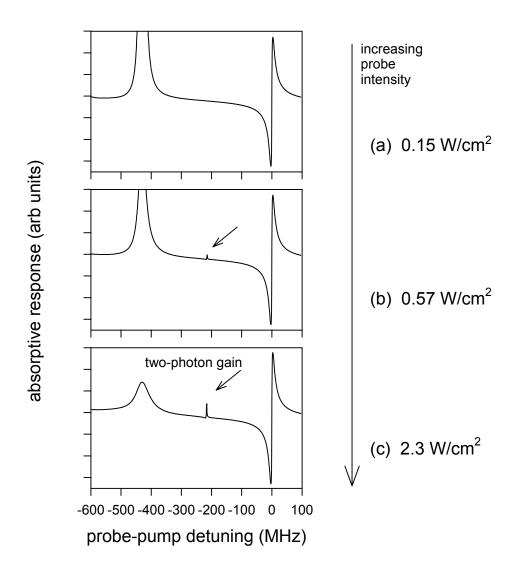


Figure 5.10: Theoretical dependence of the probe transmission spectrum on probe beam intensity. This should be compared with Fig. 4.12.

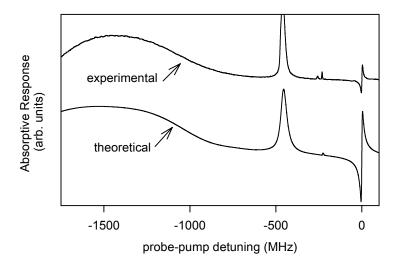


Figure 5.11: Comparison between the shape of the calculated theoretical output spectrum versus actual experimental data. Parameter values used in this plot are:  $(\Omega_{ba})_d = 560$  MHz;  $(\Omega_{bc})_d = 740$  MHz;  $(\Omega_{ba})_p = 90$  MHz;  $(\Omega_{bc})_p = 115$  MHz;  $\Gamma_{ba} = \Gamma_{bc} = 3.2$  MHz;  $\Gamma_{ca} = 0.8$  MHz;  $\gamma_{ba} = 2.1$  MHz;  $\gamma_{bc} = 4.2$  MHz;  $\gamma_{ca} = 0.64$  MHz;  $\gamma_{ac} = 0.32$  MHz;  $\Delta_g = 450$  MHz; and  $\Delta_p = -1440$  MHz.

beams, and hence changing the equivalent optical pumping effectiveness by changing the  $c \leftrightarrow a$  decay rates can significantly effect the expected gain or loss in the atomic medium. Additionally, in almost all of the calculations the Rayleigh scattering feature appears broader and larger than that seen in the data. Only by modifying the decay and dephasing rates (in an unphysical manner) can this feature be more accurately matched. Finally, the size and location of the Rabi scattering feature is quite dependent on the choice of detuning parameter. This feature can be moved around virtually at will simply by changing the detuning.

Despite these problems, Figs. 5.10 and 5.11 represent an impressive theoretical accomplishment. These figures should make it clear that our semiclassical theory reasonably describes the processes that occur in a system composed of three-level atoms interacting with two laser beams (such as a potassium atom explored using pump-probe spectroscopy). The theory reproduces the most important processes affecting the atom, including optical pumping, Raman scattering, and Rayleigh and Rabi scattering. The scattering features also demonstrate the correct general intensity dependences. Additionally, the theory accurately accounts for the effects of Doppler broadening. A future version of the theory which includes propagation effects and the magnetic sublevels of potassium should provide an excellent theoretical representation of the experimental system that can profitably used for its predictive capabilities.

## Chapter 6

## Previous Work on Two-Photon Lasers

#### 6.1 Theoretical Work

The past few chapters have described work done in the development of a robust two-photon amplifier using two-photon stimulated Raman scattering as the basis for producing two-photon gain. Future work in this system will first explore the characteristics of this nonlinear amplifier, and then focus on building a two-photon Raman laser. As described in Chapter 2, building a two-photon laser from a two-photon amplifier is a nontrivial task, although the large, spectrally distinct two-photon gain displayed by in the Raman system should simplify matters considerably. Theoretical and experimental explorations into two-photon lasers have a rich history, and this chapter serves as a review of the literature written about two-photon lasers from their conception to the present time. This is useful not only because it finally collects all of the literature on two-photon lasers in one place, but also because it helps to further emphasize some of the interesting features of these devices.

Researchers have been intrigued by two-photon lasers for the past three decades because the highly nonlinear character of the laser challenges our ability to describe its behavior, especially at the quantum level. A cursory glance at the theoretical literature on two-photon lasers might lead one to believe that the system is well understood. However, a closer inspection reveals that there are contradictory predictions concerning even the most basic properties of the laser. Unfortunately there has been little guidance from experimental work, because two-photon laser action has been realized only under limited conditions. This situation is a result of the trade-off between obtaining large two-photon gain (which occurs at high intensity) and avoiding competing processes such as normal one-photon lasing to other atomic states, energy level shifts, and multi-wave mixing. Typically, two-photon lasing is either obscured or completely suppressed by the competing processes.

A recent resurgence of interest in two-photon lasers has been motivated in part by the realization of a two-photon maser [25] and by the introduction of an innovative scheme for obtaining multi-photon gain in the optical part of the spectrum. The new gain medium was successfully used in the first demonstration of continuous-wave two-photon optical lasing [18], and was an exciting triumph of experimental quantum optics. Although the realization of a two-photon laser finally verified some of the theoretical predictions concerning its properties, a number of questions remain unanswered. This chapter is intended to review the literature, controversy, and conflicting predictions written to date about the two-photon laser. The chapter considers theoretical work and experimental progress independently. Within both the theoretical and experimental sections, there is a loose attempt to group the papers thematically, where then within each thematic section the papers are explored chronologically.

#### 6.1.1 Early Papers

Quantum amplifiers based on two-photon processes were discussed quite early in the development of nonlinear optics. The first mentions of an oscillator based on two-quantum transitions – a two-photon laser – were independently made by Prokhorov [1], a Russian scientist, and Sorokin and Braslau [2] from IBM Laboratories in the early 1960's. It is interesting to note that Prokhorov did not turn to a scientific or industrial journal to publish his new ideas concerning the two-photon laser. Rather, he included them in a lecture delivered in Stockholm when he received the 1964 Nobel Prize in Physics (with C. H. Townes and N. Basov for invention of the maser and a theory of coherent atomic radiation)!

Two-quantum oscillators offer the possibility of tunable frequency lasing since the only theoretical frequency constraint is that of energy conservation – the sum of the two frequencies generated must be equal to the frequency difference between the levels of the transition. The possibility of achieving high light intensities in these systems also piques interest in the development of two-photon lasers [56]. Saturation effects limit the power output of most lasers, yet because two-photon lasers have far higher saturation intensities than their one-photon counterparts they have the potential to achieve higher laser power than the usual one-photon laser. Since only modest power, fixed-frequency lasers existed in the early sixties, experimentalists were intrigued and excited by the opportunities these new oscillators offered. Theorists were also intrigued, because the nonlinearities associated with a two-photon laser challenged our understanding of the interaction of light with matter.

Only a few years after the first proposal of two-photon lasers, Lambropoulos [57], [4] discusses a quantum amplifier based on two-photon transitions. He

finds that such an amplifier has novel coherence and statistical properties, quite unlike a one-photon laser or any other light source available at that time. His results lead to predictions that the output state from a two-photon oscillator may also have novel statistical properties. Despite the passage of almost thirty years since these ideas were first expressed, questions concerning the light output from two-photon amplifiers and lasers remain unanswered even today.

Carman [58] uses a rate-equation viewpoint to examine amplifiers based on a two-photon stimulated emission. He enumerates the difficulties anticipated in realizing practical two-photon amplifiers, including small gain, maintaining spatial coherence, and inversion depletion through the amplification process. Gordon and Moskvin [59] consider optical amplification by two-photon transitions and multiphoton transitions in general. They find that the nonlinear character of two-photon stimulated emission and amplification lead to a number of distinguishing features of the pulse propagating through the medium, including an amplification threshold and some early results on the effect of an external beam to "ignite" the transition. Narducci et al. [60] present a detailed theory for a degenerate two-photon laser amplifier, and discuss pulse propagation through a two-photon absorbing medium. They derive the Bloch equations and construct an equation for the pulse energy density in the absorbing medium, obtaining an unstable pulse envelope with a Lorentzian line shape.

#### 6.1.2 Semiclassical Approach

General theoretical treatments of the two-photon laser have been performed classically, semiclassically and quantum mechanically, where often the laser characteristics and behavior under study determine the approach taken. In semiclassical laser theories the electromagnetic field is treated classically using Maxwell's equations, while the atom is treated quantum mechanically in terms of its discrete energy levels and atomic transitions.

Hoshimiya, Yamagishi, Tanno, and Inaba [61] present a semiclassical analysis of two-photon laser oscillation in an optical cavity. They derive a laser threshold condition and find a need for injection of a complimentary field into the cavity for triggering two-photon stimulated emission. Bulsara and Schieve [62] also consider a semiclassical treatment of the two-photon laser. In agreement with Narducci's results [60] for the two-photon amplifier, they find an unstable solution for the photon energy density. They go on to show using two separate methods that this instability is a consequence of retaining higher order terms in the solution for the energy density, which corresponds to the neglect of virtual processes in a quantum theory.

An early paper by Schubert and Wiederhold [6] analyzes the time dependent photon flux, the initiation of the lasing process, and the effects of an injected starting pulse in a two-photon laser, calculated on the basis of classical rate-equations. For calculational simplicity their analytic solution assumes that the population inversion remains constant. This unfortunately leads to nonphysical (and infinite!) results for the photon flux. Fernández and Sainz [63] perform a density matrix treatment of a two-photon laser. Theirs is the first two-photon laser treatment dealing with saturated two-photon emission. Songen [64] uses a

steady-state solution of the optical Bloch equations to discuss continuous-wave two-photon lasing, but his results are not self-consistent and thus cannot be compared with other results. Concannon and Gauthier [65] propose a simplified effective model for a two-photon laser with injected signal based on a rate-equation analysis. They look at the dynamical behavior of both the photon flux and population inversion above and below threshold, and see evidence of bistability and a first-order phase transition at threshold.

#### 6.1.3 Simple Quantum Theory

The different approaches toward the development of the theory of a two-photon laser all have different strengths and weaknesses. A classical or semiclassical treatment is insufficient for the study of some of the novel coherence properties and stability properties of the laser. In fact, the majority of the literature on two-photon lasers is devoted to a quantum description of their behavior, mainly because a great portion of the theoretical interest in a two-photon laser lies in their intrinsic nonlinearities and nonclassical characteristics. Quantum theories quantize both the atomic energy levels and the field photons and modes. Semiclassical theories approximate the full quantum treatment by treating the field in a classical manner. In the 1960's and early 1970's, a quantum description of one-photon lasers, which involve a single photon absorption and emission per atomic transition, proved very successful in explaining the bulk of one-photon laser phenomena. It wasn't long before researchers started modifying the quantum theory in order to analyze two-photon lasers as well.

A detailed theory of two-photon lasers was put forth in a series of papers by Wang and Haken in 1984. They perform an analysis based on the exact microscopic Hamiltonian which assumes a high-Q cavity (cavity linewidth  $\ll$  atomic linewidth), a circulating field that is not too intense, and neglects Stark shifts of the levels [66]. The restriction on cavity Q-value allows atomic variables to be adiabatically eliminated, and that on field intensity allows neglect of higher-order terms in the equations. Although they start from a full microscopic Hamiltonian, Wang and Haken first simplify the analysis by averaging over the fluctuation and dissipation of the atoms and lightfield in the quantum mechanical equations of motion for the field amplitudes, atomic dipole moments, and inversion. They solve the resulting semiclassical equations for the stationary solutions and their stabilities, and conclude that there exists a critical value of inversion below which there cannot exist any stable ordered state. The photon number of a mode thus starts from the critical value at the critical inversion and increases with the inversion. This is different from the behavior of one-photon lasers in which the photon number starts from zero value at threshold.

A further treatment by Wang and Haken [67] retains the full quantum complexity of the system using a Fokker-Planck analysis, and addresses thermal fluctuations (noise) and stability in the two-photon laser, both with and without an injected signal as a trigger. They show that a two-photon laser displays a first-order phase transition at the onset of lasing – there is a discontinuous jump in the laser output as threshold is reached. This contrasts with the continuous, second-order, change in the field amplitude at threshold in the one photon laser. Also, in agreement with the heuristic model of laser threshold discussed in the introduction, they find that the laser will not make this jump to the lasing state until the photon number exceeds a certain threshold even

when the inversion exceeds the threshold value. In general, fluctuations due to spontaneous emission are not enough to overcome this threshold. As a result, they also study the effect of injecting a signal into the laser cavity to start the transition [8]. They find that a degenerate two-photon laser with an injected signal resonant with the frequency of the laser has threshold behavior again analogous to a first-order phase transition. There exists a critical value of the inversion below which the lightfield amplitude is single valued, and above which bistability occurs.

With the notable exception of the Fokker-Planck treatment of the twophoton laser described above [8], the majority of researchers approach the quantum theory of the two-photon laser by generalizing the Scully-Lamb [68] theory developed for ordinary single photon lasers (the so-called master equation formalism). The Scully-Lamb approach to the quantum theory of the laser oscillator uses a density matrix description of the field inside the resonator. Both the radiation field and atomic medium are treated quantum mechanically, and instead of describing the radiation field in terms of amplitudes, phases, and frequencies it is described quantum mechanically by a density matrix. The atom-field interaction is described by a microscopic Hamiltonian. Generally, the theory includes a nonlinear active medium for gain and a damping mechanism for loss, treats only a single-mode laser, and neglects the effects of Doppler broadening and spatial variations in the field. The complete equations of motion for the radiation density matrix are found and are used to compute physical properties of the laser. The diagonal density matrix equations describe the flow of probability for finding photons in the laser cavity due to stimulated emission and damping, and are used to calculate mean photon

numbers and other photon statistics. The off-diagonal elements can be used to find lineshapes, correlation times, and the spectral profile.

McNeil and Walls [56] propose one of the first theoretical descriptions of the two-photon emission process, and advance the theory of possible two-photon lasers. They use a quantum mechanical model generalized from the Scully-Lamb one-photon laser model and derive the photon statistics of the laser fields. They separately consider multiphoton lasers which preserve detailed balance and those that don't. Detailed balance assumes a multiphoton loss mechanism for the laser light of the same order as the multiphoton gain from stimulated emission. In an n-photon laser, n photons are lost simultaneously in a stimulated de-excitation process. For a two-photon laser, detailed balance then only allows for two-photon loss, while a more general theory allows for onephoton loss as well. McNeil and Walls find laser threshold behavior analogous to a second-order phase transition and a photon distribution narrower than that for thermal light. Görtz and Walls [69] use a less computationally intense method to duplicate the results of McNeil and Walls in their solution of a twophoton laser master equation without detailed balance. Nayak and Mohanty [70] extend the previous theories to take atomic motion and Doppler broadening into account, inclusions which affect the performance of one-photon lasers. They compare the photon distribution for one- and two-photon lasers and find a narrowing of the two-photon laser distribution line. They note that the restrictive two-photon loss mechanism may affect their results, a fact that is further discussed by other authors.

<sup>&</sup>lt;sup>1</sup>Later papers (including one by Reid and Walls [89]), re-evaluate these early analyses and come to the consensus that the transition through laser threshold will be first-order phase transition.

The approach taken by Sczaniecki [71] does not involve detailed balance, but rather assumes a single–photon loss mechanism related to transmission at the end mirrors. He performs a stability analysis of the solutions derived for the operators characterizing the system, and shows that the transition through the threshold of a multiphoton laser is a first-order phase transition. A later paper by Sczaniecki [72] extends his previous results, which are valid only for the degenerate case, to the case where the multi–photon emission concerns more than one distinct field mode. The transition through the multiphoton laser threshold is quite generally found to be a first-order phase transition.

Zhu and Scully [73] study a nondegenerate two-photon laser in a cascade three-level atomic system. Two beams of different frequencies are incident on the atomic system, and they specifically look at the effects of the two fields on each other in terms of population redistribution and gain enhancement or reduction. Holm and Sargent [74] use a two-photon two-level model in a quantum theory of multiwave mixing in which one strong classical wave and one or more weak quantum waves interact in a nonlinear medium. They present a detailed calculation of the two-photon resonance fluorescence spectrum which, unlike most previous work, accounts for the dynamic Stark shifts which play an important role in two-photon transitions. The Stark shifts lead to a noticeably asymmetric fluorescence spectrum, which is related to probe gain and loss in the absorption spectrum. Although the results technically apply only to two-photon gain, their pertinence to a two-photon laser is evident.

Boone and Swain [75] author a series of papers deriving the equations of motion for the field density matrix of the two-photon laser starting from the full microscopic Hamiltonian. They calculate mean photon numbers, laser linewidths for each mode, frequency shifts (amount by which the operating frequency of the laser is shifted from the cavity frequencies), and cross-correlation coefficients (extent to which phase fluctuations in the output of the laser modes are correlated). They compare the results with those found using an effective Hamiltonian, which only includes two-photon processes, while a full quantum theory accounts for stepwise (cascade) processes as well. It is expected, and previous theories assume, that the effective Hamiltonian proves a good model whenever the single photon detuning of the intermediate state from the laser frequencies is large, reducing the probability of stepwise processes. However Boone and Swain show that the laser must also be operating above, but not too far above, threshold in order to prevent power broadening from bringing the intermediate state into effective resonance. They conclude that the effective and full Hamiltonian approaches predict identical diagonal density matrix elements in the right limits. The off-diagonal elements, however, significantly differ between the models, mainly due to the effective Hamiltonians neglect of Stark shifts, and the strong dependence of the off-diagonal element quantities on detailed atomic structure. Their work thus catalogues regions of validity for the differing models.

Cheng and Haken [76] describe quantum fluctuations and photon statistics in the two-photon laser by starting with a master equation for the density operator of the atoms and the field mode. Zhu and Li [77] use a three-level atomic system as their basis for a two-photon laser model, and note the differences in the quantum theory that arise from an exact microscopic versus effective Hamiltonian. They study the photon statistics in the exact case, and look at the effects of detunings on their results.

Many early studies on the quantum statistical properties of the radiation coming from two-photon lasers concerns photon statistics, while little attention is given to the study of the natural linewidth of the laser. Swain [78] remedies this situation in the late eighties when he considers the two-photon laser using an extended Scully-Lamb theory, and focuses on calculation of linewidths and cross-correlation coefficients. He shows that the two-photon laser is a source of tunable, strongly positively cross-correlated light when operating well above threshold. According to Swain, "cross-correlation is a topic of much current interest: crudely the reason is that whilst each mode of the laser may be noisy, the noises from the two modes may be so correlated that in an appropriate twophoton transition they may 'cancel', leading to an almost noiseless transition". Ashraf and Zubairy [79] also note the resurgence of interest in studying laser linewidths and related quantities, mainly due to the possibilities arising for noise quenching. They evaluate the natural linewidth for a two-photon laser based on an equation of motion for the field obtained by suitably generalizing Scully-Lamb theory.

Yang, Huang, and Hu [80] carry out a quantum theory of a nondegenerate two–photon laser using a three-level model where all the states are the same parity. Earlier models dealt with the problems of a two-photon laser in a two-level scheme, and later work extended it to the three-level case. Yet few, if any, previous studies looked at the effect of other *same* parity intermediate levels on a two-photon transition, instead focusing on the enhancement effects of opposite parity intermediate levels. Yang *et al.* find that the radiation field displays sub-Poissonian statistics (leading to antibunching) and confirm that the laser at threshold goes through a first-order phase transition.

Lu [81] takes a Q-function approach to the quantum theory of the twophoton laser in which he employs quasiprobability distributions for the intensity and phase of the laser to describe the field in terms of classical numbers rather than operators. He compares his approach with those involving the full microscopic Hamiltonian and the effective Hamiltonian, and claims that triggering is required to start laser oscillation only if linear gain in the laser is less than cavity loss, differing from the effective Hamiltonian results. He also determines that the general expression for photon number variance does not approach a Poisson distribution as in the one-photon laser. This leads to interesting nonclassical photon statistics, as described in the next section.

## 6.1.4 Non-classical light: Squeezing and Photon Statistics

A great deal of interest has been generated in studying the coherence properties and photon statistics of a two-photon laser, mainly due to early predictions of unusual behavior and the occurrence of nonclassical light. In order to better understand these predictions, I first briefly explain nonclassical light, and squeezed light in particular. Much of the following is based upon a good review article by Teich and Saleh [82].

The electromagnetic field associated with a single mode of radiation may be described by two independent components such as its amplitude and phase or its cosine and sine quadratures. According to quantum mechanics and the Heisenberg uncertainty principle, the two components cannot be simultaneously known with perfect precision. Yet because most usual light sources have no preferred quadrature component, the two uncertainties are equal and in-

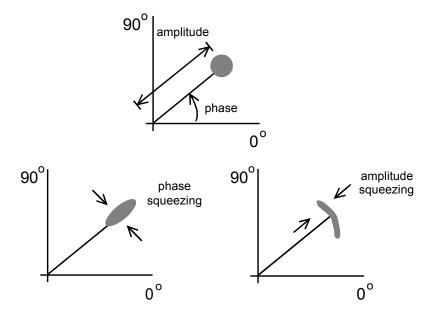


Figure 6.1: Representation of amplitude and phase squeezing

dependently fulfill an uncertainty relation. However the Heisenberg inequality does not forbid a decrease in the uncertainty of either quadrature below the given limit provided that the uncertainty of the other quadrature is increased. Thus, for example, the amplitude noise on a beam of light may be reduced below the Heisenberg limit, while the phase noise is correspondingly increased, as illustrated in Fig. 6.1 Similarly, the photon number associated with a mode may be known exactly, in which case the phase of that mode is totally uncertain. Light with a minimum uncertainty product, but with an unequal distribution of fluctuations in the two quadratures, is said to be quadrature squeezed. Light whose photon-number fluctuations are smaller than those of the Poisson distribution is said to be photon-number squeezed, or "sub-Poisson".

The statistical properties of squeezed states of light or sub-Poissonian light fields cannot be calculated using techniques analogous to classical probability theory, requiring instead a full quantum description of the light; squeezed states and sub-Poissonian light fields are hence examples of nonclassical light fields. Another example of a nonclassical, or quantum, light field is one which displays a second-order coherence less than one. All existing theories that distinguish classical from quantum coherence properties depend on the degree of second-order coherence, which is defined in terms of the correlation of light intensities at two space-time points [3]. This coherence represents the normalized probability of two photons arriving at a location simultaneously. A second-order coherence greater than one indicates a high degree of correlation and describes photon bunching, while a field distribution in which the photons are uncorrelated (second-order coherence less than one) results in anti-bunched light. Though thermal or chaotic light has a second-order coherence greater than one and hence displays bunching, this coherence doesn't violate any classical inequalities and hence remains a classical light source. A second-order coherence less than one, however, violates classical inequalities and represents quantum light.

Quantum light may be quadrature-squeezed, have sub-Poisson statistics, or have a correlation function less than one. A fairly general relationship between photon-number squeezed light and anti-bunched light exists, in that if the variance of the number of counts is in excess of that given by the Poisson distribution, photons do not arrive at random, but are bunched. On the other hand, if the variance is less, the photons exhibit anti-bunching. There is not, however, a general relation between anti-bunching and quadrature-squeezing. Quantum states may exhibit anti-bunching but not squeezing, and only some squeezed states exhibit sub-Poissonian photon statistics and hence photon anti-

bunching.

Ideal (one-photon) lasers emit coherent light, which has quadratures whose fluctuations are equal and satisfy the minimum product permitted by the uncertainty principle. The photon-number fluctuations of such coherent light are governed by the Poisson distribution, in which the fluctuations in the number of photons is equal to the square root of the photon number. A typical laser also has a second-order coherence exactly equal to one. Typical laser light does not display bunching or squeezing of laser photons.

Squeezed light in particular proves quite exciting to researchers, mainly due to its noise reduction characteristics. Recent improvements in noise reduction techniques have created a situation in which quantum noise is frequently dominant over other noise sources in optical communications. If one can generate states with a quantum noise smaller than a coherent state (the output of typical lasers), such states could be profitably used in many applications. The twophoton laser is a candidate to produce the purely quantum effects of squeezing and antibunching. Yuen [83] points out that two-photon coherent states specifically the radiation states of ideal monochromatic two-photon laser operating far above threshold – have novel characteristics that may lead to potential device applications in both quantum noise reduction and experiments requiring low noise sensitivity. Hirota [84] carefully looks at the theoretical quantum noise properties of a two-photon coherent state (generated by the ideal twophoton laser) and finds that optical communication by two-photon lasers has certain advantages over that by conventional lasers, since no increase in uncertainly occurs in the measurement or detection process. Employing two-photon coherent states as the transmission states in optical communication minimizes

error probability and improves reliability. Rowe [85] approaches the problem quite differently, yet also predicts that the coherence properties of a two-photon laser are quite different from the standard laser and may display nonclassical effects, such as squeezing. In the pulse mode, two-photon lasers might also display pulse shortening behavior [86] not found in the one-photon case.

Soon after these first exciting papers appeared, however, the predictions of novel noise characteristics became contradictory and critically dependent upon the model used to describe the two-photon laser. Golubev [87] uses perturbation methods to investigate the quantum statistical properties of a two-photon laser when the cavity loss mechanism is simulated by a single photon process. He does not find qualitative differences between the photon statistics of a onephoton laser and a two-photon laser. Lugiato and Strini [88] systematically investigate two-photon optical bistability and two-photon lasing in a ring cavity. Again, contrary to expectations, no squeezing is found for a two-photon laser in the good cavity (high-Q) limit. A later study by Reid and Walls [89] that approaches the problem quite differently confirms this finding. Both of these papers model a two-photon laser using two-level atoms interacting via a two-photon transition with a single resonant-cavity field mode. Since a squeezed state is generated via a quadratic interaction of the electric field, the quadratic nature of a two-photon interaction makes a two-photon laser a prime candidate to exhibit reduced quantum fluctuations in one quadrature of the output field. However, both these papers show that an incoherently pumped laser will not generate squeezed states of light.

The controversy over the squeezing characteristics of a two-photon laser continues through the early eighties as a flurry of papers predicting that any intrinsic squeezing will be destroyed by spontaneous emission events due to the phase insensitivity of the resulting fluctuations. Scully et al. [90] study the noise properties of a two-photon correlated-spontaneous emission laser, a coherently pumped two-level two-photon laser in which the two-photon transition is driven by atoms injected into the cavity in a coherent superposition of the levels involved in the lasing transition. They show that this laser displays a reduction in spontaneous emission fluctuations and predict that it will exhibit net gain and phase squeezing simultaneously. In another nonlinear theory of the two-photon correlated-spontaneous-emission laser, Lu et al. 91 predict that the injected atomic coherence leads to stable phase locking and squeezing of the quantum noise in the phase quadrature of the laser light. Majeed and Zubairy [92] go on to show that even for very large phase fluctuations in the injected atoms, close to 50% phase squeezing can be achieved in the two-photon correlated-spontaneous-emission lasers. A recent paper also by Majeed and Zubairy [93] studies a two-photon phase sensitive amplifier, which responds differently in terms of gain or noise to the phases of the two light quadratures. An ideal phase-sensitive amplifier has previously been shown to display phase squeezing, and they extend the results to the realistic case where the driving field is modified by phase fluctuations. Fluctuations are shown to reduce, but not destroy, the squeezing.

All of these early papers deal with the case of zero detuning in the laser, and Hu and Sha [94] first study the influence of detunings on the squeezing effect in 1991. They find that in the good cavity limit a squeezed state may exist in two-photon laser in the off-resonance condition. A paper by Savage and Walls [95] examines the squeezing spectrum for a cavity field mode interacting

with an ensemble of three-level atoms by an effective two-photon transition. A three-level, rather than two-level, system as the squeezing medium has the advantage that the nonlinearity is not due to atomic saturation (which leads to spontaneous emission, a source of noise that destroys squeezing). This three-level nonlinearity allows them to find good squeezing in systems with dispersive bistability. In fact, they predict perfect squeezing at the turning points of dispersive optical bistability generated by two-photon transitions.

The predictions of squeezing in a two-photon laser have come full circle. Although finding squeezed states in a two-photon laser is no longer expected to be as simple or automatic as it was once believed to be, the general consensus is that squeezing is theoretically possible in a two-photon laser under certain resonance and cavity conditions. Whether these conditions are experimentally realistic remains to be determined.

Over the years, a number of differing predictions concerning the photon statistics of a two-photon laser have also been proposed. It is fairly well accepted that the statistical properties of two-photon laser light will display quantum behavior, yet identifying the exact behavior seems quite difficult. Using a Scully-Lamb detailed-balance laser model, McNeil and Walls [56] predict that photon distribution functions of a two-photon laser are narrower (sub-Poisson) than in the single photon laser. Relaxing the detailed balance restriction, however, yields two-photon lasers which demonstrate no significant difference in statistics from one-photon lasers. In a later paper [96] they show that the field produced by two-photon spontaneous emission into a vacuum has a second-order correlation function greater than two, thus offering the possibility of observing photon bunching. However, with an initial field present either bunching

or antibunching effects can be seen!

The confusions only get worse from here. Zubairy [97] investigates the two-photon laser with a *single* photon process as the cavity loss mechanism in the model. He finds the photon distribution function for a two-photon laser to be wider than a Poisson distribution, differing from McNeil and Walls [56] and other previous expectations. Bandilla and Voigt [98], like Zubairy, claim that models in which the losses at the mirrors are due only to two-photon absorption are unrealistic since photons do not escape in pairs, and such nonphysical models may modify the predicted statistics. They claim that under the proper circumstances, a two-photon absorber can bring an *arbitrary* field state into one displaying photon anti-bunching, and only a careful, realistic laser model can overcome these difficulties. They use a reasonable model in which single-photon absorption accounts for losses and find a photon distribution which displays small bunching and super-Poisson statistics.

A second paper by Zubairy [99] predicts that two-photon lasers display a non-classical second-order coherence, which is expected to result in photon bunching. A paper by Sharma and Brescansin [100] includes the effects of cooperative atomic interactions in their study of the statistics of a two-photon laser and finds nonclassical behavior qualitatively similar to that already described, though their quantitative results differ slightly. A further study of photon statistics and coherence properties by Lu [101] compares predicted results for an exact versus effective interaction Hamiltonian and catalogues the regions in which they agree. Bay and Lambropoulos [102] study the photon distribution of a two-photon laser and carefully account for the effects of the dynamic Stark shift. They reproduce the result that a two-photon laser with

no Stark shift and no detuning results in a super-Poissonian photon distribution. They go on to show that when a detuning is introduced in the case of a strong dynamic Stark shift, the statistics of the photon distribution changes from super-Poissonian to sub-Poissonian.

In summary, although the photon statistics of a two-photon laser are expected to differ from a one-photon laser, whether the new photon number distribution broadens or narrows, and how the second-order correlation function changes, is again critically dependent on which features are incorporated into the two-photon laser model. Only tests done on a two-photon laser itself will satisfactorily determine these outstanding questions.

#### 6.1.5 Bistabilities and Instabilities

There is a great deal of breadth and vigor within the field of nonlinear optics studying instabilities in active optical media. Just as squeezing and non-Poisson statistics attest to nonlinearities in an optical system, novel stability properties are another indication of interesting nonlinearities. Many of the stability properties of typical laser systems have been familiar to the experimental physicist since the early days of the laser, and mathematical developments in the study of nonlinear dynamical phenomena allowed these instabilities to be extensively studied. Similar theoretical studies on two-photon lasers would prove useful in understanding these novel quantum oscillators. The two-photon laser is expected to have nonlinearities quite different from, and far more complicated than, those of the one-photon laser due to the absorption and stimulated emission of two photons simultaneously in the amplification process.

Abraham, Lugiato, and Narducci [103] present a nice overview summarizing

the general methodology used to analyze instabilities in laser systems. Nearly all laser models, including two-photon laser models, derive their theoretical framework from coupled differential equations whose solutions can be viewed as trajectories in the phase space of the dynamical variables. When working with continuous-wave lasers, steady-state solutions to these equations are used to determine long-term laser behavior. A standard linear stability analysis<sup>2</sup> determines which of these steady-state solutions are realized in the system – only the stable solutions represent physical laser outputs.

Abraham et al. [103] apply the above procedure to look at the steady-state solutions for the degenerate two-photon laser. Their basic results are generally agreed upon and deserve a quick summary before mentioning the independent, and often controversial, results presented by a number of authors. Solutions for the mean photon number and inversion in a two-photon laser as a function of pumping are, in general, given by a trivial solution (nonlasing; zero-intensity) and a pair of nontrivial solutions as shown in Fig. 6.2. Irrespective of pumping, the trivial solution is always stable<sup>3</sup>, though two-photon spontaneous emission, neglected here due to its small probability of occurrence in the optical regime, can destabilize this solution. The two nontrivial solutions exist only above a certain value of the pump parameter, and for one the intensity of the solution grows with the pump parameter, while it decreases for the other. The negative slope portion of the steady-state curve is always unstable, so only the upper-branch (lasing) intensity is considered in most treatments. The stability of this

<sup>&</sup>lt;sup>2</sup>Details of a standard linear stability analysis are explored in Chapter 3, where such an analysis is performed on a rate-equation model of two-photon lasers.

<sup>&</sup>lt;sup>3</sup>In fact, even this is not universally agreed upon. Using a full microscopic Hamiltonian, Boone and Swain [75] find the solution at the origin to be unstable above threshold.

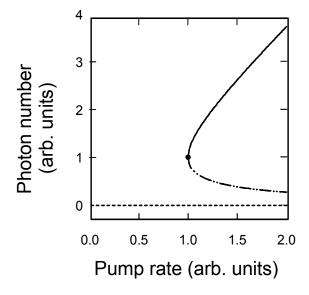


Figure 6.2: Steady-state behavior in the two-photon laser

branch varies with the pump parameter, and bistability between the zero- and upper nonzero-intensity solution, which only meet at infinity, will occur when the upper branch is stable.

Most researchers use the conventional linear stability analysis when approaching a theoretical examination of the stability of two-photon lasers and predict differing results simply because of different effects included in the individual laser models. Ito and Nakagomi [104] study the two-photon laser oscillation process and find the possibility of a first-order phase transition at threshold, as evidenced by their solutions for the complex amplitude of the field. Though many early stability analyses look only at the photon field, Ito and Nakagomi also explore the inversion. The solutions to the system of equations describing both the photon field and inversion are threefold, as described above. The upper branch stability condition depends on the relative magni-

tude between the photon and atomic decay rates, and has no counterpart in the single photon laser.

Reid, McNeil and Walls [7] present a unified approach to n-photon transitions which can occur in an optical cavity filled with two-level atoms. Their formalism describes the n-photon laser, the n-photon laser with injected field, and n-photon optical bistability, and they derive the state equations and stability conditions for each of these processes using a treatment similar to that of Sczaniecki [71]. They perform explicit calculations of semiclassical and statistical laser properties and find the two-photon laser to be bistable, resulting in a need for fluctuations or an injected trigger to make the transition to lasing.

Ning and Haken [105] author a number of papers concerning the dynamic behavior of the effective Hamiltonian two-photon laser. They systematically study the stability of the stationary states in the two-photon laser, and reproduce the now-familiar trio of stationary solutions. They first look at the mathematically simpler case of perfect tuning, then relax this restriction to study how unavoidable detunings [106] influence the stability of the two-photon laser. They show that the stability of the trivial solution is responsible for the bistability of the system between the trivial and nontrivial solutions near the lasing threshold. They also show that one of the nontrivial states is always unstable, and the stability of the other depends on whether the cavity is good, giving regions of stability, or bad in which case it is always unstable. Recall that a good cavity is one in which the cavity lifetime is much larger than the atomic lifetime. For an intermediate cavity, a linear stability analysis shows the existence of a self-pulsing instability that occurs through a Hopf bifurcation at a critical pump parameter, and they perform both an analytic and numeric

nonlinear analysis about this instability point [107]. The most interesting feature of this Hopf bifurcation is that, in opposition to the majority of lasers, the laser is stable for pump values larger than (and unstable for values smaller than) that corresponding to the bifurcation point. Finally, they also perform a preliminary study of the phase dynamics of a two-photon laser [108].

In a paper on generating ultrashort pulses using two-photon gain, Heatley et al. [109] carry out a stability analysis on the two-photon laser in the bad cavity limit, and find an instability in the two-photon continuous-wave field while the pulsed field remains stable. Wang and Guan [110] discuss instability and chaotic phenomena in the two-photon laser with injected signal for a homogeneously broadened single-mode ring-cavity laser. They observe not only steady state and periodic motion, but also chaos and hyperchaos.

Roldán, de Valcárcel and Vilaseca [111] study the operational conditions and stability of a degenerate two-photon laser. They adopt a semiclassical laser model based on a microscopic three-level Hamiltonian, and investigate the influence of a nonresonant intermediate level on the emission conditions and stability of a two-photon laser. Their model generalizes previous effective Hamiltonian models since it retains information about the intermediate level through parameters describing atomic population and frequency shifts. In their analysis they describe two important features of the two-photon laser: (i) the absolute stability of the trivial solution with the consequent necessity of triggering; and (ii) the existence of a Hopf bifurcation that destabilizes the steady lasing solution. A follow-up paper by de Valcárcel, Roldán, Urchueguía, and Vilaseca [112] extends the analysis by allowing for both degenerate and non-degenerate cases, analyzes the stability of the Hopf orbits, and numeri-

cally investigates the global dynamic behavior of the two-photon laser. Both papers concentrate on the influence of the intermediate-state parameters on the stability and dynamical properties of the two-photon laser.

Ovadia and Sargent [113] are among the few researchers not to use the conventional linear stability analysis, but rather study two-photon lasers using the "weak-sideband" approach, a common and intuitive approach taken when dealing with one-photon lasers. For one-photon lasers both approaches tend to yield the same instability boundaries, and this seems to be true for two-photon lasers as well. In the weak-sideband method, an instability is primed by the emergence of symmetric sidebands around an existing oscillating signal. This causes the output intensity to lose its stationary character and acquire an amplitude modulation, or instability. Ovadia and Sargent [113] study the buildup of sidemodes and sidemode instabilities in the two-photon laser, and find a two-photon laser, like a one-photon laser, becomes unstable if the sidemodes have positive net gain. Single and multiwavelength instabilities in two-photon laser operation are shown to occur. A later paper by Ovadia, Sargent, and Hendow [114] extends the theory and performs a preliminary investigation on the influence of AC-Stark shifts on two-photon laser dynamics.

#### 6.1.6 Recommended reading

As has become evident, the two-photon laser models employed by different authors vary significantly. For the reader unfamiliar with the myriad of theoretical work that has been done, it proves helpful to try to point them to one or two reasonably good, reasonably complete theoretical papers as references.

For a semiclassical theory, I recommend the related treatments by Roldán et

al. [111] and Vilaseca et al. [112] They present a three-level model of the twophoton laser, look at both the degenerate and non-degenerate cases, and retain
important information about AC-Stark shifting of atomic levels and population
induced level shifting. They perform a careful analysis of the laser's stability
properties, and study the effects of laser field detunings on laser behavior.

One notable deficiency of this model (and all other two-photon laser models
already discussed) is that it allows incident laser fields to interact only on a
single atomic transition, whereas in physical systems a field often interacts on
two or more transitions. In addition, because the model is semiclassical, by
definition it cannot predict or explain the laser's quantum properties, including
possible squeezing and non-classical photon statistics.

Papers dealing with the quantum aspects of the laser tend to be more specialized and more technically difficult to decipher, but they do predict laser qualities not available to a semiclassical analysis. I hesitate to recommend many quantum treatments of the two-photon laser, mainly because of their usual notation: they bandy about a and  $a^{\dagger}$  terms as if every optical physicist has been familiar with these quantities since junior high-school. Wang and Haken [66] present one reasonable quantum theory of two-photon lasers. They treat the dynamics and stability of a two-photon laser near threshold and the influence of noise characteristics. They consider both degenerate and non-degenerate lasers, and study the need for and effect of a trigger to initiate lasing. This is a wonderful initial treatment of the laser, useful as a starting point for more detailed treatments. Its most obvious deficiencies, however, include the fact that incident fields are again only allowed to interact on a single atomic transition, and parts of the treatment require a high-Q cavity

and relatively weak electromagnetic fields.

Another fairly general quantum theory, which takes a different approach than that of Wang and Haken, is that by Boone and Swain [75]. Like the semiclassical theory described above, their density-matrix approach includes the effects of AC-Stark shifts and intermediate state frequency shifts. They include effects of cavity detunings, look at steady-state solutions, and perform a careful a stability analysis. Their treatment does not, however, consider the laser's dynamical properties.

The models presented in Ref. [75] and Ref. [111] are both equivalent to the dressed-state two-photon laser model presented by Zakrzewski *et al.* [115], which is further described in Sec. 6.2.3. This proves both convenient and useful, as the dressed-state treatment models the experimental situation used in the only realization of the two-photon laser to date.

## 6.2 Experimental Progress

Despite the wealth of literature, it should have become clear that there are various two-photon laser models which lead to contradictory predictions and confusions, and yet still leave large gaps in our knowledge. Perhaps the most straightforward way to resolve these confusions and contradictions is through experimental investigations on two-photon stimulated emission and gain, and the experimental realization of a two-photon laser. A few of the more important experimental papers in this quest are mentioned below.

#### 6.2.1 Early Experimental Work

Early experiments focused on observation of two-quantum effects, including two-photon ionization, absorption, enhanced emission, and stimulated emission. In 1966, Hall observed what appeared to be one of the first genuine two-photon ionization signals. He calculated the two-quantum photoionization rate for atomic cesium, and observed ionization both when the laser was tuned to the two-photon resonance and when it was off-resonance. Two years later, Yatsiv et al. [116] observed enhanced two-photon emission between the 6S and 4S states of potassium atoms. Enhanced emission amplifies incident laser radiation without requiring inversion between the populations of the emitting atomic states, and serves as a precursor to true stimulated two-photon emission. Only two years later, Bräunlich and Lambropoulos [117] report on the observation of singly stimulated two-photon emission from metastable deuterium atoms. Due to an absence of real intermediate states, the de-excitation occurs via an unambiguously two-photon process.

Bethune, Lankard, and Sorokin [118] study two-photon emission crosssections for the metastable  $c^3\Pi_u \to b^3\Sigma_u^+$  transition in  $H_2$ . Despite extremely small cross-sections for emission, they believe these difficulties can be overcome, and molecular hydrogen presents a good candidate for a two-photon amplifier. Loy [119] reports an early experimental observation of adiabatic population inversion in a two-photon transition, demonstrated through two-photon stimulated emission and gain in ammonia. Although the two-photon gain is quite small and only a transient effect, this represents one of the first reports of two-photon stimulated emission and gain, and is a step forward in the quest to achieve two-photon laser oscillation. Gao [120] et al. look at two-photon stimulated emission between two excited states of the same parity in sodium. Sodium appears a better gain medium than ammonia due to the relatively higher energy storage in the excited sodium. Schlemmer, Frolich, and Welling [121] direct their interests toward finding continuous-wave two-photon gain since two-photon transient gain has been achieved. They observe stimulated two-photon emission in an incoherently pumped continuous-wave three-level cascade He-Ne laser. Qualitative agreement between the experimental results and a three-level rate-equation model is found.

Nikolaus [42] et al. report the observation of two-photon emission in atomic lithium vapor pumped by two counterpropagating laser beams, and apparent two-photon gain in a third beam probing the transition. There is some controversy [122], however, that competing nonlinear effects such as multiwave mixing are the origin of the observed enhancement. This sets a precedent forcing experimental papers to carefully distinguish between true two-photon type gain and wave-mixing type gain in some way (e.g. by using phase matching constraints to preventing wave mixing, or by ensuring the existence of a two-photon population inversion).

Though most investigations of two-photon gain concentrate on atomic media and optical pumping, Ironside [123] proposes semiconductors as a two-photon gain medium. Unfortunately, few (if any) experiments have been performed to test this new approach. Semiconductors have the advantages that two-photon effects are well understood and that semiconductor technology is a well-developed field, so material adaptation for our present purposes should not be difficult. A severe disadvantage, however, is that nonlinear processes which compete with two-photon gain are often prevalent in solid state media.

Normal one-photon lasing would completely overwhelm any two-photon lasing, and must be prevented for semiconductors to be a useful gain medium.

The work by Grynberg et al. [124] in which they report on a two-photon optically pumped laser also deserves mention. Some authors reference this as the first experimental observation of two-photon lasing. A careful reading, however, demonstrates that this is not the case. The system they discuss consists of a rubidium atom in which one creates a population inversion between two excited states by means of a two-photon excitation process. Normal, one-photon, laser emission is then possible between these two levels.

Bethune et al. [118] ascribe the limited success toward the realization of a two-photon amplifier to difficulties in finding a suitable transition (which has an intermediate state for enhancement, yet avoids cascade de-excitations through this state), troubles in creating significant population inversions between the transition levels, and the need for an extremely high intensity beam to trigger the two-photon emission. Although different materials and transitions have been studied in the quest to overcome these difficulties, significant success toward two-photon amplifiers and lasers is achieved only when two-photon emission is considered from an entirely different perspective.

#### 6.2.2 Two-Photon Micromaser

For many years experimental difficulties related to low two-photon gain in the usual transitions and competing nonlinear optical effects prevented the realization of a continuous-wave two-photon oscillator. In the mid-eighties, Haroche et al. [24, 125] realized that Rydberg atoms in a high-finesse superconducting cavity can be effectively used to overcome these difficulties and construct

a two-photon maser. Rydberg atoms, highly excited atoms with properties and radiation effects very different from atoms in low-lying states, are ideal for observing simple atom-cavity quantum dynamical effects [126]. They strongly couple to the radiation field owing to their large matrix elements for transitions to neighboring levels, and the transitions are in the region of millimeter waves, allowing construction of cavities with low-order modes that are reasonably large in order to insure long interaction times. The atoms also have long spontaneous emission times, so only the interaction with the selected cavity mode is important, and coupling of atoms to other cavity modes can be neglected.

Rydberg atoms' long wavelengths and large electric dipole moments make it possible to construct cavities that can oscillate with only one atom and a few microwave photons inside it at any time. The extremely low intracavity intensities tend to prevent destructive nonlinear effects from dominating the interaction. Rydberg atoms can also greatly enhance the two-photon transition amplitude if one chooses a two-photon transition such that an intermediate level can be found in the Rydberg state spectrum nearly halfway between the initial and final states. Using an extremely high finesse cavity serves to prevent unwanted resonance effects from occurring even when tuned very near the intermediate state. These ideas are successfully used in the first quantum oscillator based upon two-photon stimulated emission of radiation – the twophoton micromaser [25]. The micromaser displays sustained continuous-wave oscillation in a high finesse ( $\simeq 10^8$ ) niobium superconducting cavity on the degenerate  $40S \rightarrow 39S$  two-photon transition in rubidium. This extraordinary experimental accomplishment is a breakthrough in the quest for novel light sources, and shows promise for the eventual realization of a two-photon laser.

#### 6.2.3 Dressed-State Lasers

As mentioned earlier, the greatest experimental problem in building a two-photon oscillator is the small two-photon gain in most normal systems. The two-photon micromaser overcame this difficulty by using Rydberg atoms with an intermediate state to enhance the gain without increasing the effects of competing processes. Although this worked splendidly, the technique cannot be expanded into the optical regime. The breakthrough for the realization of a two-photon optical quantum oscillator required an innovative two-photon gain medium with similar idealized properties – a driven-atom gain medium. The new concept for optical two-photon gain is based on the idea that it is possible to 'engineer' a near-ideal two-photon gain medium consisting of two-level atoms (one-photon transition) driven by an intense, near-resonant laser field — a so-called dressed atom [17].

Over twenty years ago it was predicted [127] and later observed [128] that the spectrum of the radiation scattered by a two-level atom driven by an intense, resonant, monochromatic laser field displays three peaks (Mollow triplet). Soon after the first experimental observation of strong-field resonance fluorescence, Cohen-Tannoudji and coworkers [129] introduced the dressed-atom states to explain this triplet. The dressed-atom states are simply the energy eigenstates of the combined atom and strong driving field, derived by ignoring the interaction between the two-level atoms and all radiation modes except the single, highly-occupied mode of the driving field. In the dressed-atom representation, each peak of the Mollow triplet is then interpreted as arising from spontaneous emission events between the various dressed-atom states.

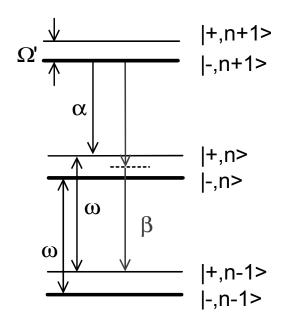


Figure 6.3: Standard dressed-states for a two-level atom driven at the frequency  $\omega$ 

Dressed-atom representation is quite useful in describing the interaction of intense laser fields with matter because it accurately describes the coupling of the atom to the field, which occurs in such a way that the energy-level and resonance structure of the atom is modified due to the laser-field induced Stark shifts. The standard dressed-state energy levels are described by an infinite ladder of doublets split by the generalized Rabi frequency  $\Omega'$  and separated by the laser frequency  $\omega$  as shown in Fig. 6.3. A nonzero detuning of the driving field from the atomic transition frequency results in a population imbalance between the dressed-state doublets. In particular, for the case of red detuning the lower levels of each doublet have larger populations. For transitions  $\alpha$  and  $\beta$  between dressed levels indicated in Fig. 6.3, this imbalance is then equivalent to a population inversion and optical gain can occur. Transition  $\alpha$  illustrates

an inverted one-photon transition at a frequency  $\omega_L = \omega - \Omega'$ . Laser pumped two-level atoms thus comprise a composite gain medium in which the gain is essentially identical to the familiar one-photon gain. Several researchers have successfully utilized this similarity and constructed one-photon lasers using dressed atoms [130].

Dressed-state gain is not limited to single photon transitions; in fact, an intense probe beam can induce multiphoton transitions among the dressed levels. Dressed-state atoms provide a near ideal two-photon gain medium in which the two-photon resonances are strongly enhanced by the intermediate dressed states, as illustrated by transition  $\beta$  in Fig. 6.3. Transition  $\beta$  illustrates an inverted two-photon transition at frequency  $\omega_L = \omega - \Omega'/2$ . The energy levels and splittings (and hence the resonance frequencies) are also, to some extent, tunable. Lewenstein, Zhu and Mossberg [131] predict that a collection of atoms strongly driven by a laser field displays two-photon gain and can support twophoton lasing. They describe the origin of gain in terms of inverted two-photon transitions between dressed atomic states. Zhu et al. [17] then experimentally observe a two-photon gain feature in the strong-probe absorption spectrum of a driven two-level atom. Zakrzewski, Lewenstein, and Mossberg [115] perform a careful theory of dressed-state lasers in which they derive stability conditions and determine laser threshold conditions which should be experimentally verifiable. They examine the quantum-statistical properties of both one-photon and two-photon dressed-state lasers, and the consequences of pump depletion on both the stability properties and statistical properties of the lasers. A further analysis by Lewenstein et al. [132] extends the theory to the bad-cavity limit, accounting for competition between one-photon and two-photon processes, and

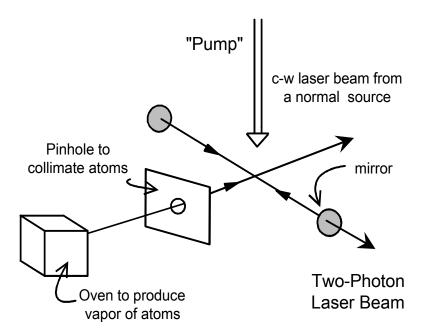


Figure 6.4: Schematic representation of the two-photon dressed-state laser show that high-order instabilities and chaos might appear.

Gauthier, Wu, Morin, and Mossberg [18] report the first realization of a continuous-wave two-photon optical laser. They use dressed-atom energy eigenstates as their two-photon gain medium, guaranteeing relatively strong, near resonantly enhanced, degenerate two-photon transitions. The two-photon laser consists of an atomic beam of barium atoms driven by another laser beam as it passes through the center of a confocal cavity, as shown in Fig. 6.4. They isolate the laser gain from competing one-photon processes using a high-finesse optical cavity. The mutually orthogonal geometry of the laser beams both prevents wave-mixing type processes from being phase matched for emission into the cavity modes and provides nearly Doppler-free atom-pump and atom-cavity interactions. They carefully characterize the dressed-atom laser system

and observe a pronounced, intensity-dependent gain feature at the predicted location for two-photon gain. Using an externally injected trigger-pulse, they initiate two-photon lasing and find the experimental threshold conditions to be in good agreement with theoretical predictions. Over twenty-five years after the two-photon laser was first theoretically described, Gauthier *et al.* conclusively demonstrated two-photon optical lasing! Like the two-photon maser, realization of the two-photon laser is an impressive experimental breakthrough, but it is by no means the end of the story.

#### 6.2.4 Raman Lasers

Despite the successes in realizing the two-photon maser and the dressed-state two-photon laser, a great deal of further work needs to be done in the detailed study of the properties of continuous-wave two-photon optical lasers. Masers, by definition, operate at microwave frequencies and hence have properties quite different from lasers, which operate at optical frequencies. Their long wavelengths and low photon energies mean that the particle-like nature of the light output from a two-photon maser is very difficult to measure. Unlike the optical regime where individual photons give a measurable detector response, in the microwave regime thousands or millions of photons are needed to produce the same response. This makes any study of the photon statistics or cavity photon numbers a difficult, though not insurmountable, proposition. These difficulties limit any benefits that studies of the two-photon micromaser can offer in terms of studying a two-photon laser.

The small gain observed in the two-photon dressed-state laser ( $\sim 0.1\%$ ), and the fact that the experimental apparatus worked near its theoretical limits,

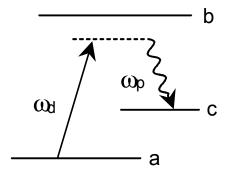


Figure 6.5: Raman scattering as a mechansim for gain

restricts its usefulness for careful, long-term studies of its properties. As a result, the main research directions in our lab are: (i) to thoroughly characterize two-photon lasers; and (ii) to develop new types of two-photon gain media, both in order to make two-photon lasing easier and in order to distinguish between the properties two-photon lasers in general and those that are specific to a gain medium. Guided by the concept underlying dressed-state two-photon lasers, we have discovered a new type of two-photon gain medium in which the gain is derived from two-photon, near-resonant Raman scattering between bare atom states of a multi-level atom.

Typical Raman gain arises from near-resonant scattering of laser photons from a three-level atom as shown in Fig. 6.5. This process amplifies the radiation at the frequency  $\omega$  if state  $|c\rangle$  is more populated than state  $|a\rangle$ . In a 1985 experiment unrelated to Raman gain, Kumar and Shapiro [34] observe unexpected laser oscillation in the sodium D lines when pumped by a continuous-wave dye laser and placed in an optical cavity. The oscillation is detuned from the pump laser by the ground state hyperfine splitting of sodium. After some study, they conclude that gain results from optical pumping and

stimulated Raman scattering. This is the first demonstration of the Raman laser.

Raman lasers have since become relatively standard laboratory tools, and are even used as pump lasers in a variety of nonlinear optical experiments. However, no attempt (to our knowledge) has been made to build Raman lasers based upon hyper-Raman processes. At high intensities, new features appear in the absorption spectrum of a Raman-active medium at subharmonics of the Raman difference frequency [133]. The fact that these are high-order gain features was not fully appreciated until recently – the early studies called them simply 'subharmonic resonances'.

Very recently Hänsch et al. [134] observed unique resonances in the absorption spectra of three-dimensional optical lattices which they attribute to multiphoton Raman transitions between vibrational states of the trapped atoms. Although the gain is small and not well resolved, this is to our knowledge the first published work explicitly identifying amplification due to what we call two-photon stimulated Raman scattering. Two-photon Raman scattering involves two photons from the pump laser and two from the probe laser in making the transition from the initial vibrational state to the final state via a virtual state. The basis of this thesis is the observation of very large gain attributed to a similar effect – two-photon stimulated Raman scattering in a strongly driven potassium vapor. Future work intends to use this gain to build the first two-photon Raman laser.

# Chapter 7

# Rate-equation model of two-photon lasers

To date, our efforts in the laboratory have focused on constructing an effective two-photon amplifier. Future work will concentrate on construction of a two-photon laser. Two-photon lasers are predicted to have a number of novel characteristics that interest researchers and deserve further study. Yet modelling the behavior of such lasers is challenging, mainly because they are based on the two-photon stimulated emission (SE) process and hence operate in a highly nonlinear manner under all conditions. Like the semiclassical two-photon amplifier theory described in Chapter 5, a laser theory would need to incorporate all of the amplifier effects, in addition to oscillator effects such as cavity-atom interactions and cavity losses. The propagation effects neglected in Chapter 5 also become a critical component in a description of an oscillator.

Theories of two-photon lasers have been developed in the past, but as we discovered in the last chapter most of the theories are mathematically quite complicated, often to the point that they begin to lose sight of the physical properties and laser dynamics that the equations themselves describe. We have

developed [65] a model for two-photon lasers based on a set of self-consistent rate-equations that predicts many of their crucial attributes without being overly complex. In this chapter, we present our rate-equation model and use it to make predictions of the behavior of two-photon optical lasers. We feel that our model is useful for developing an intuitive understanding of two-photon lasers, although more complete treatments which include interactions ignored in our rate-equation model, such as coherent effects [7, 105], single photon processes [9], and dynamical Stark shifts [135], may be needed to make quantitative comparisons with experimental results.

## 7.1 One-photon rate equations

Rate-equations provide the standard textbook approach to continuous-wave and transient behavior [136] for one-photon lasers. To our knowledge, however, this work is the first that uses them to model two-photon laser behavior. In the rate-equation approximation, laser equations are derived based on the idea that there is a balance between the rate of change of total population in the atomic system and the total number of laser photons. This is schematically indicated in Fig. 7.1, where levels a and b represent atomic energy levels and the black dots represent the populations in those levels. If an atom de-excites through a transition from level b to level a, the energy difference is balanced through the emission of a laser photon. Similarly, the absorption of a laser photon will transfer a single atom from level a to level b.

The main approximation in the rate-equation formulation stems from ignoring coherent effects. This approximation is valid only when the energy relaxation time  $1/\gamma$  and cavity decay time  $1/\gamma_c$  are long compared to the dephasing

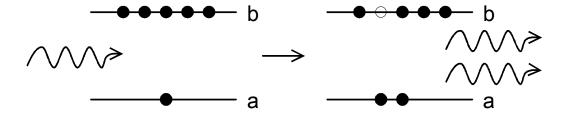


Figure 7.1: Energy balance between atomic inversion and field photons

time of the system, which turns out to be true for most laser transitions. When coherent effects are ignored, the dynamical equation for the coherences present in a full laser treatment can be adiabatically eliminated<sup>1</sup>, significantly simplifying the laser model. A further approximation in the rate-equation treatment is that they generally do not account for propagation effects, and so do not consider the possibility that photons created in one part of a gain medium can stimulate more transitions further downstream. Before discussing the details of our rate-equation model of two-photon lasers, it seems useful to provide a context with which to compare the basic laser equations and predicted behavior. Toward that end, we briefly summarize some of the well known results that stem from a rate-equation model of one-photon amplifiers and lasers.

## 7.1.1 Amplifier model

In an amplifier, no cavity is present and hence no cavity or oscillation effects need to be taken into account. For consistency with rate-equation models which ignore propagation effects, we study amplification in an optically thin medium where propagation effects are negligible. The amplifier is modelled as

<sup>&</sup>lt;sup>1</sup>Adiabatic elimination involves eliminating the atomic variables from the equation of motion for the field when (as in many laser systems) the state of the laser field varies little over the interaction time with the atom.

a thin slab of gain medium (a collection of two-level atoms with an external pump process creating an inversion) with some number of photons q incident upon it as shown in Fig. 7.2a. By the assumption of an optically thin medium, the photon number q remains constant throughout the amplifier, so we only need to explore how the population inversion density between the two active levels changes in time. This is modelled by the equation

$$\frac{d\Delta N}{dt} = -2B^{(1)}q\Delta N - \gamma(\Delta N - \Delta N_o) , \qquad (7.1)$$

where  $B^{(1)}$  is the one-photon rate coefficient,  $B^{(1)}q$  is the one-photon stimulated emission rate,  $\gamma$  is the population decay rate,  $\Delta N_o$  is the inversion in the absence of the field due to the pump process, and  $\gamma \Delta N_o$  is the pump rate. Physically the terms in this equation account for, respectively, a decrease in the inversion due to stimulated emission and spontaneous emission, and an increase due to pumping. These processes are schematically indicated in Fig. 7.2b.

For an amplifier, the steady-state response of the medium is found as the time-independent inversion, yielding

$$\Delta N_{ss} = \frac{\Delta N_o}{1 + 2B^{(1)}q/\gamma} = \frac{\Delta N_o}{1 + q/q_{cot}^{(1)}} , \qquad (7.2)$$

where we have defined the one-photon saturation photon number

$$q_{sat}^{(1)} \equiv \frac{\gamma}{2B^{(1)}} \ . \tag{7.3}$$

The one-photon saturation photon number is generally quite large<sup>2</sup>. The steady-state inversion in the one-photon amplifier given by Eq. 7.2 can also be

 $<sup>^2 \</sup>text{For a typical HeNe laser, we can estimate } q_{sat}^{(1)}$  as follows:  $q_{sat}^{(1)} = \gamma/2B^{(1)} = V_c\gamma/\sigma c$ , where  $V_c$  is the volume contained in the laser cavity ( $\sim 1~\text{mm}^2 \times 10~\text{cm}$ ),  $\gamma$  is the spontaneous decay rate ( $\sim 1/(10^{-4}~\text{sec})$ ),  $\sigma$  is the transition cross-section ( $\sim 10^{-18}~\text{cm}^2$ ), and c is the speed of light. With these numbers, we find  $q_{sat}^{(1)} \sim 10^{10}$ .

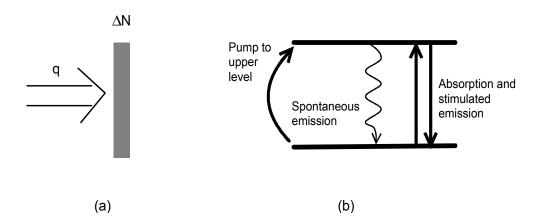


Figure 7.2: Generalized amplifier model showing relevant population-changing processes

quite large, and is only limited by the efficiency with which the pump can create an inversion  $\Delta N_o$ . The inversion will decrease as more and more photons are pumped into the medium and the medium saturates, where saturation represents a statement of energy conservation, indicating the finite pump energy and pump rate in any real system.

## 7.1.2 One-photon laser

Unlike an optical amplifier whose output results from single pass amplification of a light beam, a laser's output is light resulting from multiple passes through an amplifying medium. In a laser oscillator, the photon number present in the cavity can then change dramatically with time. The simplest possible rate-equation model for *laser* transients (in either a one- or two-photon laser model) then consists of a single first order differential equation for the population difference between lasing levels coupled to a single first order differential equation for the intensity or photon density. This is sufficiently accurate for

most practical purposes, and yet the equations remain intuitive enough that they are easily adapted to different laser systems. These laser models extend the description of an amplifier in order to also account for the change in the photon number q.

The basic form of the one-photon rate-equations couples  $\Delta N$ , the population inversion density between the two active levels, to the photon number q according to the nonlinear system of equations [137]

$$\frac{dq}{dt} = V_a B^{(1)}(q+1)\Delta N - \gamma_c q \tag{7.4}$$

and

$$\frac{d\Delta N}{dt} = -2B^{(1)}q\Delta N - \gamma(\Delta N - \Delta N_o) . (7.5)$$

Here  $V_a$  is the volume of the gain medium within the cavity mode and  $\gamma_c$  is the cavity decay rate. Equation 7.4 explicitly includes the effect of spontaneous emission. In a single mode cavity, approximately one photon exists at all times due to spontaneous emission. The net emission rate into the cavity is then proportional to the number of cavity photons plus one (q+1). In order to keep the algebra simple and the solutions intuitive, we find approximate steady-state solutions both in the regime at low pump rates where  $q \ll 1$  and at higher pump rates where  $q \gg 1$ . The limiting solutions must be consistent with each other in the intermediate regime.

In any laser, a minimal requirement to initiate lasing forces the material gain to equal the system loss. If the gain is large enough, a single spontaneously emitted photon will multiply until the cavity photon number is large enough to support lasing. One analytic indicator of lasing is given by the photon number increasing with time, so that dq/dt > 0. Equation 7.4 applied to the case where the photon number is large  $(q + 1 \simeq q)$  requires  $\Delta N > \gamma_c/V_a B^{(1)}$ , so that laser action is produced when the population inversion reaches a critical value given by

$$\Delta N_{crit} = \frac{\gamma_c}{V_a B^{(1)}} \ . \tag{7.6}$$

When the pump rate (producing the inversion) is above the threshold value, the photon number q grows from an initial value determined by spontaneous emission and, for a constant pump, will eventually reach a constant value  $q_{ss}$ . This steady-state value, and the corresponding steady-state value for the inversion  $\Delta N_{ss}$  can be found by setting the time rate of change of the photon number and the inversion equal to zero. Solving laser equations in steady-state in this manner greatly simplifies the mathematics of the problem by reducing the set of coupled differential equations to algebraic equations. The algebraic equations can then be analytically or numerically solved for allowed photon numbers and inversions as a function of the pumping in a very straightforward manner.

#### Spontaneous regime

At low pump-rates where  $q \ll 1$ , the spontaneously emitted photon plays a critical role and, in fact, starts the transition to lasing. Equation 7.4 with  $(q+1) \simeq 1$  gives

$$q = \frac{V_a B^{(1)}}{\gamma_c} \Delta N = \frac{\Delta N}{\Delta N_{crit}} \ll 1 , \qquad (7.7)$$

while Eq. 7.5 reduces to

$$\frac{\Delta N^2}{q_{sat}\Delta N_{crit}} + \Delta N - \Delta N_o = 0 . {(7.8)}$$

However, since  $\Delta N/\Delta N_{crit} \ll 1$  at low pump rates and  $q_{sat}$  is typically large, the first term in the above equation can be neglected to give

$$\Delta N \simeq \Delta N_o \tag{7.9}$$

and, from Eq. 7.7,

$$q \simeq \frac{\Delta N_o}{\Delta N_{crit}} \ . \tag{7.10}$$

#### Stimulated regime

To solve the steady-state rate-equations in the regime where stimulated emission is important  $(q \gg 1)$  we take  $(q+1) \simeq q$  in Eq. 7.4. There are then two possible solutions to this equation,

$$q_{ss} = 0 (7.11)$$

and

$$\Delta N_{ss} = \frac{\gamma_c}{V_a B^{(1)}} = \Delta N_{crit} . \tag{7.12}$$

Only the second solution can continuously match the solution in the spontaneous regime where the steady-state photon number is greater than zero, so Eq. 7.12 describes the system. The steady-state photon number above threshold is then determined from Eqs. 7.3, 7.5 and 7.12 to be

$$q_{ss} = q_{sat} \left( \frac{\Delta N_o}{\Delta N_{crit}} - 1 \right) . {(7.13)}$$

The general behavior of the photon number and the inversion density in the one-photon laser are sketched<sup>3</sup> in Fig. 7.3. The one-photon rate-equations predict that above a certain pump level (which produces the threshold inversion)

<sup>&</sup>lt;sup>3</sup>Although we have not explicitly shown it here, the approximate solutions found in the different regimes must connect continuously in the intermediate region.

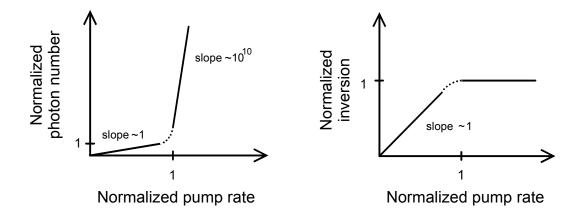


Figure 7.3: Approximate steady-state behavior of the photon number and the inversion above and below the one-photon laser threshold

the laser begins to operate, as evidenced by the growth of the photon number q from a very small initial value. This turn-on process occurs extremely rapidly, yet smoothly. An important feature of the solution given by Eq. 7.12 and illustrated in Fig. 7.3b is that the inversion is *clamped* above threshold at the critical value. Any increase in the pump rate above the critical value of the threshold pump rate produces an increase in the number of photons in the laser cavity, and not an increase in the inversion.

## 7.2 Two-photon rate-equations

After briefly summarizing both the procedure and the results derived from a rate-equation model of one-photon amplifiers and lasers, the analysis can now be extended to describe two-photon amplifiers and lasers. In order to model two-photon transitions, we modify Eqs. 7.1, 7.4, and 7.5 by replacing the one-photon stimulated emission rate  $B^{(1)}q$  with the two-photon stimulated emission rate  $B^{(2)}q^2$  [138]. This new rate coefficient derives from a direct evaluation of

the two-photon transition probability [139].

## 7.2.1 Two-photon amplifier model

For purposes of comparison, first consider the simple case of an amplifier based upon a two-photon gain medium. The inversion equation for the two-photon amplifier (again under the approximation of an optically thin gain medium) then looks quite similar to that for the one-photon laser, and reads

$$\frac{d\Delta N}{dt} = -2B^{(2)}q^2\Delta N - \gamma(\Delta N - \Delta N_o). \qquad (7.14)$$

Solving in steady state gives

$$\Delta N_{ss} = \frac{\Delta N_o}{1 + 2B^{(2)}q^2/\gamma} = \frac{\Delta N_o}{1 + q^2/q_{sat}^2}, \qquad (7.15)$$

where the inversion is now explicitly labelled as a steady state quantity. Note that  $q_{sat} = \sqrt{\gamma/2B^{(2)}}$  is defined as the two-photon saturation photon number, in analogy with the standard one-photon saturation number. The saturation number is simply a collection of constants whose value depends only on the parameters of the transition and indicates when a stimulating wave is strong or weak. A strong incident wave will significantly affect the population distribution due to stimulated emission, while a weak wave has a negligible effect. The two-photon saturation photon number is defined to occur when the two-photon stimulated emission rate is equal to half the population decay rate. Its physical meaning is then obvious: for  $q_{ss} = q_{sat}$ , the steady-state inversion is equal to one-half of the inversion created by the pump process in the absence of a field,  $\Delta N_{ss} = N_o/2$ .

Equation 7.15 is reminiscent of the steady-state inversion for a one-photon amplifier (Eq. 7.2) except that the denominator is now quadratic, rather than

linear, in q. The inversion again increases with the pump rate, and is limited only by the efficiency of the pumping scheme. The seemingly innocuous quadratic term, however, serves to significantly modify the steady-state solutions for a two-photon laser from those of a one-photon laser, as we will see below.

## 7.2.2 Two-photon laser model

A description of a two-photon laser is found by extending the description of a two-photon amplifier to include cavity effects. For simplicity, assume that the two-photon laser operates in the degenerate mode, that the laser oscillates in a single plane-wave mode, and that the cavity (population) decay rate  $\gamma_c$  ( $\gamma$ ) is much smaller than the atomic coherence dephasing rate. Under these oversimplifying conditions, the behavior of the laser is described by the mean photon number in the cavity q and the mean population inversion density  $\Delta N$  between the atomic levels that participate in the stimulated emission process. The first-order, coupled nonlinear differential equations governing the evolution of these quantities are given by

$$\frac{dq}{dt} = V_a B^{(2)} q^2 \Delta N - \gamma_c (q - q_{inj}(t))$$

$$(7.16)$$

and

$$\frac{d\Delta N}{dt} = -2B^{(2)}q^2\Delta N - \gamma(\Delta N - \Delta N_o), \qquad (7.17)$$

where  $q_{inj}(t)$  is the photon number injected into the cavity by an external source.

The forte of rate-equations lies in the obvious physical interpretations of their terms. Equation 7.16 indicates that the photon number increases due to the two-photon stimulated emission process and by injection from the external source, and decreases due to linear loss through the cavity mirrors. This ignores the possibility of two-photon spontaneous emission processes at the laser frequency because the emission rates are extremely small in the optical regime [74]. This approximation is not valid for two-photon masers where the stimulated and spontaneous rates are comparable [24]. Similarly, Eq. 7.17 states that the inversion decreases in response to the stimulated emission process and due to other radiative (at frequencies distinct from the laser frequency) and nonradiative decay mechanisms, and increases due to the pump process.

The remainder of this chapter is devoted to a study of Eqs. 7.16 and 7.17. From them we find the steady-state behavior of the laser and explore the laser's stability properties. We also directly integrate the equations under various conditions in order to explore the transient behavior of the laser.

## 7.3 Derivation of the steady-state behavior

Under steady-state conditions, we find from Eq. 7.17 that

$$\Delta N_{ss} = \frac{\Delta N_o}{1 + 2B^{(2)}q_{ss}^2/\gamma} = \frac{\Delta N_o}{1 + q_{ss}^2/q_{sat}^2} \,. \tag{7.18}$$

This is identical to the solution found for the two-photon amplifier with  $q \to q_{ss}$ . The solution is not complete, however, because the equations for the inversion and the photon number remain coupled. The inversion can be found explicitly by first substituting Eq. 7.18 into Eq. 7.16 to solve for the photon number (in terms of the pump rate  $\Delta N_o$ ). For clarity, we explore the situation separately for the case when the injected field  $q_{inj}$  is zero and when it is non-zero.

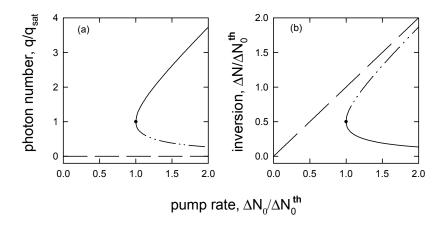


Figure 7.4: Steady-state behavior of the cavity photon number and atomic inversion with no injected field

# 7.3.1 Steady-state equations for $q_{inj} = 0$

For the case when  $q_{inj}(t) = 0$ , there are three solutions to Eq. 7.16 given by

$$q_{ss}^o = 0 (7.19)$$

and

$$q_{ss}^{\pm} = \frac{\gamma V_a}{4\gamma_c} \left[ \Delta N_o \pm \sqrt{\Delta N_o^2 - 16q_{sat}^2 \gamma_c^2 / \gamma^2 V_a^2} \right] . \tag{7.20}$$

The steady-state solutions are only physically meaningful when they are non-negative real numbers. The physical solutions are plotted as a function of the pump rate in Fig. 7.4. It is seen from Eq. 7.20 that  $\Delta N_o^{th} = 4q_{sat}\gamma_c/\gamma V_a$  is the minimum value of  $\Delta N_o$  which admits a nonzero photon number, and hence represents the threshold inversion. With this threshold inversion, the onset of lasing occurs at the steady-state values  $q_{ss}^{\pm} = q_{sat}$  and  $\Delta N_{ss} = 1/2 \Delta N_o^{th}$ .

This is in agreement with the heuristic discussion of the threshold behavior presented in the introduction.

There are a few basic behavioral similarities and differences between onephoton lasers and amplifiers and two-photon lasers and amplifiers. The discontinuous threshold behavior shown in Fig. 7.4 is indicative of a first-order phase transition, which is very different from the smooth turn-on behavior of normal one-photon lasers. Figure 7.4a demonstrates that the two-photon gain is saturated at threshold, again in sharp contrast to the typical one-photon laser which operates very far below saturation. Finally, recall that in the one-photon amplifier the inversion increased linearly with the pump rate. In a one-photon laser, adding a cavity dramatically affected the behavior and led to inversion clamping in which the inversion remains constant at its threshold value even for high pump rates. In a two-photon amplifier, the inversion again increases with pump rate, and, by analogy one might expect inversion clamping above threshold. In a two-photon laser, however, the inversion does not clamp above threshold. Figure 7.4b shows that the inversion is never constant, and is a strong indication that a two-photon laser may display behavior dramatically different from that of a one-photon laser.

<sup>&</sup>lt;sup>4</sup>It is interesting to note that many early two-photon laser models predicted inversion clamping very similar to that seen in the one-photon laser. These predictions resulted from a restrictive 'detailed balance' assumption for cavity losses, where mirror losses were taken to be nonlinear and required two photons to escape the cavity at the same time. Such a restriction proves unphysical and leads to incorrect results. For purposes of comparision with these early models, however, we can mimic detailed balance in our model by modifying Eq. 7.16 to read  $\gamma_c q \to \gamma_c q^2$ , so that the cavity decay scales as the square of the photon number. Our model then predicts inversion clamping.

#### 7.3.2 Dimensionless equations

The saturation and threshold parameters introduced earlier serve to define the natural scales for the parameters of the system. We translate the equations to dimensionless units defined in terms of these natural units in order to look more easily at the steady-states and stabilities of the solutions. Dimensionless variables are indicated by tildes, and are found as follows. Photon numbers are divided by the saturation photon number, giving

$$\tilde{q}_{ss} \equiv \frac{q_{ss}}{q_{sat}} \text{ and } \tilde{q}_{inj} \equiv \frac{q_{inj}}{q_{sat}};$$
 (7.21)

inversions are normalized to the threshold inversion, yielding

$$\Delta \tilde{N}_{ss} \equiv \frac{\Delta N_{ss}}{\Delta N_o^{th}} \text{ and } \Delta \tilde{N}_o \equiv \frac{\Delta N_o}{\Delta N_o^{th}};$$
 (7.22)

and rates/times are normalized to the cavity decay rate, giving

$$\tilde{\gamma} \equiv \frac{\gamma}{\gamma_c} \text{ and } \tilde{t} \equiv \frac{t}{t_c} = t\gamma_c.$$
 (7.23)

With these definitions, the rate-equations (Eqs. 7.16 and 7.17) transform to

$$\frac{d\Delta\tilde{N}}{d\tilde{t}} = -\tilde{\gamma}\tilde{q}^2\Delta\tilde{N} - \tilde{\gamma}(\Delta\tilde{N} - \Delta\tilde{N}_o)$$
 (7.24)

and

$$\frac{d\tilde{q}}{d\tilde{t}} = 2\tilde{q}^2 \Delta \tilde{N} - \tilde{q} + \tilde{q}_{inj} . \tag{7.25}$$

The  $q_{inj} = 0$  steady-state solutions given by Eqs. 7.19 and 7.20 can then be rewritten as

$$\tilde{q}_{ss}^o = 0 \tag{7.26}$$

and

$$\tilde{q}_{ss}^{\pm} = \left[ \Delta \tilde{N}_o \pm \sqrt{\Delta \tilde{N}_o^2 - 1} \right] . \tag{7.27}$$

## 7.3.3 Steady-state equations for $\tilde{q}_{inj} \neq 0$

For  $\tilde{q}_{inj} \neq 0$ , it is difficult to algebraically solve for the steady-state laser behavior. Using the dimensionless variables, the steady-state inversion is

$$\Delta \tilde{N}_{ss} = \frac{\Delta \tilde{N}_o}{1 + \tilde{q}_{ss}^2} \tag{7.28}$$

as before. The steady-state photon number, however, is found from the cubic

$$0 = \tilde{q}_{ss}^3 - \tilde{q}_{ss}^2 (2\Delta \tilde{N}_o + \tilde{q}_{inj}) + \tilde{q}_{ss} - \tilde{q}_{inj} , \qquad (7.29)$$

which is not in general analytically solvable. It is known that a cubic with real coefficients will always yield either three real roots or one real root and a complex conjugate pair. From these roots, note that negative or imaginary values of the steady-state photon number are nonphysical. The task, then, is to numerically determine when  $\tilde{q}_{ss}$  yields a positive real root and hence a physically meaningful solution. These meaningful  $\tilde{q}_{ss}$  solutions are later used to perform a stability analysis of the solutions and determine the injection threshold.

In general, both the pump rate  $\Delta \tilde{N}_o$  and the injection parameter  $\tilde{q}_{inj}$  can vary in a laser system, and any changes in these parameters will affect the steady-state solutions. As a result, in an analysis of our system there are really two different, though related, questions to address concerning the expected laser behavior. First, how will the laser behave as the pump rate is varied given a constant injected field in the cavity? Second, what level of trigger pulse must be injected for the laser to turn on at any given pump rate? The next section responds to the first issue, while the second issue becomes more important in the transient regime and is addressed later in this chapter.

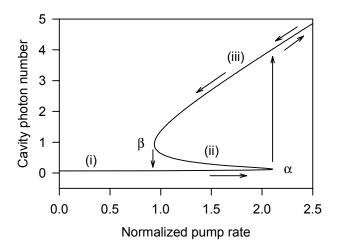


Figure 7.5: Steady-state behavior of the laser showing hysteresis

#### Laser behavior with constant injected field $\tilde{q}_{inj}$

We first describe some representative behavior found by assuming injection of a constant photon number of  $\tilde{q}_{inj} = 0.06$  into the cavity. Figure 7.5 illustrates that for small nonzero values of  $\tilde{q}_{inj}$ , the steady-state solution has the shape of a typical bistability curve with three distinct branches, labelled (i), (ii), and (iii). A laser in this regime exhibits hysteretic turn-on behavior. Suppose a constant photon number  $(\tilde{q}_{inj} = 0.06$  for the curve shown) is injected into the cavity while the pump rate is varied from an initial value of zero. The laser follows branch (i) until its turning point (labelled  $\alpha$ ), where branches (i) and (ii), which were previously distinct positive real solutions, merge and become a complex conjugate pair. The laser remains below the lasing threshold along this lowest branch.

Beyond the turning point, further increasing the pump rate causes the laser to discontinuously jump to branch (iii). The upper branch has a high-photon number and represents the lasing solution, and hence the turning point  $\alpha$  represents the laser turn-on threshold. With further increases in pump rate, the state of the laser moves out along the upper branch as indicated. If the pump rate is now decreased, the laser remains on the upper branch and continues lasing even when the pump rate is decreased below the turn-on threshold. If, however, the pump rate is lowered below the turning point between branches (ii) and (iii) (labelled  $\beta$ ), the laser is forced to jump back to the lowest branch (i). The turning point  $\beta$  represents the turn-off threshold. In the regime with three distinct branches, then, the laser threshold behavior displays distinct hysteresis as the pump rate is varied while a constant field is injected into the cavity. Additionally, the jump from branch (i) to branch (iii) on turn-on indicates a first-order, discontinuous phase transition.

We expand the analysis by looking at the solutions for a few selected values of a constant injected field  $\tilde{q}_{inj}$ . In Fig. 7.6, note the progression of the steady-state curves from a region in which there are three distinct branches to one in which there is only a single branch. At this point, no hysteresis is seen with changes in pump rate, but instead the laser turns on and off smoothly. Thus, if the system is driven with a large enough injected field ( $\tilde{q}_{inj} \geq 0.20$ ) it begins to show a characteristic similar to a one-photon laser: a continuous, single-valued steady-state solution. This continuous solution indicates a change in the threshold behavior from a first-order to a second-order phase transition. Unpublished work with the dressed-state two-photon laser indicated that a change in the phase-transition characterizing the system seems possible, though

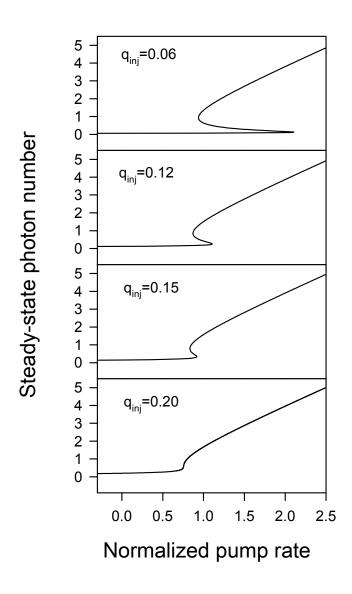


Figure 7.6: Steady-state behavior of the cavity photon number with a non-zero injected field  $\,$ 

requires more study to make a definitive assessment [140].

It is worth noting that the dimensionless steady-state equations for both  $\tilde{q}_{inj} = 0$  and  $\tilde{q}_{inj} \neq 0$  are independent of  $\tilde{\gamma}$  (the ratio between the atomic decay rate and cavity decay rate), and hence the solutions are valid over the entire range of cavity qualities. Cavity quality becomes important, however, in the following sections that consider the stability of the steady-state solutions.

## 7.4 Linear stability analysis

Interesting instabilities in typical one-photon lasers have been found both theoretically and experimentally, and as a general rule the instabilities change
with increasing pumping strength [141]. The onset of laser action is typically
the first instability. New instabilities occur at higher pumping strengths in
which either the intensity of the one lasing mode will start to oscillate or some
off-resonance modes will become unstable. The diverse and complex behavior exhibited by typical lasers proves interesting both to researchers concerned
with the general mathematical modelling of nonlinear systems, and to those
concerned with the practical behavior of the lasers. Based on past experience with one-photon lasers, it is expected that the steady-state equations for
two-photon lasers may also have interesting stability properties.

## 7.4.1 Linearization procedure

We investigate the stability of the stationary solutions using a typical linearization procedure, outlined below. Starting from Eqs. 7.24 and 7.25, perturb the system's dynamical variables around their respective steady-state values using the substitutions  $\tilde{q} \to \tilde{q}_{ss} + \delta q$  and  $\Delta \tilde{N} \to \Delta \tilde{N}_{ss} + \delta N$ . After performing this

substitution and retaining only terms first order in the small perturbations  $\delta q$  and  $\delta N$ , this yields the linearized equations of motion,

$$\frac{d(\delta q)}{d\tilde{t}} = 2\tilde{q}_{ss}^2 \delta N + 4\tilde{q}_{ss} \Delta \tilde{N}_{ss} \delta q - \delta q \tag{7.30}$$

and

$$\frac{d\delta N}{d\tilde{t}} = -\tilde{\gamma}(\tilde{q}_{ss}^2 \delta N + 2\tilde{q}_{ss} \Delta \tilde{N}_{ss} \delta q + \delta N) . \tag{7.31}$$

We solve these coupled equations for the eigenvalues of the system, because the eigenvalues describe the response of the steady-state solutions to small perturbations. If an applied perturbation decays away and the system returns to the original solution, then that solution is said to be stable. If the perturbation grows, then the solution is unstable.

Stability directly relates to the signs of the eigenvalues. If the real parts of all the eigenvalues are negative, the steady-state of interest is stable and the corresponding solution represents a physical and accessible state for the system. If even one rate constant acquires a real positive value, the system is unstable and will depart exponentially from the steady-state in response to an applied perturbation. The signs of the real part of the eigenvalues thus determine the absolute stability of the system, even if the eigenvalues are complex numbers. Complex eigenvalues simply state that the growth or decay of any perturbations will be oscillatory. A pure imaginary eigenvalue corresponds to a periodic solution with fixed amplitude oscillations.

Considering the above system in terms of matrices leads to a second-order eigenvalue equation, where the eigenvalues (or rate constants)  $\lambda$  of the system are found as the nonzero solutions to the characteristic equation

$$\det \begin{bmatrix} 4\tilde{q}_{ss}\Delta\tilde{N}_{ss} - 1 - \lambda & 2\tilde{q}_{ss}^2 \\ -2\tilde{\gamma}\tilde{q}_{ss}\Delta\tilde{N}_{ss} & -\tilde{\gamma}(\tilde{q}_{ss}^2 + 1) - \lambda \end{bmatrix} = 0.$$
 (7.32)

When expanded, the above determinant is a second order polynomial in  $\lambda$ ,

$$\lambda^2 + \lambda B + C = 0 (7.33)$$

where

$$B = \tilde{\gamma}(\tilde{q}_{ss}^2 + 1) - 4\tilde{q}_{ss}\Delta\tilde{N}_{ss} + 1 \tag{7.34}$$

and

$$C = \tilde{\gamma}(\tilde{q}_{ss}^2 - 4\tilde{q}_{ss}\Delta\tilde{N}_{ss} + 1) . \tag{7.35}$$

The roots of this equation,  $\lambda = \frac{1}{2}(-B \pm \sqrt{B^2 - 4C})$ , give us the rate constants  $\lambda$ . Note that the determination of the eigenvalues  $\lambda$  first requires the computation of the steady-state values  $\tilde{q}_{ss}$  and  $\Delta \tilde{N}_{ss}$ . We separately calculate  $\tilde{q}_{ss}$  and  $\Delta \tilde{N}_{ss}$  for the case when the injected photon number is zero and when it is nonzero.

# 7.4.2 Linear stability analysis for $q_{inj} = 0$

For  $q_{inj} = 0$ , the dimensionless steady-state solutions are given by Eqs. 7.18, 7.26, and 7.27. We summarize the results of a linear stability analysis of these steady-state solutions below and explore the mathematical details in what follows.

- $\bullet$  The zero-photon solution  $(\tilde{q}^o_{ss},\Delta \tilde{N}^o_{ss})$  is always stable.
- The  $(\tilde{q}_{ss}^-, \Delta \tilde{N}_{ss}^-)$  solution, where the photon number decreases with increasing pump rate, is always unstable.
- The  $(\tilde{q}_{ss}^+, \Delta \tilde{N}_{ss}^+)$  solution, where the photon number increases with increasing pump rate, is always stable for a 'good' cavity  $(\gamma/\gamma_c > 1)$ .

• The  $(\tilde{q}_{ss}^+, \Delta \tilde{N}_{ss}^+)$  solution is unstable for a 'bad' cavity  $(\gamma/\gamma_c < 1)$  for pumping just above threshold but stabilizes for higher pump rates.

Note that the 'good' and 'bad' cavity conditions are a constraint on the cavity linewidth relative to the atomic decay rate, and should not be interpreted literally to mean that the cavity design must be of high or low optical quality.

The  $\tilde{q}_{ss}^{o}$  solution is trivially shown to be stable. Using  $\tilde{q}_{ss}^{o} = 0$ , the eigenvalue equation (Eq. 7.33) simplifies to

$$\lambda = -\frac{(\tilde{\gamma} + 1)}{2} \left[ 1 \pm \sqrt{\frac{\tilde{\gamma} - 1}{\tilde{\gamma} + 1}} \right] . \tag{7.36}$$

Since  $\tilde{\gamma} > 0$ , the term in brackets always has a positive real part, and multiplication by the negative leading term yields eigenvalues  $\lambda$  which necessarily have a negative real part, rendering this solution always stable. Two-photon spontaneous emission, neglected here, can destabilize this solution.

To check the stability of the other equations, simply substitute the steadystate values given by Eqs. 7.26 and 7.27 into the characteristic equation for  $\lambda$ . Evaluation of  $Re(\lambda)$  determines the stability properties of the steady-state solutions, since if  $Re(\lambda)$  has a positive real part the corresponding solution is unstable. The eigenvalues are numerically evaluated, because even though in principle the procedure is quite simple the algebra for this calculation becomes rather messy. The  $\tilde{q}_{ss}^-$  solution is unstable over the entire range of pump rates and cavity goodness. The laser will thus not have output intensities given by this solution.

The  $\tilde{q}_{ss}^+$  solution, on the other hand, is generally stable and represents the lasing output. Note that because the zero solution is also stable, some sort of trigger will be needed to make the transition from the zero solution (the

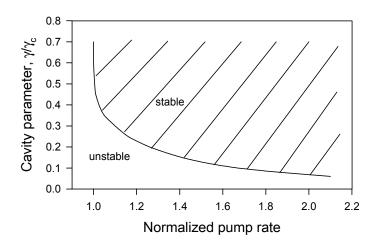


Figure 7.7: Stability boundary with no injected field

typical initial condition where the laser is 'off') to the non-zero output intensity solution. This is an indication that the two-photon laser is a bistable system, and as such may have application in terms of optical switching.

The  $\tilde{q}_{ss}^+$  solution is not, however, stable for all parameter values. In the very bad-cavity limit (for  $\tilde{\gamma} \lesssim 0.5$ ), there exists a small region just above the threshold pump rate where the solution is unstable, although the solution tends to stabilize at higher pump rates. The stability boundary is shown in Fig. 7.7. This result is inconsistent with the work of Ning *et al.* [105] and Heatley *et al.* [109] who found that there is no stable lasing state in the bad-cavity limit. We attribute the difference between results to our neglect of coherent effects based on the work of Ref. [105].

### 7.4.3 Linear stability analysis with $q_{inj} \neq 0$

The steady-state solutions of Eqs. 7.28 and 7.29 have already been determined. We now need to determine their stability properties when a continuous-wave beam of photons is injected into the cavity ( $\tilde{q}_{inj} \neq 0$ ). Using the same method just described for the simpler case with no injected field, we use the steady-state values and Eqs. 7.30 and 7.31 to perform a linear stability analysis. Although they yield the same characteristic equation for the eigenvalues  $\lambda$  as the zero-injection case, the solution involves different values of the steady-state inversion  $\Delta \tilde{N}_{ss}$  and photon number  $\tilde{q}_{ss}$ . As before, the eigenvalues for the linear stability analysis must be negative for a stable solution, and complex eigenvalues are perfectly valid.

Here we summarize the results of the linear stability analysis with  $q_{inj} \neq 0$ . A more careful discussion of the results is deferred to the next section, in which there is also a discussion of how an injected field can turn on the laser.

- The low-photon case, which used to be always stable, now abruptly destabilizes past a critical value (determined in the next section) which is a function of both the pump rate and the injected photon number.
- The mid-photon number case remains always unstable.
- The high-photon number case remains always stable in the good cavity limit, and again has regions of instability in the bad cavity limit. The instability boundary reproduces Fig. 7.7 in the limit  $\tilde{q}_{inj} = 0$ .

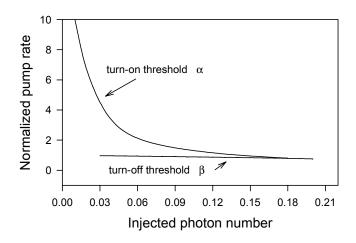


Figure 7.8: Turn-on and turn-off thresholds as a function of injection

### 7.5 Injection Threshold

A study of the laser's injection threshold allows a response to the question posed in Sec. 7.3.3 asking what amplitude trigger is necessary to turn on the laser for any given pump rate. In that section, the steady-state photon number as a function of pump rate was explored when some constant beam of photons was injected into the cavity. The laser displayed hysteresis, with discontinuous turn-on and turn-off thresholds that vary with the injection amplitude.

We now reverse the problem and explicitly look at the laser threshold with a variable injection and a fixed pump rate. Figure 7.8 maps how the turn-on and turn-off thresholds change with increasing injection. In relation to what has been done previously, Fig. 7.8 maps how the critical points  $\alpha$  and  $\beta$  (described in conjunction with Fig. 7.5) vary as the injected photon number

is varied. In the region above the turn-on threshold  $\alpha$  the laser is on; in the region below the turn-off threshold  $\beta$  the laser is off. In addition, recall from Fig. 7.6 that at an injection rate above about  $\tilde{q}_{inj} = 0.20$  the laser enters a regime of continuous and smooth turn-on behavior. This appears as the point where the two thresholds in Fig. 7.8 merge and end. A method for finding an analytical expression for the threshold values is described below.

If, in Fig. 7.6, the axes are reversed in order to consider photon number versus pump rate, the resulting curve is a function whose turning points are easily found as its local maxima and minima. Yet these turning points are exactly the critical points representing the turn-on and turn-off thresholds. We thus solve Eq. 7.29 for  $\Delta \tilde{N}_o$ ,

$$\Delta \tilde{N}_o = \frac{1}{2} \left[ \frac{\tilde{q}_{ss}^3 - \tilde{q}_{ss} - \tilde{q}_{inj}}{\tilde{q}_{ss}^2} - \tilde{q}_{inj} \right] , \qquad (7.37)$$

and take its derivative with respect to  $\tilde{q}_{ss}$ ,

$$\frac{d(\Delta \tilde{N}_o)}{d(\tilde{q}_{ss})} = \frac{1}{2} \left[ \frac{\tilde{q}_{ss}^4 - \tilde{q}_{ss}^2 + 2\tilde{q}_{ss}\tilde{q}_{inj}}{\tilde{q}_{ss}^4} \right] . \tag{7.38}$$

Setting the derivative equal to zero determines the critical points of the steadystate photon number. The equation  $d(\Delta \tilde{N}_o)/d(\tilde{q}_{ss}) = 0$  is satisfied for  $\tilde{q}_{ss} = \tilde{q}_{crit}$ , where  $\tilde{q}_{crit}$  is found from the cubic

$$\tilde{q}_{crit}^3 - \tilde{q}_{crit} + 2\tilde{q}_{inj} = 0$$
 (7.39)

Figure 7.8 was generated from a numerical solution to this equation.

A reasonably simple analytic approximation to the turn-on curve sometimes proves useful for performing back-of-the-envelope calculations. We arrive at such an approximation as follows. In the regime with three distinct branches for the steady-state photon number, note from Fig. 7.6 that  $\tilde{q}_{crit} < 1$ . As a lowest

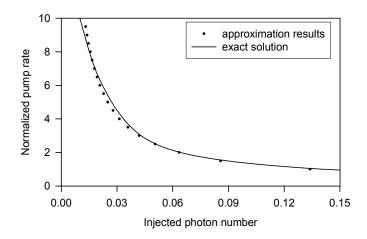


Figure 7.9: Comparison between exact and approximate expressions for the laser turn-on threshold

order approximation, neglect the cubic term in Eq. 7.39 to get  $(\tilde{q}_{crit})^0 \simeq 2\tilde{q}_{inj}$ . Then substitute this solution into Eq. 7.29 and solve for the critical injection strength at a given pump rate  $\Delta \tilde{N}_o$  to find

$$\tilde{q}_{inj} = \Delta \tilde{N}_o \pm \frac{1}{2} \sqrt{4\Delta \tilde{N}_o^2 - 1} \ . \tag{7.40}$$

The curve described by Eq. 7.40 well represents the exact critical injection strength, as shown in Fig. 7.9.

We earlier described the hysteretic behavior of the laser as the pump rate varied for a constant injected field. As one would expect, similar hysteresis is seen by exploring the laser behavior for a constant pump rate while the injection amplitude is varied. In this case, it proves easiest to simultaneously consider the steady-state solutions, a linear stability analysis of these solutions, and the injection threshold in order to arrive at a comprehensive description

of the laser behavior.

First recall the physically meaningful  $\tilde{q}_{ss}$  solutions plotted in Fig. 7.6. For low pumping rates, the only physical solution is that corresponding to the laser remaining off, in analogy to the  $\tilde{q}_{inj}=0$  solution  $\tilde{q}_{ss}^o$ . In this solution the photon number remains close to the injected photon number and has very little amplification due to spontaneous or stimulated emission. It is interesting to note, however, that due to the presence of injected photons into the cavity the threshold inversion is not equal to one, but rather  $\Delta N_o^{th}$  can be less than 1. (In other words, the critical point  $\beta$  occurs at a normalized pump rate less than 1 for injection values above about  $\tilde{q}_{inj} = 0.13$ ). This is understandable in terms of the dual threshold condition. The threshold inversion is defined as that needed to satisfy the threshold condition with cavity photon number  $\tilde{q}_{sat}$  just sufficient to saturate the two-photon gain. Any injected photons then serve to increase the cavity photon number above saturation, and correspondingly decrease the necessary inversion. Figure 7.10 illustrates the injection threshold for a good cavity ( $\tilde{\gamma} = 2$ ) as a function of both pump rate and injected photon number.

For zero or low injection, over a range of pump rates around the pump threshold there are three real solutions for the photon number corresponding to the  $\tilde{q}_{inj}=0$  solutions  $\tilde{q}_{ss}^o$ ,  $\tilde{q}_{ss}^+$ , and  $\tilde{q}_{ss}^-$ . Each of these solutions must be individually tested for stability. Yet to determine the stability threshold, and hence a true injection threshold, there are actually three parameters of interest:  $\Delta \tilde{N}_o$ ,  $\tilde{q}_{inj}$ , and  $\tilde{\gamma}^5$ . The system must be examined over a range of cavity

<sup>&</sup>lt;sup>5</sup>Recall that when we found the steady-state solutions in Sec.7.3.3, the goodness of the laser cavity defined by  $\tilde{\gamma}$  played no role in the solutions. It only becomes important as we explore the stability of these solutions.

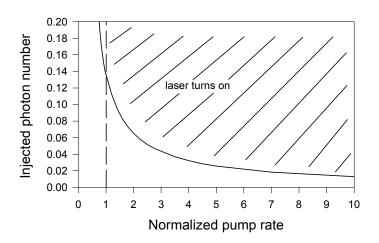


Figure 7.10: Variation of the injection threshold with pump rate

parameters from the good cavity limit to the bad cavity limit. Within this range, for any given (fixed) pump rate we find: (i) whether a stable solution ever exists; and (ii) if so, does it destabilize above or below a certain injection value. As before, real negative eigenvalues of Eq. 7.33 define stable solutions. All stability calculations are performed numerically.

The mid-photon number solution is again found to be unstable for all pump parameters, injected fields, and cavity values, and will thus never represent a physical output state of the laser. The high-photon number solution, however, is easily shown to be stable over the full range of injection parameters in the good cavity limit. In the bad-cavity limit, however, the stability of the solution is more complex, displaying regions of instability which vary with  $\tilde{\gamma}$  and  $\tilde{q}_{inj}$ . The limiting case  $\tilde{q}_{inj} \to 0$  reproduces the instability region shown in Fig. 7.7. An interesting result is that when  $\tilde{\gamma}$  is less than the critical value for stability

with no injected photons (Fig. 7.7), the laser will also be unstable with injected photons. In the region where the solutions are unstable, the laser will not turn on for any values of the pump rate  $\Delta \tilde{N}_o$  or injected photon number  $\tilde{q}_{inj}$  – it remains below threshold.

So far, the laser stability behavior looks remarkably similar to the case without injection and as such is rather uninteresting. New stability behavior becomes evident only upon closer examination of the low-photon number solution. For small pump rates this is the only solution and it displays unconditional stability. For higher pump rates two other solutions appear. Rather than maintaining permanent stability, the low-power solution then increases as  $\tilde{q}_{inj}$  increases and is only stable until it reaches a critical value,  $\tilde{q}_{inj}^{th}$ . At this point, the low- and mid-photon number solutions, which had been distinct real solutions, merge and become a complex conjugate pair. This obviously represents a loss of stability (or continued instability) for the solutions. As  $\tilde{q}_{inj}$  increases beyond this point, the laser is forced to switch from the low-power solution (now unstable) to the high-power solution (stable), and the laser turns on. The point  $\tilde{q}_{inj}^{th}$  thus defines the minimum injected photon number necessary to initiate lasing.

This threshold behavior is illustrated in Fig. 7.11, where three solutions for the steady-state photon number are plotted for  $\tilde{q}_{inj} \neq 0$  and a constant pump rate of  $\Delta \tilde{N}_o = 1.2$ . The results are described for the important case when the laser is initially 'off' and  $\tilde{q}_{inj}$  is increased slowly. The low power solution (dashed curve) increases as  $\tilde{q}_{inj}$  increases and is stable until it reaches the critical value  $\tilde{q}_{inj}^{th} \simeq 0.11$ . This is the *same* critical value determined from Fig. 7.10. As  $\tilde{q}_{inj}$  increases beyond this point, the state of the laser abruptly

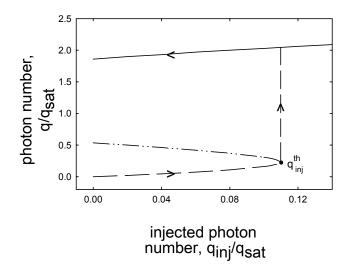


Figure 7.11: Injection threshold for a constant pump rate

switches from low power to high-power, and the laser turns on. Threshold is thus defined as the point where the lowest solution ends, and the arrows indicate the progression of the laser from off to on. The dashed, solid, and dotted-dashed curves are the solutions with  $\tilde{q}_{inj} \neq 0$  corresponding to the  $\tilde{q}_{inj} = 0$  solutions  $\tilde{q}_{ss}^0$ ,  $\tilde{q}_{ss}^+$ , and  $\tilde{q}_{ss}^-$  respectively. The discontinuous threshold behavior again indicates a first-order phase transition. The behavior of the laser as  $\tilde{q}_{inj}$  decreases depends on the quality of the cavity. For a good cavity, the laser will continue to operate at high power as  $\tilde{q}_{inj}$  decreases. For a bad cavity, the laser will only continue to operate at high power if the solution remains stable with  $\tilde{q}_{inj} = 0$ .

In addition, we studied the stability behavior of the laser for various values of the pump rate, and hence various injection thresholds  $\tilde{q}_{inj}^{th}$ . The injection

threshold decreases for higher values of the pump rate, as seen in Fig. 7.8 or Fig. 7.9. Although it only reaches zero for an infinitely high pump rate, beyond a certain point spontaneous emission will take the system above threshold and the laser will turn on. This pump rate is, however, well beyond the range of values at which most lasers operate. Future experimental work will test the theoretical injection threshold values against the actual laser threshold.

#### 7.5.1 Transient behavior of the laser

Although exploring the steady-state behavior and stability of the two-photon laser proves extremely useful, it does not give any predictions concerning how the state of the laser evolves from one solution to the next. Additional insights are gained by examining dynamic phenomena in the laser, including the buildup of coherent radiation caused by a pulsed excitation or small change in excitation.

The transient behavior and response of the laser is explored by numerically integrating Eqs. 7.25 and 7.24. We no longer assume a cw beam of a given amplitude is injected into the laser; instead a square-like trigger pulse with peak photon number  $q_{inj}^o$  is injected into the laser. The leading edge of the pulse is modelled as a rising exponential, and the trailing edge as a falling exponential. The rise- and fall-times are adjustable, as is the pulse amplitude and the duration of the pulse itself.

For all of the trials, the laser must be able to adiabatically follow the temporal variation of the pulse. This is true when the pulses turn on slowly and remain on for at least a few characteristic lifetimes, where the relevant time scale is the cavity lifetime. When the laser can adiabatically follow the tempo-

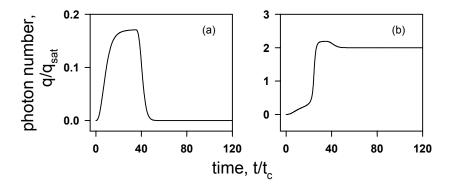


Figure 7.12: Transient evolution of the photon number for pumping 20% above threshold in the good cavity limit

ral variation of the pulse, the injection threshold is equal to that found in the cw case,  $q_{inj}^o = q_{inj}^{th}$ . Pulses with rapid risetimes and short durations change faster than the response time of the laser, and the injection threshold increases accordingly  $(q_{inj}^o \geq q_{inj}^{th})$ . The observed injection threshold for rapid pulses increased by as much as 10% over the minimum threshold.

The response of the laser for a good cavity is fairly straightforward, and an example involving some typical parameter values can clarify the description of the laser behavior. Figure 7.12 shows how the laser responds to injected trigger pulses for a good cavity  $(\gamma/\gamma_c = 2)$  when the pump rate is greater than the threshold pump rate  $(\Delta N_o = 1.2 \ \Delta N_o^{th})$  and when there are no photons in the cavity initially. For a weak trigger pulse (peak amplitude  $q_{inj}^o = 0.1 \ q_{sat}$ , Fig. 7.12a) the laser is not driven above threshold. The output pulse is basically unchanged from the trigger pulse, which remains true until the

pulse amplitude is very close to (or above) threshold. For a slightly stronger pulse (peak amplitude  $q_{inj}^o = 0.12 \ q_{sat}$ , Fig. 7.12b) the laser is driven above threshold and attains a constant amplitude after the injected pulse switches off. This is in good agreement with the injection threshold  $q_{inj}^{th} \simeq 0.11 \ q_{sat}$  calculated previously (see, for example, Fig. 7.11).

Quite different behavior is observed for the case of a bad cavity. We have identified three separate characteristic behaviors which correspond well with the bad-cavity stability regions discussed earlier. As an illustrative example, recall how the stability of the  $(q_{ss}^+, \Delta N_{ss}^+)$  solution changes with pump rate for the case of a bad cavity,  $(\gamma/\gamma_c = 0.2)$ . For pump rates just above threshold  $(1 < \Delta N_o/\Delta N_o^{th} \lesssim 1.26)$ , the high power solution is unstable and hence an injected pulse, no matter how strong, cannot turn on the laser. For higher pump rates,  $1.26 \lesssim \Delta N_o/\Delta N_o^{th} \lesssim 2.3$ , the solution becomes stable and the transient behavior of the laser displays large spiking in the initial turn-on and damped relaxation oscillations as it approaches steady-state. The predicted relaxation oscillations and transient spiking are entirely new behaviors and are shown in Fig. 7.13. For even larger pump rates  $(\Delta N_o/\Delta N_o^{th} \gtrsim 2.3)$  the system settles to a stable steady-state in a single oscillation.

The good cavity transient behavior shown in the plots is reminiscent of the experimental data on the dressed-state two-photon laser [18] with the exception that the rate-equation model does not predict the spiking during the initial turn-on of the laser nor the oscillatory behavior of the laser. It is known that models incorporating coherent effects lead to stable oscillating solutions [105], although it is not clear whether these effects alone properly account for the observed behavior. The initial spiking and damped oscillations seen in the

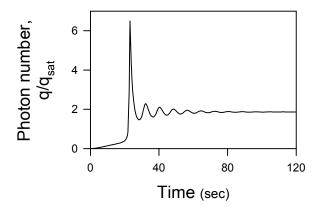


Figure 7.13: Transient evolution of the photon number in the bad-cavity limit bad cavity case more closely mimic the behavior observed in the dressed-state two-photon laser experiments. However, it would be incorrect to conclude that our model contains all of the correct physics for predicting this behavior, because the experiment was conducted using a very good cavity. The experimentally observed spiking behavior during turn-on remains an open question because no previous work has specifically investigated pulsed injection of a continuous-wave two-photon laser. However, we suspect that the behavior can be attributed to AC Stark shifts and coherent effects.

As a final note, we should mention some transient solutions which baffled us for quite some time. For various cavity values  $\gamma$ , the laser displayed periodic oscillations after the initial pulse switches off. Although the theory allowed damped oscillations, it did not predict stable oscillations. It was only in mapping out the region in  $\gamma$  and  $\Delta N_o$  where these oscillations occurred that the error became clear. We had randomly chosen a 'typical' pump value  $\Delta N_o = 1.25 \ \Delta N_o^{th}$  for performing many of the numerical integrations. Unfortunately, this value turned out to be far from typical, because it exactly corresponded to an eigenvalue with a zero real part. This led to stable oscillatory solutions which are mathematically existent, but would be quite difficult to realize in practice.

#### 7.5.2 Limitations of our model

Although the simplicity of rate-equations is one of their largest assets, it is also one of their greatest weaknesses: because the equations are reduced to bare fundamentals, they provide an incomplete model of laser systems. Generally, rate-equation results apply only when the laser is operating in a single cavity mode, and they are often unable to describe the instabilities seen in real lasers. In focusing only on the population and photon number, rate-equations also ignore any coherence in the coupling between radiation and matter. Coherent laser equations realize that light-matter interactions involve the coupling between optical waves and atomic dipoles, and determine the evolution of the radiated field through a polarization according to Maxwell's equations. A specific limitation of our model is that it only considers the degenerate case, in which both emitted photons have equal frequency. A more general model would start with the non-degenerate case (though it does turn out that the degenerate case is a limiting case of the non-degenerate one). We also used a two-level model (as in the effective Hamiltonian model), rather than a three-level model which includes the effect of the intermediate state on the two-photon transition. The two-level model does not consider the influences of detunings or Stark shifts on

laser stability or dynamic behavior. A more carefully accounting for the true level structure in the gain medium or accounting for spatial variation of the inversion and electromagnetic energy density are other ways we could increase the accuracy of the rate-equation model.

Alternately, more complete treatments, such as the semiclassical and fully quantum theories mentioned in the previous chapter, can be used to model the system. Such treatments may include interactions ignored in the rate-equation model. In general, semiclassical and quantum models are somewhat more complicated than rate-equation models, but they include a more rigorous physical description of the interaction between the fields and atoms. In the appropriate limits, average results of a quantum treatment coincide with the semiclassical treatment. Similarly, the semiclassical equations reduce to the rate-equations in the case when the coherence dephasing times are much faster than all other time constants in the system. We performed a density matrix treatment of our experimental system in Chapter 5.

As mentioned at the beginning of this chapter, we chose to make our model very simple, and ignore most of the effects just mentioned in order to get the most intuitive, least mathematical solution. Despite this, it should prove a reasonable qualitative description of the types of behavior one might expect to see in a two-photon laser.

## Chapter 8

## Conclusions and Future Directions

This thesis has demonstrated the usefulness of Raman scattering for generating two-photon gain. I perform pump-probe spectroscopy in a laser-driven potassium vapor and study the scattering processes expected to take place, especially one-photon and two-photon Raman scattering. High gain relies on the nonlinear interactions and coupling between the pump and probe laser fields and the atomic gain medium. Under certain conditions, I observe  $\sim 30\%$  two-photon gain in a potassium vapor cell.

Iperform a semiclassical analysis of driven three-level atoms which is used to model the nonlinear interactions occurring in the potassium cell. I adapt generalized density-matrix equations of motion to describe the experimental system and use them to explicitly find the level populations and coherences. From these I also determine the atomic absorptive response, and compare the theoretical response to the experimentally measured spectrum. The results are in good qualitative agreement. Future work will refine the theory to carefully account for all of the hyperfine levels of potassium and propagation effects in the cell.

Although the experimental work to date focuses on the observation of continuous-wave two-photon optical amplification, this should naturally lead into a robust experimental realization of a two-photon laser. In order to help understand the properties of such a laser, I present a simple rate-equation theory of two-photon lasers in which I explore the equations describing the cavity photon number and population inversion density as a function of time in a pumped two-level system. I solve for the steady-states and determine the stabilities of the calculated solutions. From the analysis, I expect the two-photon laser to display novel threshold characteristics, including optical bistability. These results are consistent with the behavior predicted from more complicated models.

Current laboratory efforts are directed toward suppressing the minor competing effects that occur simultaneously in the experimental system with the desired Raman gain: self-defocusing and the background caused by the Rabi gain. Both of these processes depend on the population in the  $4P_{1/2}$  excited state, so quenching this population serves to reduce the efficiency of these competing processes relative to the Raman scattering. Reducing the excited state population can be done by collisionally dephasing the  $4S_{1/2} \rightarrow 4P_{1/2}$  transition using a buffer gas introduced into the potassium cell. Because the dephasing rate of the electronic transition is large in comparison to the dephasing rate of the coherence between the ground levels, collisions serve to quickly depopulate the excited state. Preliminary results with both nitrogen and helium buffer gases are quite promising. Both the self-focusing and Rabi gain can be virtually eliminated with only a small effect on the Raman gain. Further studies are needed to determine optimal buffer gas pressures and the best choice of gas

itself.

Use of a buffer gas is intended to optimize the Raman gain process through reduction of competing effects. Yet the ability of a buffer gas to quickly depopulate the  $4P_{1/2}$  excited state also has potential for realizing two-photon gains even higher than the 30% observed to date. The maximum gain is partially limited by the amount of light that can be effectively scattered, which eventually boils down to how fast the atoms can be optically pumped into the F=1 ground state and hence used in a scattering process for producing gain. In a gain medium of pure potassium, the spontaneous decay rate of the excited state limits the optical pumping rate. With a buffer gas introduced into the potassium, the effective excited-state decay rate becomes faster due to collisionally induced excitation, and hence the optical pumping rate increases. This positive buffer-gas side effect is still under investigation.

In the past, observed two-photon gain was so small as to prevent experimental studies of single pass two-photon amplification. The high-gain system described in this thesis should, however, make studies of this type feasible. The apparatus is also well suited for investigating how the photon noise of a beam of light is modified by the two-photon amplification process. Work is in progress to study the noise properties of saturated versus unsaturated one-photon and two-photon Raman amplification and try to understand how the nonlinear gain processes affect the noise properties and photon statistics of the amplified light. Few experimental studies on nonlinear optical amplifiers have been performed, and studies such as these should significantly contribute to the pool of knowledge on this subject.

Reducing competing effects and studies of nonlinear optical amplification

are two more steps toward a robust experimental realization a two-photon laser. Continuing work is being done on the development of a two-photon laser based on the two-photon Raman scattering process. Such a laser is expected to have high gain, and a correspondingly high output power. This should facilitate studies of the laser's threshold behavior, noise properties, photon statistics, and other quantities which are still very much unknown.

# **Bibliography**

- [1] A. M. Prokhorov. Quantum Electronics. Science, 10:828-830, 1965.
- [2] P. P. Sorokin and N. Braslau. Some Theoretical Aspects of a Proposed Double Quantum Stimulated Emission Device. IBM J. Res. Dev., 8:177-181, 1964.
- [3] R. Loudon. The Quantum Theory of Light. Oxford Science Publications, New York, 1992, Ch. 7.
- [4] P. Lambropoulos. Quantum Statistics of a Two-Photon Quantum Amplifier. *Phys. Rev.*, 156:286-297, 1967.
- [5] See, for example, the review article by D. F. Walls. Squeezed states of light. *Nature*, 306:141-146, 1983.
- [6] M. Schubert and G. Wiederhold. On the Two-Photon Lasing Process in a Degenerate System. Exp. Tech. Phy., 27:225-234, 1979.
- [7] M. Reid, K. J. McNeil, and D. F. Walls. Unified approach to multiphoton lasers and multiphoton bistability. *Phys. Rev. A*, 24:2029-2043, 1981.
- [8] Z. C. Wang and H. Haken. Theory of Two-photon Lasers III: Two-Photon Laser with Injected Signal. Z. Phys. B, 56:83-90, 1984.

- [9] A. W. Boone and S. Swain. Theory of the degenerate two-photon laser. Phys. Rev. A, 41:343-351, 1990.
- [10] R. W. Boyd. Nonlinear Optics. Academic Press, Inc., New York, 1992, p. 266.
- [11] A non-specialists primer to many of the following processes can be found in Ref. [10]. For further references, see the good review article by N. Bloembergen. Nonlinear optics and spectroscopy. Rev. Mod. Phys., 54(3):685-695, 1982.
- [12] A general treatment of the parametric amplification principle has been given by W. H. Louisell. Coupled Mode and Parametric Electronics. John Wiley & Sons, Inc., New York, 1960.
- [13] See, for example, V. S. Butylkin, A. E. Kaplan, Yu. G. Khronopulo, and E. I. Yakubovich. Resonant Nonlinear Interactions of Light with Matter. Springer-Verlag, Berlin, 1989, p. 152-205.
- [14] See, for example, Y. R. Shen. The Principles of Nonlinear Optics. Wiley, New York, 1984, p. 303-333.
- [15] For a review of work on multi-photon ionization see, for example, G. Mainfray and C. Manus. *Multiphoton Ionization of Atoms*. Edited by S. Chin and P. Lambropoulos. Academic Press, New York, 1984, p. 7.
- [16] R. H. Dicke. Coherence in Spontaneous Radiation Processes. Phys. Rev., 93:99-110, 1954.

- [17] Y. Zhu, Q. Wu, S. Morin, and T. W. Mossberg. Observation of a Two-Photon Gain Feature in the Strong-Probe Absorption Spectrum of Driven Two-Level Atoms. *Phys. Rev. Lett.*, 65:1200-1203, 1990.
- [18] D. J. Gauthier, Q. Wu, S. E. Morin, and T. W. Mossberg. Realization of a Continuous-Wave, Two-Photon Optical Laser. *Phys. Rev. Lett.*, 68:464-467, 1992.
- [19] The stimulated Raman effect was first observed shortly after the demonstration of the first ruby laser by E. J. Woodbury and W. K. Ng. Proc. IRE, 50:2347, 1962.
- [20] See, for example, Ref. [47]. Additionally, most of my understanding of the subject is derived from John Thomas's written class notes for Physics 317.
- [21] L. Allen and C. R. Stroud Jr. Broadening and Saturation in n-Photon Absorption. Phys. Rep., 91:1-29, 1982.
- [22] This description mimics that presented in Chapter 1 of M. Born and E. Wolf. Principles of Optics. Fifth Edition, Pergamon, New York, 1975.
- [23] M. T. Gruneisen, Two-Beam Coupling and Phase Conjugation by Resonant Nonlinear Optical Interaction, Ph.D. Thesis, Institute of Optics, University of Rochester, 1989, unpublished.
- [24] M. Brune, J. M. Raimond, and S. Haroche. Theory of the Rydbergatom two-photon micromaser. *Phys. Rev. A*, 35:154-163, 1987; and L. Davidovich, J. M. Raimond, M. Brune, and S. Haroche. Quantum theory

- of a two-photon micromaser. *Phys. Rev. A*, 36:3771-3787, 1987; M. Brune, J. M. Raimond, P. Goy, L. Davidovich, and S. Haroche. The Two-Photon Rydberg Atom Micromaser. *IEEE J. Quantum Electron.*, 24:1323-1330, 1988.
- [25] M. Brune, J. M. Raimond, P. Goy, L. Davidovich, and S. Haroche. Realization of a Two-Photon Maser Oscillator. *Phys. Rev. Lett.*, 59:1899-1902, 1987.
- [26] Michelle S. Malcuit. Competition Effects in Nonlinear Optics. Ph.D. Thesis, The Institute of Optics, University of Rochester, 1987, unpublished.
- [27] See Ref. [10], p. 346.
- [28] A good review article is that by C. E. Wieman and L. Hollberg. Using diode lasers for atomic physics. Rev. Sci. Instrum., 62:1-20, 1991.
- [29] I gratefully acknowledge the careful and detailed description of how to set up a diode laser system with grating feedback given in K. B. MacAdam, A. Steinbach and C. Wieman. A narrow band tunable diode laser system with grating feedback, and a saturated absorption spectrometer for Cs and Rb. American Journal of Physics, 60(12):1098-1111, 1992.
- [30] Jeff Bischoff. Senior Honors Project, Duke University, 1995, unpublished.
- [31] See, for example, P. McNicholl and H. J. Metcalf. Sychronous cavity mode and feedback wavelength scanning in dye laser oscillators with gratings. Appl. Opt., 24:2757-2761, 1985.

- [32] Hui-Rong, S. V. Benson, and T. W. Hänsch. A 'toy-train' wavemeter.

  \*Laser Focus\*, March 1981, p. 54-58.
- [33] M. W. Hamilton. An introduction to stabilized lasers. *Contemp. Phys.*, 30(1):21-33, 1989.
- [34] P. Kumar and J. H. Shapiro. Observation of Raman-shifted oscillation near the sodium D lines. Opt. Lett., 10:226-228, 1985.
- [35] Philip R. Hemmer. Precision studies of stimulated resonance Raman scattering in atomic beams. PhD. Thesis, Massachusetts Institute of Technology, 1984, unpublished.
- [36] Hugh Robinson, private communication.
- [37] This figure is taken from Fig. 4.2 in Ref. [23].
- [38] M. Poelker, P. Kumar, and S.-T. Ho. Laser frequency translation: a new method. Opt. Lett., 16:1853-1855, 1991.
- [39] P. Verkerk, B. Lounis, C. Salomon, C. Cohen-Tannoudji, J.-Y. Courtois, and G. Grynberg. Dynamics and Spatial Order of Cold Cesium Atoms in a Periodic Optical Potential. *Phys. Rev. Lett.*, 68:3861-3864, 1992.
- [40] S. Haroche and R. Hartmann. Theory of Saturated-Absorption Line Shapes. Phys. Rev. A, 6:1280-1300, 1972.
- [41] M. T. Gruneisen, K. R. MacDonald, and R. W. Boyd. Induced gain and modified absorption of a weak probe beam in a strongly driven sodium vapor. J. Opt. Soc. Am. B, 5:123-129, 1988.

- [42] B. Nikolaus, D. Z. Zhang, and P. E. Toschek. Two-Photon Laser. Phys. Rev. Lett., 47:171-173, 1981.
- [43] R. W. Boyd, M. G. Raymer, P. Narum, and D. J. Harter. Four-wave parametric interactions in a strongly driven two-level system. Phys. Rev. A, 24:411-423, 1981.
- [44] N. Bloembergen. Nonlinear Optics. Benjamin, New York, 1965.
- [45] See, for example, C. Cohen-Tannoudji and J. Dupont-Roc. Experimental Study of Zeeman Light Shifts in Weak Magnetic Fields. Phys. Rev. A, 5:968-984, 1972.
- [46] S. H. Autler and C. H. Townes. Stark effect in rapidly varying fields. Phys. Rev., 100:703-722, 1955.
- [47] See, for example, B. W. Shore. The Theory of Coherent Atomic Excitation. John Wiley & Sons, New York, 1990, and references therein.
- [48] G. S. Agarwal. Generation of odd subharmonic Raman resonances from Stokes-anti-Stokes coupling. Phys. Rev. A, 43:1523-1527, 1991.
- [49] R. P. Lucht, R. Trebino, and L. A. Rahn. Resonant multiwave-mixing spectra of gas-phase sodium: Nonperturbative calculations. *Phys. Rev.* A, 45:8209-8227, 1992.
- [50] R. Trebino and L. A. Rahn. Calculation of higher-order wave-mixing spectra. Opt. Lett., 15:354-356, 1990; and Ref. [133].
- [51] See Daniel J. Gauthier. Instabilities and Chaos of Laser Beams Propagating Through Nonlinear Optical Media. Ph.D. Thesis, The Institute of

- Optics, University of Rochester, 1989, p. 115, unpublished.
- [52] See, for example, C. Cohen-Tannoudji, L. Dupont-Roc, and G. Grynberg.

  Atom-Photon Interactions. John Wiley & Sons, Inc., New York, 1992.
- [53] The computer code, Sparse 1.3: A Sparse Linear Equation Solver, was written by K. S. Kundert and Alberto Sangiovanni-Vincentelli, University of California, Berkeley, 1988.
- [54] W. H. Press, S. A. Teukolsky, W. T. Vetterling, and B. P. Flannery. Numerical Recipes in C. Cambridge University Press, New York, 1992. I modified the routine odeint for my purposes.
- [55] A. Corney. Atomic and Laser Spectroscopy. Clarendon Press, Oxford, 1977, chapter IX.
- [56] K. J. McNeil and D. F. Walls. Quantum theory of multiphoton lasers I: Systems in detailed balance. J. Phys. A, 8:104-110, 1975; and Quantum theory of multiphoton lasers II: Systems without detailed balance. J. Phys. A, 8:111-119, 1975.
- [57] P. Lambropoulos. On the theory of a two-photon quantum amplifier. Phys. Lett., 21:418-419, 1966.
- [58] R. L. Carman. Amplifiers involving two-photon energy-extraction schemes. Phys. Rev. A, 12:1048-1061, 1974.
- [59] E. B. Gordon and Y. L. Moskvin. Two-photon laser amplifiers. Sov. Phys. JETP, 43:901-907, 1977.

- [60] L. M. Narducci, W. W. Eidson, P. Furcinitti, and D. C. Eteson. Theory of a two-photon laser amplifier. Phys. Rev. A, 16:1665-1672, 1977.
- [61] T. Hoshimiya, A. Yamagishi, N. Tanno, and H. Inaba. A Semiclassical Theory of Two-Photon Laser Oscillation. *Japan. J. Appl. Phys.*, 17:2177-2178, 1978.
- [62] A. R. Bulsara and W. C. Schieve. Semiclassical stochastic description of the two-photon laser. Phys. Rev. A, 19:2046-2051, 1979.
- [63] P. García Fernández and L. Sainz de los Terreros. Calculation of the offdiagonal elements of a two-photon laser. Opt. Comm., 61:151-154, 1987.
- [64] S. Songen. Discussion on two-photon laser oscillation process. Chin. J. Lasers, 14:1-5, 1987.
- [65] H. M. Concannon and D. J. Gauthier. Simple rate-equation model for two-photon lasers. Opt. Lett., 19:472-474, 1994.
- [66] Z. C. Wang and H. Haken. Theory of Two-photon Lasers I: Semiclassical Theory. Z. Phys. B, 55:361-370, 1984.
- [67] Z. C. Wang and H. Haken. Theory of Two-photon Lasers II: Fokker-Planck Equation Treatment. Z. Phys. B, 56:77-82, 1984.
- [68] M. O. Scully and W. E. Lamb, Jr. Quantum Theory of an Optical MaserI: General Theory. Phys. Rev., 159:208-226, 1967.
- [69] R. Görtz and D. F. Walls. Steady State Solutions of Master Equations without Detailed Balance. Z. Physik B, 25:423-427, 1976.

- [70] N. Nayak and B. K. Mohanty. Quantum theory of an inhomogeneously broadened two-photon laser. Phys. Rev. A, 19:1204-1210, 1979.
- [71] L. Sczaniecki. Quantum theory of subharmonic lasers. Non-equilibrium phase transition of the first order. *Opt. Acta*, 27:251-261, 1980.
- [72] L. Sczaniecki. Quantum theory of multi-photon lasers. Opt. Acta, 29:69-85, 1982.
- [73] S. Y. Zhu and M. O. Scully. Theoretical study of a two-photon double-beam laser. *Phys. Rev. A*, 38:5433-5436, 1988.
- [74] D. A. Holm and M. Sargent III. Quantum theory of multiwave mixing: Two-photon two-level model. Phys. Rev. A, 33:1073-1090, 1986.
- [75] A. W. Boone and S. Swain. Effective Hamiltonians in two-photon laser theory. Opt. Comm., 73:47-50, 1989; and A. W. Boone and S. Swain. Effective Hamiltonians and the two-photon laser. Quantum Opt., 1:27-47, 1989.
- [76] W. Z. Cheng and H. Haken. Quantum theory of the two-photon laser. Z. Phys. B, 71:253-259, 1988.
- [77] S. Zhu and X. Li. Quantum theory of a two-photon laser. Phys. Rev. A, 36:3889-3896, 1987.
- [78] S. Swain. Field fluctuations and cross-correlation in the two-photon laser.
  J. Mod. Opt., 35:103-111, 1988.
- [79] I. Ashraf and M. S. Zubairy. Natural linewidth of a two-level two-photon laser. Opt. Comm., 71:92-96, 1989.

- [80] G. Yang, Z. Huang and G. Hu. Quantum Theory of a Nondegenerate Two-Photon Laser. Commun. Theor. Phys., 14:397-410, 1990.
- [81] N. Lu. Q-function approach to a two-photon laser. Phys. Rev. A, 42:6756-6766, 1990.
- [82] M. C. Teich and B. E. A. Saleh. Squeezed and Antibunched Light. Physics Today, 43(6):26-34, 1990.
- [83] H. P. Yuen. Two-photon stimulated emission and pulse amplification. Appl. Phys. Lett. 26:505-507, 1975.
- [84] O. Hirota. Generalized Quantum Measurement Theory and Its Application in Quantum Communication Theory: Optical Communication by Two-Photon Laser. *Elec. and Comm. in Japan*, 60-A:10-18, 1977; and O. Hirota, I. Shioya, S. Ikehara, and Y. Suematsu. Optimal Control of Quantum Noise: Optical Communications by Two-photon Laser Part II. *Trans. of IECE of Japan*, E61:273-279, 1978.
- [85] D. J. Rowe. The two-photon laser beam as a breathing mode of the electromagnetic field. Can. J. Phys., 56:442-446, 1978.
- [86] H. P. Yuen. Two-photon coherent states of the radiation field. Phys. Rev. A, 13:2226-2243, 1976.
- [87] Yu. M. Golubev. Statistics of the electromagnetic field radiated in a two-photon process. *Opt. Spectrosc.*, 46:1-3, 1979.
- [88] L. A. Lugiato and G. Strini. On nonclassical effects in two-photon optical bistability and two-photon laser. Opt. Comm., 41:374-378, 1982.

- [89] M. D. Reid and D. F. Walls. Quantum fluctuations in the two-photon laser. Phys. Rev. A, 28:332-343, 1983.
- [90] M. O. Scully, K. Wodkiewicz, M. S. Zubairy, J. Bergou, N. Lu, and J. Meyer ter Vehn. Two-Photon Correlated-Spontaneous-Emission Laser: Quantum Noise Quenching and Squeezing. *Phys. Rev. Lett.*, 60:1832-1835, 1988.
- [91] N. Lu, F. Zhao, and J. Bergou. Nonlinear theory of a two-photon correlated-spontaneous-emission laser: A coherently pumped two-level two-photon laser. *Phys. Rev. A*, 39:5189-5208, 1989.
- [92] M. Majeed and M. S. Zubairy. Effect of phase fluctuations on noise-free amplification and phase squeezing in a two-photon laser. *Phys. Rev. A*, 44:4688-4692, 1991.
- [93] M. Majeed and M. S. Zubairy. Role of pump phase fluctuations in a two-photon phase-sensitive amplifier. *Phys. Rev. A*, 52:2350-2360, 1995.
- [94] G. Hu and C. Sha. Dispersive squeezing in the two-photon bistable system and two-photon laser with an injected signal. *Phys. Lett. A*, 159:47-54, 1991.
- [95] C. M. Savage and D. F. Walls. Squeezing via two-photon transitions. Phys. Rev. A, 33:3282-3291, 1986.
- [96] K. J. McNeil and D. F. Walls. Possibility of observing enhanced photon bunching from two-photon emission. *Phys. Lett.*, 51A:233-234,1975.

- [97] M. S. Zubairy. Photon statistics of a two-photon laser. *Phys. Lett.*, 80A:225-228,1980.
- [98] A. Bandilla and H. Voigt. Quantum statistics of light after saturated two-photon emission processes and the photon statistics of a two-photon laser. Opt. Comm., 43:277-280, 1982.
- [99] M. S. Zubairy. Nonclassical effects in a two-photon laser. Phys. Lett., 87A:162-164, 1982.
- [100] M. P. Sharma and L. M. Brescansin. Effect of cooperative atomic interactions on photon statistics in a two-photon laser. *Phys. Rev. A*, 3:1893-1897, 1981.
- [101] N. Lu. Photon statistics in a single-mode two-photon laser: Exact versus effective interaction Hamiltonian. *Opt. Comm.*, 77:203-209, 1990.
- [102] S. Bay and P. Lambropoulos. A Fokker Planck approach to the twophoton laser: Suppressing fluctuations by means of the dynamic Stark shift. Opt. Comm., 112:302-307, 1994.
- [103] N. B. Abraham, L. A. Lugiato, L. M. Narducci. Overview of instabilities in laser systems. J. Opt. Soc. Am. B, 2:7-14, 1985.
- [104] H. Ito and T. Nakagomi. Thermodynamic Limit in Quantum Stochastic Process. Prog. Theor. Phys., 57:54-66, 1977.
- [105] C. Z. Ning and H. Haken. Instability in degenerate two-photon running wave laser. Z. Phys. B., 77:157-162, 1989; and C. Z. Ning. Application

- of the Slaving principle and the Normal form theory to the two-photon laser. Ph.D. Thesis, University of Stuttgart, 1991, unpublished.
- [106] C. Z. Ning. Instability in degenerate two–photon running wave laser with detuning. Z. Phys. B., 71:247-252, 1988.
- [107] C. Z. Ning and H. Haken. Generalized Ginzburg-Landau equation for self-pulsing instability in a two-photon laser. Z. Phys. B., 77:163-174, 1989.
- [108] C. Z. Ning and H. Haken. Geometrical Phase and Amplitude Accumulations in Dissipative Systems with Cyclic Attractors. *Phys. Rev. Lett.*, 68:2109-2112, 1992; and C. Z. Ning and H. Haken. The geometric phase in nonlinear dissipative systems. *Mod. Phys. Lett. B.*, 6:1541-1568, 1992.
- [109] H. R. Heatley, C. N. Ironside, and W. J. Firth. Ultrashort-pulse generation using two-photon gain. Opt. Lett., 8:628-630, 1993.
- [110] Y. Wang and Y. Guan. Chaotic Phenomena in a Two-Photon Laser with Injected Signal. Commun. Theor. Phys., 17:393-400, 1992.
- [111] E. Roldán, G. J. de Valcárcel and R. Vilaseca. Operation conditions and stability of a degenerate two-photon laser. Opt. Comm., 104:85-90, 1993.
- [112] G. J. de Valcárcel, E. Roldán, J. F. Urchueguía, and R. Vilaseca. Twophoton laser dynamics. *Phys. Rev. A*, 52:4059-4069, 1995.
- [113] S. Ovadia and M. Sargent III. Two-photon laser and optical-bistability sidemode instabilities. Opt. Comm., 49:447-452, 1983.

- [114] S. Ovadia, M. Sargent III, and S. T. Hendow. Effects of dynamic Stark shifts on two-photon side-mode instabilities. *Opt. Lett.*, 10:505-507, 1985.
- [115] J. Zakrzewski, M. Lewenstein, and T. W. Mossberg. Theory of dressed-state lasers. I. Effective hamiltonians and stability properties. *Phys. Rev. A*, 44:7717-7731, 1991; II. Phase diffusion and squeezing. *Phys. Rev. A*, 44:7732-7745, 1991; and III. Pump-depletion effects. *Phys. Rev. A*, 44:7746-7758, 1991.
- [116] S. Yatsiv, M. Rakni, and S. Barak. Enhanced two-proton [sic] emission. Phys. Rev. Lett., 23:1282-1284, 1968.
- [117] P. Braunlich and P. Lambropoulos. Detection of singly stimulated twophoton emission from metastable deuterium atoms. *Phys. Rev. Lett.*, 25:135-138, 1970.
- [118] D. S. Bethune, J. R. Lankard, and P. P. Sorokin. Studies of the metastable  $c^3\Pi_u$  state of  $H_2$ : Towards a two-photon amplifier. *J. Chem. Phys.*, 69:2076-2081, 1978.
- [119] M. M. T. Loy. Two-Photon Adiabatic Inversion. Phys. Rev. Lett., 41:473-475, 1978.
- [120] J. Y. Gao, W. W. Eidson, M. Squicciarini, and L. M. Narducci. Scheme for investigation of two-photon emission in sodium. J. Opt. Soc. Am. B, 1:606-608, 1984.
- [121] H. Schlemmer, D. Frolich, and H. Welling. Two-photon amplification on cascade-transitions, Opt. Comm., 32:141-144, 1980.

- [122] D. J. Jackson and J. J. Wynne. What is the Signature of a Two-Photon Laser? *Appl. Phys. B*, 28:238, 1982.
- [123] C. Ironside. Two-Photon Gain Semiconductor Amplifier. IEEE J. Quant. Elec., 28:842-847, 1992.
- [124] G. Grynberg, E. Giacobino, and F. Biraben. Two-photon optically pumped laser. Opt. Comm., 36:403-405, 1981.
- [125] S. Haroche and J.-M. Raimond. Cavity Quantum Electrodynamics. Scientific American, 268(4):54-62, 1993
- [126] J. A. C. Gallas, G. Leuchs, H. Walther, and H. Figger. "Rydberg atoms: High-resolution spectroscopy and radiation interaction—Rydberg molecules" in *Advances in Atomic and Molecular Physics*. Edited by D. Bates and B. Bederson. Academic Press, Orlando, vol. 20, p. 413.
- [127] B. R. Mollow. Power Spectrum of Light Scattered by Two-Level Systems. Phys. Rev., 188:1969-1975, 1969.
- [128] F. Schuda, C. R. Stroud, Jr., and M. Hercher. Observation of the resonant Stark effect at optical frequencies. J. Phys. B, 7:L198-L202, 1974; W. Hartig, W. Rasmussen, R. Schieder, and H. Walter. Study of the Frequency Distribution of the Fluorescent Light Induced by Monochromatic Radiation, Z. Phys. A, 278:205-210, 1976; and R. E. Grove, R. Y. Wu, and S. Ezekiel. Measurement of the spectrum of resonance fluorescence from a two-level atom in an intense monochromatic field. Phys. Rev. A, 15:227-233, 1977.

- [129] C. Cohen-Tannoudji and S. Reynaud. Dressed-atom description of resonance fluorescence and absorption spectra of a multi-level atom in an intense laser beam. J. Phys. B., 10:345-363, 1977.
- [130] G. Grynberg, E. LeBihan, and M. Pinard. Two-wave mixing in sodium vapour. J. Phys. (Paris), 47:1321-1325, 1986; D. Grandclement, G. Grynberg, and M. Pinard. Observation of Continuous-Wave Self-Oscillation Due to Pressure-Induced Two-Wave Mixing in Sodium. Phys. Rev. Lett., 59:40-43, 1987; G. Khitrova, J. F. Valley, and H. M. Gibbs. Gain-Feedback Approach to Optical Instabilities in Sodium Vapor. Phys. Rev. Lett., 60:1126-1129, 1988; A. Lezama, Y. Zhu, M. Kanskar, and T. W. Mossberg. Radiative emission of driven two-level atoms into the modes of an enclosing optical cavity: The transition from fluorescence to lasing. Phys. Rev. A, 41:1576-1581, 1990.
- [131] M. Lewenstein, Y. Zhu, and T. W. Mossberg. Two-Photon Gain and Lasing in Strongly Driven Two-Level Atoms. Phys. Rev. Lett., 64:3131-3134, 1990.
- [132] J. Zakrzewski and M. Lewenstein. Theory of dressed-state lasers in the bad-cavity limit. Phys. Rev. A, 45:2057-2069, 1992.
- [133] See, for example, R. Trebino and L. A. Rahn. Subharmonic resonances in higher-order collision-enhanced wave mixing in a sodium-seeded flame. Opt. Lett., 12:912-914, 1987; and G. S. Agarwal. Subharmonic Raman effect in nonlinear mixing. Opt. Lett., 13:482-485, 1988.
- [134] A. Hemmerich, C. Zimmermann, and T. W. Hänsch. Multiphoton transi-

- tions in a Spin-Polarized 3D Optical Lattice. *Phys. Rev. Lett.*, 72:625-628, 1994.
- [135] P. Meystre and M. Sargent. Elements of Quantum Optics. Springer-Verlag, New York, 1991.
- [136] See, for example, O. Svelto. Principles of Lasers. Plenum Press, New York, 1989; and A. E. Siegman. Lasers. University Science Books, Mill Valley, California, 1986.
- [137] L. A. Lugiato, L. M. Narducci, J. R. Treadicce, and D. K. Bandy. "25 Years of Laser Instabilities" in *Instabilities and Chaos in Quantum Optics* II. Plenum Press, New York, 1988.
- [138] See page 16 of Ref. [10].
- [139] M. Schubert and B. Wilhelmi. Nonlinear Optics and Quantum Electronics. John Wiley & Sons, New York, 1986, p. 214.
- [140] Daniel Gauthier, private communication.
- [141] H. Risken. "Single- and Multimode Instabilities in Lasers" in Optical Instabilities. Cambridge University Press, England, 1986.

## **Biography**

Hope M. Concannon was born on the summer solstice, June 21, 1968 in Chicago, Illinois. Despite the mystical nature of her birthdate she led a fairly ordinary childhood, filling her freetime playing with friends, reading, ice-skating, practicing the piano, and the martial arts. After six years in the Chicago Public School System, she transferred to Morgan Park Academy where she eventually graduated first in her high-school class in 1986. Due to close ties with her three sisters and her parents, she attended nearby Valparaiso University as she continued her education. Being a true student of the liberal arts, she picked up majors in Physics and Mathematics and minors in Philosophy and the Humanities before graduating with highest honors in December 1990. In the fall of 1991 she was awarded an A. B. Duke Fellowship at Duke University, so she pulled up stakes and moved down to Durham, North Carolina to pursue graduate work in Physics. Under the tutelage of Dr. Daniel J. Gauthier, she received her Master's degree in December 1993. Along the way, she also became addicted to two new extracurricular activities that have made her infamous in the Physics Department for her bruises and injuries – whitewater kayaking and mountain biking. She has also been know to jump out of an airplane as a birthday present to herself. She now has her sights set on finishing up her graduate studies in order to enter the "real world" and pursue her dream of teaching physics and instilling the love of science in others.

#### LIST OF PUBLICATIONS

'Observation of large continuous-wave two-photon optical amplification,' H. M. Concannon, W. J. Brown, J. R. Gardner, and D. J. Gauthier, *Phys. Rev. Lett.*, in preparation.

'Recent Advances in Two-Photon Lasers,' H. M. Concannon and D. J. Gauthier. Condensed Matter News 3:7-13, 1994.

'The two-photon laser', in *Nonlinear Spectroscopy of Solids: Advances and Applications*. Edited by B. Di Bartolo and B. Bowlby. Plenum Press, New York, 1994.

'Simple rate-equation model for two-photon lasers,' H. M. Concannon and D.

J. Gauthier, Opt. Lett., 19:472-474, 1994.

'Stabilizing unstable periodic orbits in a fast diode resonator using continuous time-delay autosynchronization,' D. J. Gauthier, D. W. Sukow, H. M. Concannon, and J. E. S. Socolar. *Phys. Rev. E*, 50:2343-2346, 1994.

'Instabilities in two-photon lasers,' in  $Chaos\ in\ Optics.$  R. Roy, ed., Proc. SPIE 2039:198-205, 1993.